UNIVERSIDADE FEDERAL DE SÃO CARLOS

CENTRO DE CIÊNCIAS EXATAS E DE TECNOLOGIA

PROGRAMA DE PÓS-GRADUAÇÃO EM FÍSICA

&

SORBONNE UNIVERSITÉ

ÉCOLE DOCTORALE DE PHYSIQUE ET CHIMIE DES MATÉRIAUX

Multiferroicity and Structural Anomalies in Quadruple Perovskite Manganites: Case Study $(\mathrm{A})\mathrm{Mn_7O_{12}}$, A=Na and La

Vinícius Pascotto Gastaldo

Orientador: Adilson Jesus Aparecido de Oliveira

Co-orientador: Andrea Gauzzi

São Carlos

2019

UNIVERSIDADE FEDERAL DE SÃO CARLOS

CENTRO DE CIÊNCIAS EXATAS E DE TECNOLOGIA

PROGRAMA DE PÓS-GRADUAÇÃO EM FÍSICA

&

SORBONNE UNIVERSITÉ

ÉCOLE DOCTORALE DE PHYSIQUE ET CHIMIE DES MATÉRIAUX

Multiferroicity and Structural Anomalies in Quadruple Perovskite Manganites: Case Study $(\mathrm{A})\mathrm{Mn_7O_{12}}$, A=Na and La

Tese apresentada em regime de cotutela entre a Universidade Federal de Sâo Carlos e Sorbonne Université ao Programa de Pós-graduação em Física da Universidade Federal de São Carlos e à École Doctorale de Physique et Chimie des Matériaux como parte dos requisitos para obtenção do título de Doutor em Ciências pela UFSCar e Docteur en Physique pela Sorbonne.

Vinícius Pascotto Gastaldo

Orientador: Adilson Jesus Aparecido de Oliveira

Co-orientador: Andrea Gauzzi

São Carlos

2019

Vinícius Pascotto Gastaldo Multiferroicity and Structural Anomalies in Quadruple Perovskite Manganites: Case Study $(\mathbf{A})\mathbf{Mn_7O_{12}}$, A=Na and La/ Vinícius Pascotto Gastaldo. – São Carlos, 2019- 103 p. : il. (algumas color.) ; 30 cm.
Orientador: Adilson Jesus Aparecido de Oliveira
Tese (Doutorado) – Universidade Federal de Sâo Carlos, 2019.
1. Quadruple Perovskites. 2. Magnetic Oxides. 3. Multiferroic Materials. 4. Manganites. I. Título

UNIVERSIDADE FEDERAL DE SÃO CARLOS

Centro de Ciências Exatas e de Tecnologia
Programa de Pós-Graduação em Física

Folha de Aprovação

Assinaturas dos membros da comissão examinadora que avaliou e aprovou a Defesa de Tese de Doutorado do candidato Vinicius Pascotto Gastaldo, realizada em 15/01/2019:

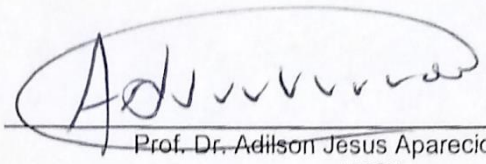

Prof. Dr. Adilson Jesus Aparecido de Oliveira
UFSCar

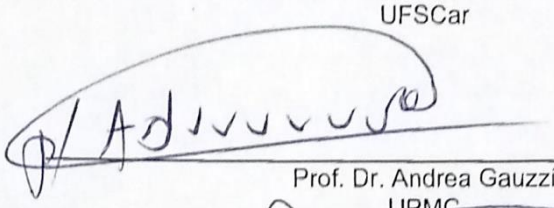

Prof. Dr. Andrea Gauzzi
UPMC

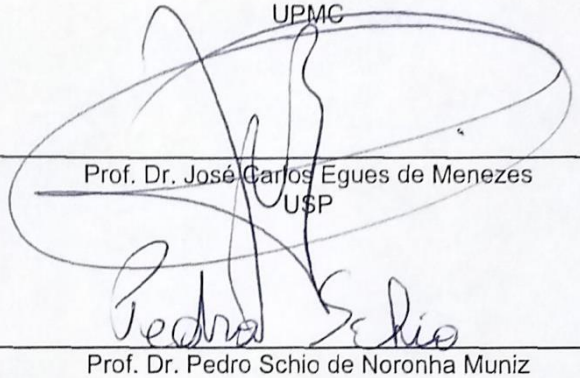

Prof. Dr. José Carlos Egues de Menezes
USP

Prof. Dr. Pedro Schio de Noronha Muniz
LNLS

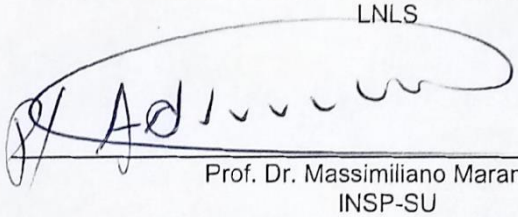

Prof. Dr. Massimiliano Marangolo
INSP-SU

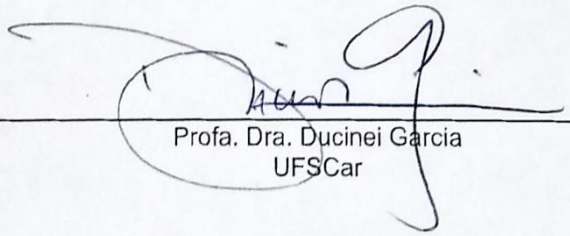

Profa. Dra. Ducinei Garcia
UFSCar

Certifico que a defesa realizou-se com a participação à distância do(s) membro(s) Andrea Gauzzi, Massimiliano Marangolo e, depois das arguições e deliberações realizadas, o(s) participante(s) à distância está(ao) de acordo com o conteúdo do parecer da banca examinadora redigido neste relatório de defesa.

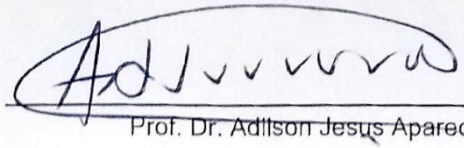

Prof. Dr. Adilson Jesus Aparecido de Oliveira

À Natalia, pelo tanto que crescemos durante esses anos.

Agradecimentos

No fim de mais essa etapa, gostaria de agradecer aos meus orientadores, Adilson Jesus Aparecido de Oliveira e Andrea Gauzzi, por todos esses anos de trabalho compartilhado, pelo acolhimento em seus laboratórios e grupos de pesquisa, pela amizade construída dentro e fora do trabalho, e por tudo que me ensinaram dentro e fora do mundo da pesquisa. Obrigado também ao Prof. Paulo Cesar de Camargo, pela ajuda e contribuições a esse trabalho e ao grupo de pesquisa como um todo. Meus agradecimentos também aos professores membros da banca, por sua disponibilidade e prontidão em avaliar esse trabalho. Meus sentimentos de profunda gratidão a todos os professores que me ensinaram e inspiraram ao longo de toda a minha vida. Num momento em que me preparo para me juntar a eles na docência, e em um momento em que professores são mais necessário do que nunca, espero poder encarar com humildade a tarefa de fazer jus a tudo o que fizeram por mim.

Agradeço aos colegas no Brasil, na França a na Itália que contribuíram e por vezes realizaram experimentos que culminaram nessa tese: Edmondo Gilioli pela produção das amostras no IMEM-CNR em Parma, Itália. A Yannick Klein pelas medidas de calor específico, Cristophe Bellin e Florent Perez pelo auxílio com as medidas de espectroscopia Raman. Agradeço também ao Prof. Guillaume Fiquet pelo acolhimento no *Institut de Minéralogie, de Physique des Matériaux et de Cosmochimie*. A Matteo d'Astuto, Alexei Bosak, Luigi Paolasini, e novamente a Cristophe Bellin pelo auxílio e suporte na realização dos experimentos no ESRF. A Mala N. Rao pelos cálculos utilizados na interpretação dos experimentos de IXS. A Driele von Dreifus por algumas medidas de magnetização. E finalmente a Flávio Paulo Milton por toda a ajuda e pelas medidas de corrente piroelétrica.

Gostaria de agradecer às agências de fomento que, direta ou indiretamente, contribuíram financeiramente para a realização desse trabalho: FAPESP (através dos projetos 2015/21206-1 e 2013/27097-4), CAPES, CNPq, CNRS, COFECUB e todas as outras agências de fomento à pesquisa e à ciência. Além do sincero agradecimento, ficam meus votos que todos os que promovem a ciência e todos que removem barreiras nos caminhos do conhecimento possam ter sua importância e seus esforços verdadeiramente reconhecidos nessa época de obscurantismo crescente.

Aos amigos do Grupo de Supercondutividade e Magnetismo, pelos trabalhado e pela convivência diária, o meu obrigado: Danusa, Marlon, Alexandre, Korllvary, Maycon, Fernanda, Helena, Otávio, Zé, Bárbara, Lincoln, Alberto, Raphael, Carlos, Pedro (novamente), Hugo e aos professores Fabiano e Ortiz. Pelo apoio técnico, agradeço a Claudio e Luiz, e também ao Igor, em especial, pela sua disponibilidade. Aos colegas do GMF, em

especial ao Flavio e a Professora Ducinei, o meu reiterado agradecimento.

Aos amigos do trabalho do outro lado do Atlântico, no *Institut de Minéralogie, de Physique des Matériaux et de Cosmochimie*. Marine, Andrea, Carlos, Gilbert, Betül, David, Alisha, Sam, Guilherme, Francesca, Ornella, Tommaso, Cesare, Silvia, Raffaello, Fred - Un trés grand merci!

Minha gratidão aos meus pais, minha família e minha irmã Natalia pelo seu amor e apoio incondicionais ao longo de toda a minha vida. Também a Ana, que chegou há pouco mas fez esse um fim de jornada mais leve e feliz, um caloroso obrigado.

Aos amigos que me acompanham há tanto tempo: Van, Junior, Leilson, Rafinha e Marcoleta, sou incapaz de expressar a alegria que foi tê-los ao lado durante a jornada. E aos amigos que conheci aqui em São Carlos: Guiga, Hindi, Lobo, Leo, Alo, Lazaro, Luigi, Santiago, Iann e Roberto Pina, o caminho sem vocês seria muito mais tortuoso e difícil.

Um agradecimento final também é necessário e todos os amigos da Associação São Carlos de Kendo. Meu carinhoso agradecimento aos senseis Yashiro, Harumi, Paulo, Kenji, Akemi, Anchieta e Gil, por todo o aprendizado proporcionado dentro e fora do dojo. Também pelo aprendizado, pela amizade, e pela companhia e esforço diário nos treinos, meu sincero obrigado a Gabi, Godinho, Ernesto, João Pedro, Danilo, Leonardo, Hyngrid, Andre, Elias, Ito, Matheus, Diego, Vitor, Ariel e Cintia.

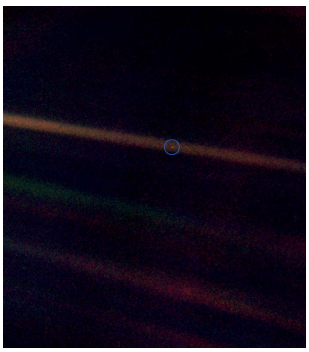

There is perhaps no better demonstration of the folly of human conceits than this distant image of our tiny world. To me, it underscores our responsibility to deal more kindly with one another, and to preserve and cherish the pale blue dot, the only home we've ever known.

- Carl Sagan, Pale Blue Dot, 1994

Abstract

In this work we study the quadruple perovskite structure ($AA'_3B_4O_{12}$) manganese oxides $(NaMn_3^{3+})(Mn_2^{3+}Mn_2^{4+})O_{12}$ e $(LaMn_3^{3+})Mn_4^{3+}O_{12}$ under the point of view of the existence of multiferroicity, magnetoelectric coupling, and also structure anomalies on $NaMn_7O_{12}$. These studies range from the existence to the mechanism of the establishment of multiferroicity and coupling between ferroic orders in these materials. The driving force of the dynamic structural anomalies in $NaMn_7O_{12}$ are also studied with the goal of clarifying the mechanisms of structural distortion and how they relate to the onset of ferroic orders.

The different valence states create a fruitful environment to study the importance of electronic degrees of freedom of structural, magnetic, and ferroelectric ones. While $LaMn_7O_{12}$ is single valent, only possessing Mn^{3+} ions, $NaMn_7O_{12}$ present a charge unbalance, having half of the B-site manganese ions in Mn^{3+} state and half in the Mn^{4+} one. Both can be compared to the intermediate case of $(CaMn_3^{3+})(Mn_3^{3+}Mn_1^{4+})O_{12}$, in which the valence disproportion between Mn^{3+} and Mn^{4+} is 3:1. Both compounds go through a cubic $Im\bar{3}$ to monoclinic $I2/m$ structure, which for $NaMn_7O_{12}$ is accompanied by a total charge ordering and commensurate structural modulation in the $\left(\frac{1}{2}, 0, -\frac{1}{2}\right)$ direction. Magnetically, both materials present antiferromagnetic ordering of the manganese ion sublattice in the A' and B sites. In both cases the sublattices order at distinct temperatures.

These manganites are synthesized under high pressures and temperatures by Prof. Andrea Gauzzi's group at *Institut de Minéralogie, de Physique des Matériaux et de Cosmochimie* at Sorbonne Université, in Paris, France. The characterization of samples involved specific heat, Raman spectroscopy, inelastic x-ray scattering (IXS) and diffuse x-ray scattering (DXS), DC magnetometry and pyroelectric current measurements. To search for magnetoelectric coupling, magnetoelectric susceptibility measurements, DC magnetometry under electric fields, and pyroelectric current measurements under magnetic field are used.

The results of IXS and DXS experiments show interesting dynamical anomalies in $NaMn_7O_{12}$'s structural transition, a softened phonon driven by the Jahn-Teller mechanism dominates over a different short range distortion that was unveiled by DXS experiments. This shows the importance of the JT mechanism in the structural stabilization of the monoclinic phase and generate an interesting scenario for comparison with $CaMn_7O_{12}$ results in similar experiments.

Results of Raman spectroscopy experiments, by showing anomalies in certain phonon frequencies during magnetic phase transitions, point to the coupling of magnetic and elastic properties $NaMn_7O_{12}$. The changes in specific heat in $NaMn_7O_{12}$ samples

when exposed to magnetic fields, especially in low temperatures, also emphasizes this point.

In fact, a ferroelectric transition was found simultaneous to anomalies in specific heat and magnetization in $NaMn_7O_{12}$. Particularly, magnetic hysteresis loops are quite wider in the ferroelectric phase, although previous work rule out the presence of new magnetic order. These properties are explained in function of a magnetoelectricity mediated antiferromagnetic domain wall ordering model.

As for $LaMn_7O_{12}$, a ferroelectric transition was found at the B site antiferromagnetic transition temperature, allowing for an interesting contrast between its multiferroic properties and those of $NaMn_7O_{12}$. Besides the particularities of each system, structural and magnetic properties imply that their ferroelectricity is of magnetic origin through the exchange striction mechanism. That way, both $(NaMn_3^{3+})(Mn_2^{3+}Mn_2^{4+})O_{12}$ and $(LaMn_3)Mn_4O_{12}$ can be added to the class of multiferroic materials.

Keywords: Multiferroic materials. Magnetoelectric coupling. Manganites. Quadruple perovskites.

Resumo

Nesse trabalho são estudados os óxidos de manganês $(NaMn_3^{3+})(Mn_2^{3+}Mn_2^{4+})O_{12}$ e $(LaMn_3^{3+})Mn_4^{3+}O_{12}$, que tem estrutura de perovskita quádrupla ($AA'_3B_4O_{12}$), sob os pontos de vista da existência de multiferroicidade, do acoplamento magnetoelétrico, assim como anomalias estruturais dinâmicas no $NaMn_7O_{12}$. Esses estudos abrangem desde a existência, assim como os mecanismos do estabelecimento de multiferroicidade e acoplamento entre ordens ferróicas nesses compostos. As forças motrizes por trás das anomalias estruturais dinâmicas no $NaMn_7O_{12}$ também são estudadas no sentido de esclarecer os mecanismos de deformação estrutural e como eles se envolvem no estabelecimento das ordens ferróicas.

A diferença de estados de valência fornece um ambiente fortuito para o estudo da importância dos graus de liberdade eletrônicos sobre as propriedades estruturais, magnéticas e ferroelétricas. Enquanto $LaMn_7O_{12}$ é monovalente, apresentando apenas íons Mn^{3+}, $NaMn_7O_{12}$ apresenta um desequilíbrio de valência, com metade dos íons de manganês do sítio B no estado Mn^{3+} e metade no estado Mn^{4+}. Ambos podem ser comparados ao caso intermediário do já estudado $(CaMn_3^{3+})(Mn_3^{3+}Mn_1^{4+})O_{12}$, em que a desproporção entre Mn^{3+} e Mn^{4+} é de 3:1. Ambos os compostos passam por uma transição de uma estrutura cúbica $Im\bar{3}$ para monoclínica $I2/m$, sendo que no caso do $NaMn_7O_{12}$ a transição é acompanhada por um ordenamento completo de carga e de uma modulação estrutural comensurada na direção $\left(\frac{1}{2}, 0, -\frac{1}{2}\right)$. Magneticamente, ambos os compostos apresentam ordenamentos antiferromagnéticos das subredes de íons de manganês nos sítios A' e B. Nos dois casos as subredes se ordenam em temperaturas distintas.

Essas manganitas foram fabricadas sob altas pressões e temperaturas pelo grupo do Prof. Andrea Gauzzi, no *Institut de Minéralogie, de Physique des Matériaux et de Cosmochimie* na Sorbonne Université, em Paris, França. Os métodos de caracterização envolvem calor específico, espectroscopia Raman, espalhamento inelástico de raios-x (IXS), espalhamento difuso de raios-x (DXS), magnetometria DC e corrente piroelétrica. Para detectar o acoplamento magnetoelétrico, medidas de suscetibilidade magnetoelétrica, magnetometria DC sob campos elétricos e corrente piroelétrica sob campos magnéticos são utilizadas.

Os resultados dos experimentos de IXS e DXS mostram interessantes anomalias dinâmicas na transição estrutural do $NaMn_7O_{12}$, um fônon suavizado gerado pelo mecanismo de Jahn-Teller sobrepuja outra distorção de curto alcance detectada via DXS. Isso mostra o o papel fundamental desse mecanismo na estabilização estrutural da fase monoclínica e geram um quadro de interessante comparação com resultados do $CaMn_7O_{12}$ em experimentos semelhantes.

Os resultados das medidas de espectroscopia Raman, ao apresentar anomalias nas frequências de certos fônons durante as transições de fase magnéticas, apontam para o acoplamento entre propriedades magnéticas e elásticas do $NaMn_7O_{12}$. A variação do calor específico de amostras de $NaMn_7O_{12}$ quando expostas a campos magnéticos, especialmente a baixas temperaturas, enfatiza esse acoplamento.

De fato, uma transição ferroelétrica foi encontrada simultaneamente a anomalias no calor específico e na magnetização do $NaMn_7O_{12}$. Particularmente, curvas de histerese magnética são bastante mais largas na fase ferroelétrica, embora trabalhos anteriores descartem a presença de novo ordenamento magnético. Essas propriedades são explicadas em função de um modelo de ordenamento das paredes de domínio antiferromagnéticas do $NaMn_7O_{12}$, que é ligado a magnetoeletricidade.

No caso do $LaMn_7O_{12}$, uma transição ferroelétrica foi encontrada na temperatura de transição antiferromagnética do sítio B, permitindo um interessante contraste entre suas propriedades multiferróicas e as do $NaMn_7O_{12}$. Apesar das peculiaridades de cada sistema, as propriedades estruturais e magnéticas permitem afirmar que a ferroeletricidade tem origem magnética através do mecanismo de estricção de troca. Dessa forma $(NaMn_3^{3+})(Mn_2^{3+}Mn_2^{4+})O_{12}$ quanto $(LaMn_3)Mn_4O_{12}$ podem ser adicionados à categoria dos materiais multiferróicos.

Palavras-chave: Materiais multiferróicos. Acoplamento magnetoelétrico. Manganitas. Perovskitas quadruplas.

Résumé

Dans cette thèse on étude les oxydes de manganèse $(NaMn_3^{3+})(Mn_2^{3+}Mn_2^{4+})O_{12}$ et $(LaMn_3^{3+})Mn_4^{3+}O_{12}$, qu'appartiennent à la structure de pérovskite quadruple $(AA'_3B_4O_{12})$, sous les points de vue de l'existence de multiferroïcité, de la couplage magnétoélectrique, et aussi des anomalies structurels dynamiques en $NaMn_7O_{12}$. Ces études concernent l'existence, les mécanismes d'établissement de la multiferroïcité et le couplage entre les ordres ferroïques en ces matériaux. Les forces motrices des anomalies structurels dynamiques en $NaMn_7O_{12}$ sont aussi étudiés au sens de clarifier les mécanismes de déformation structurel et quel est son importance au établissement des ordres ferroïques.

La différence entre les états de valence fournisse un environnement avantageux pour l'étude de l'importance des degrés de liberté électroniques sur ceux structurels, magnétiques et ferroélectriques. Au pas que $LaMn_7O_{12}$ est monovalent, ne présentant que des ions Mn^{3+}, $NaMn_7O_{12}$ présente un déséquilibre de valence, avec moitié des ions de manganèse au site B à l'état Mn^{3+} et l'autre l'état Mn^{4+}. Les deux peuvent être comparés au cas intermédiaire du déjà étudie $(CaMn_3^{3+})(Mn_3^{3+}Mn_1^{4+})O_{12}$, auquel la disproportion entre Mn^{3+} et Mn^{4+} est de 3 :1. Les deux matériaux passe par une transition d'une structure cubique $Im\bar{3}$ a une monoclinique $I2/m$, et au cas du $NaMn_7O_{12}$ la transition est accompagné par un ordonnément complète de charge et par une modulation structurel commensurable vers la direction $\left(\frac{1}{2}, 0, -\frac{1}{2}\right)$. Par rapport de la structure magnétique, les deux composées présentent ordonnément antiferromagnétique des sous-réseaux des ions manganèse aux sites A' et B. Aux deux cas, les sous-réseaux s'ordonnent en températures différents.

Ces manganites sont fabriqués au *Institut de Minéralogie, de Physique des Matériaux et de Cosmochimie* à l'Université Sorbonne à Paris, France. Les méthodes de caractérisation comprendre chaleur spécifique, spectroscopie Raman, la dispersion inélastique de rayons-x (IXS), la dispersion diffuse de rayons-x (DXS), magnétométrie DC, courant pyroélectrique. Pour investiguer le couplage magnétoélectrique, manipulations de susceptibilité magnétoélectrique, magnétométrie DC sous champ électrique et courant pyroélectrique sous champ magnétique sont utilisés.

Les résultats des manipulations de IXS et DXS révèlent anomalies dynamiques dans la transition structurel du $NaMn_7O_{12}$. Un phonon amollit engendré par le mécanisme de Jahn-Teller domine sur une autre distortion de courte longueur. Ce que montre le rôle fondamental de ce mécanisme pour l'stabilisation structurel de la phase monoclinique e engendre un intéressant cas de comparaison avec les résultats du $CaMn_7O_{12}$ en manipulations similaires.

Les résultats de la spectroscopie Raman, en présentant anomalies à la fréquence de certains phonons en croisant les températures de transition de phase magnétique, suggère

le couplage entre les propriétés magnétiques et élastiques du $NaMn_7O_{12}$. La variation de la chaleur spécifique d'échantillons de $NaMn_7O_{12}$ exposés à champs magnétiques, surtout en basses températures, souligne la possibilité de couplage.

En effet, une transition ferroélectrique a été trouvé simultanément à anomalies dans la chaleur spécifique et dans la magnétisation du $NaMn_7O_{12}$. Particulièrement, les courbes d'hystérésis magnétique sont bien plus larges dans la phase ferroélectrique, bien études précédant élimine la possibilité de nouveau ordonnément magnétique. Ces propriétés sont expliquées dans le cadre d'un modelé de ordonnément de frontières de domaine antiferromagnétique en $NaMn_7O_{12}$, qui est lié à la couplage magnétoélectricité.

Au cas du $LaMn_7O_{12}$, une transition ferroélectrique a été trouvé à la température de transition antiferromagnétique du site B, permettant un intéressant contraste entre ses propriétés multiferroïque et ceux du $NaMn_7O_{12}$. Malgré les péculiarité de chaque système, ses propriétés structurels et magnétiques permettent d'affirmer qui sa ferroélectricité est d'origine magnétique travers le mécanisme de striction d'échange. Donc, $(NaMn_3^{3+})(Mn_2^{3+}Mn_2^{4+})O_{12}$ et $(LaMn_3)Mn_4O_{12}$ peuvent être rajouté à la catégorie des matériaux multiferroïques.

Mots-clés : Matériaux multiferroïques. Couplage magnétoélectrique. Manganites. Pérovskites quadruples.

List of Figures

List of Tables

Contents

1 Introduction

A very current technological challenge in the design of new devices regards the development of materials that can be tailored to perform multiple functions. This class of material, called multifunctional materials, are capable of producing more the one response from a single stimulus, *i.e.*, a material that produces electric polarization and magnetization when applied a magnetic field, and a precise control of their responses and properties is highly desirable. There is a wide variety of conceivable multifunctional materials, some of which exemplified in the diagram in figure 1.1. A particular case of this multifunctional class of material is that of the materials with more than one ferroic order, a long-range order with spontaneous responses. Prime examples of ferroic orders are ferroelectric, ferroelastic and ferromagnetic materials. Other types of ordering, like antiferromagnetism, are also included. Materials with more than one ferroic order are

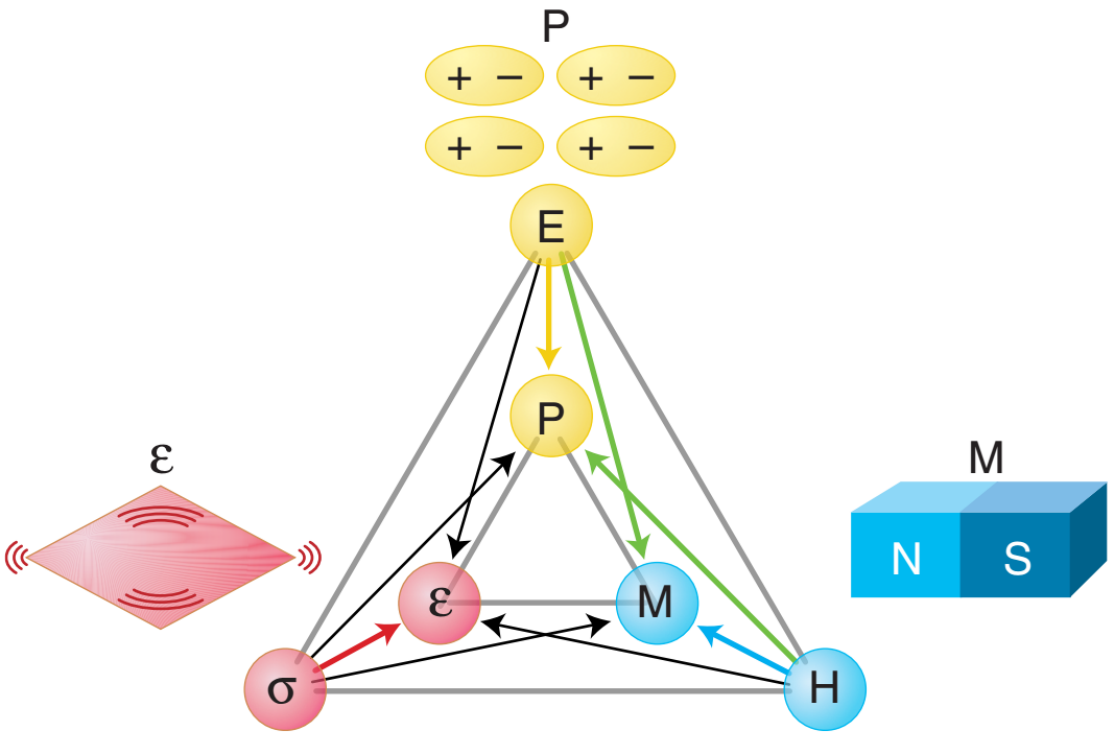

Figure 1.1 – Diagram showing some forms of multifunctional materials. The stimuli stress (σ), electric (E) and magnetic (H) fields control the responses strain (ϵ), polarization (P) and magnetization (M). Red, yellow and blue arrow represent the ordinary material response, green and black arrows represent multifunctional responses. Green arrows represent magneto electric responses. Adapted from [1].

called multiferroic materials. Because ferroelectricity usually involves coupling lattice distortions, elastic, magnetic and electric are usually the degrees of freedom that interact in these materials. In particular, and because of their wide usage in electronic applications, materials that couple electric and magnetic properties are wanted for a wide range of applications [1–5]. These materials are called magnetoelectric.

There is sometimes confusion about the meaning of the terms "magnetoelectric" and "multiferroic". For clarification, in this work the convention established by Eerenstein, Mathur and Scott[2] will be used, as shown in figure 1.2. The term "multiferroic" will be used to denote all materials that have two ferroic orderings, even if completely independent and uncoupled, represented by the area shaded in red in figure 1.2. The term "magnetoelectric" will be used to denote every material in which electric polarization and magnetization are coupled, even if no ferroic order is present. Evidently, the most desirable effect is to find magnetoelectric multiferroic materials.

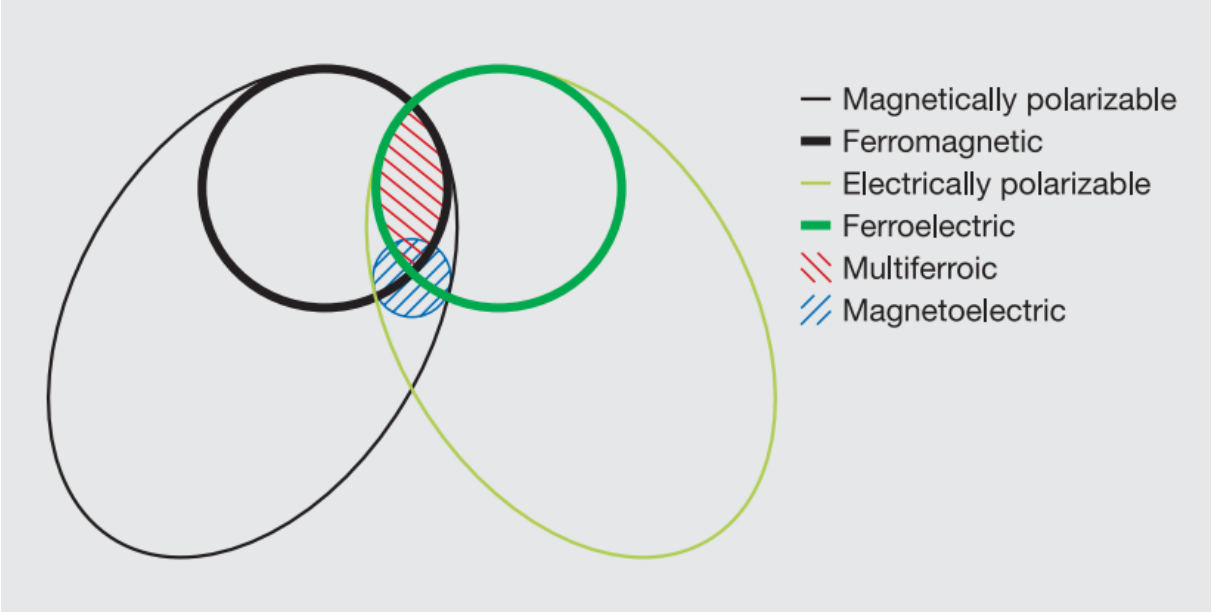

Figure 1.2 – Venn diagram clarifying the meaning of the terms "multiferroic" and "magnetoelectric". Adapted from [2].

There are several technological applications that would be brought into viability by robust magnetoelectric multiferroic materials. On the field of storage devices, there are concepts for higher states memory devices [6], as well as magnetic memories electrically written [1, 5, 7]. Magnetoelectric materials with high sensibility to magnetic fields can be used to produce low-cost precise magnetic sensors [5, 7]. Microwave and radio frequency electronics would also benefit from filter and antennas made with magnetoelectric materials [5, 7]. The area of spintronics would specially benefit to materials that couple electric and magnetic degrees of freedom. Spin valves and spin filters would also join the set of devices that could be realized by this kind of material [5, 8, 9]. Finally, wireless energy transfer,

energy-saving and energy harvesting applications of magnetoelectric materials have also been proposed [5].

The magnetoelectric effect in oxides were first described more than fifty years ago [10, 11], but in the last decade, its discovery in new materials have attracted renewed interest [1–3]. One approach to multiferroicity is to combine ferroelectric and ferromagnetic materials with large coupling to elastic properties (that is, piezoelectric and magnetostrictive materials). This approach not only allows not make use of optimal materials of each group, relieving the burden of finding the same effect in a single-phase material, but also, through modern synthesis techniques, it also creates the possibility of manipulation of patterns in the materials, controlling its mechanical coupling and anisotropy. Examples of different configuration in these composite materials are particulate materials in a matrix, layered structures and fibrous composites [2, 3, 12, 13]. For more than a decade, a fruitful partnership between The GSM (Magnetism and Superconductivity Group) and GMF (Ferroic Materials Group) research groups at UFSCar Physics Department produced several studies into the synthesis, properties and coupling mechanism of multiferroic composite materials [14–21].

Nevertheless, many single-phase materials also show magnetoelectric effect and multiferroicity. An example that has become notorious in recent years for presenting these properties at room temperature is the Bismuth ferrite $BiFeO_3$ [22]. Other examples of single phase multiferroics include other rare-earth ferrites like $DyFeO_3$ and $GdFeO_3$ [23], layered structure ferrites and manganites RFe_2O_5 and RMn_2O_5 with R a rare earth metal [23, 24]. Other, more complex structures are also present this effect, like $TbPO_4$, $HoBaNiO_5$, $CaBaCo_4O_7$ and $Ba_{0.52}Sr_{2.48}Co_2Fe_{24}O_{41}$ [5, 6, 25].

Besides the RMn_2O_5 family, another family of manganites attracts much attention because of their many interesting properties, like magnetoresistance [26] and for showing multiferroic properties [23, 27–30]. The perovskite structure $RMnO_3$ manganites have shown multiferroicity for several rare earth metals in the R position, like Dy, Ho and Tb [23, 27, 29]. However, these simple perovskite compounds usually present much more complex distortions than the pristine perovskite cell presented in figure 1.3 [23, 27, 27–30]. Besides, the possibility of oxygen defects in many of them, make chemical disorder another obstacle into interpreting results and separating competing mechanisms of the multiferroic, or even other properties, like magnetic ones.

A different perovskite-like structure offers an interesting alternative in the study of manganites. First described by Marezio et al.[31] in 1973, the quadruple perovskite structure can be seen in figure 1.3. It is usually stabilized under high pressures [31–33], but some quadruple perovskite can also be produced by chemical routes under room pressures [34,35]. This structure is usually more symmetrical than simple perovskites counterparts. It is also denser and has simpler distortions. The enhanced density is achieved through large

rigid tilting of BO_6 octahedra. Given the importance of octahedra tilting as a mechanism for ferroelectricity [36–38], the finding of electric order in some materials of this class is expected. Finally, the oxygen in the $AA'_3B_4O_{12}$ usually has higher coordination and crystallizes in very symmetrical crystallographic positions, making this structure practically free from oxygen defects, reducing the disorder coming from oxygen deficiencies [31, 32].

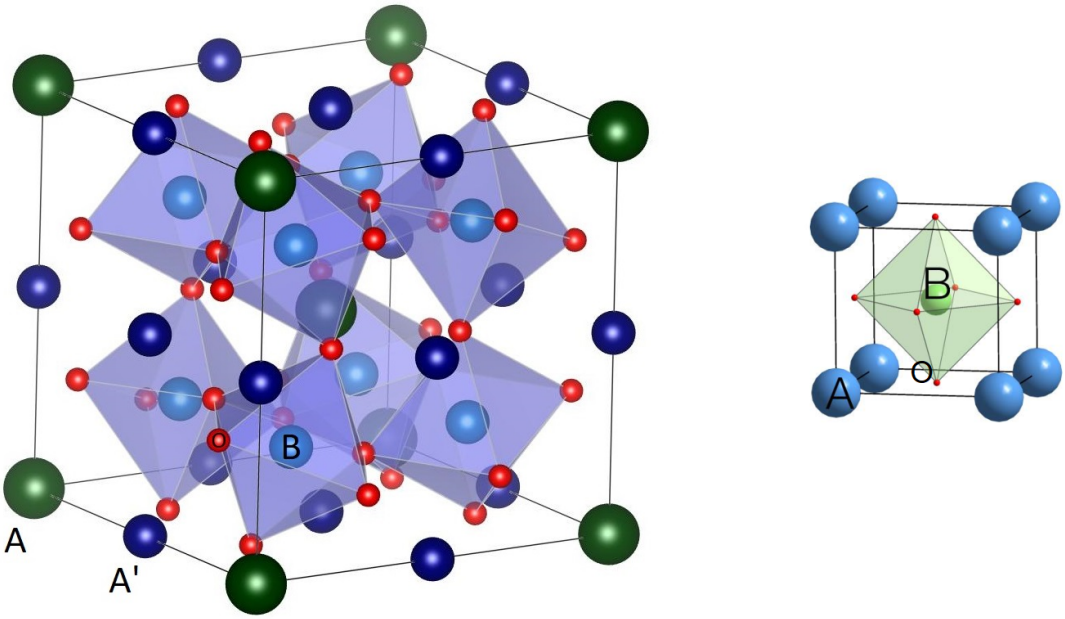

Figure 1.3 – Right: Simple perovskite structure ABO_3. Left: Quadruple perovskite structure $AA'_3B_4O_{12}$. Oxygen shown in red in both structures.

Quadruple perovskite manganites are obtained when the A' and B sites are occupied by Mn ions ($AMn_3Mn_4O_{12}$ or AMn_7O_{12} for simplicity) and multiferroicity is also present in this class of materials, $BiMn_7O_{12}$ being one example [39]. In this structure, mixed valence can have very interesting effect, since the valence of the A site ion can affect the proportion of Mn^{3+} and Mn^{4+} ions without the inherent disorder brought by doping. The divalent Ca in the A-site leads to the very interesting case of $(CaMn_3^{3+})(Mn_3^{3+}Mn^{4+})O_{12}$, which was shown to be multiferroic with the very large value of electric polarization of 0.27 $\mu C/cm^2$, which is stabilized by its spiral spin structure [34, 35]. It also goes through an incommensurate modulation of its structure that appears as short-range order much before the transition is properly realized [40]. This makes $CaMn_7O_{12}$'s distortion very interesting to study from the point of view of interplay between lattice, orbital and spin degrees of freedom. The complicated incommensurate structure, however, is a challenge to the understanding of the underlying mechanisms of these distortions.

In this thesis, we study the quadruple perovskite manganites $(LaMn_3)Mn_4O_{12}$ and $(NaMn_3)(Mn_2^{3+}Mn_2^{4+})O_{12}$ from the point of view of multiferroicity. A simpler, commensurate modulation found in $NaMn_7O_{12}$ also allows for the study of its causes and

mechanisms in a more favorable way than $CaMn_7O_{12}$. The performed studies in both $(LaMn_3)Mn_4O_{12}$ and $(NaMn_3)Mn_4O_{12}$ comprise magnetization, magnetoelectric susceptibility and pyroelectric current measurements, including measurements under electric field. Additionally, to further study structural properties and anomalies in $(NaMn_3)Mn_4O_{12}$, it also was studied by Raman spectroscopy, diffuse x-ray scattering, inelastic x-ray scattering, and specific heat measurements.

Important results on the structural properties of $NaMn_7O_{12}$ were revealed by the diffuse x-ray scattering (DXS) experiments and inelastic x-ray scattering (IXS) experiments. We have been able to detect two competing structural distortions during the cubic to monoclinic transition. The prevalent distortion was found to be a Jahn-Teller driven phonon. This finding significantly advances the understanding of the driving forces of this kind of structural distortion, putting the Jahn-Teller mechanism at a key spot in its ensuing. These results are also described on a paper that is essentially ready for submission [41].

On the multiferroicity front, both $NaMn_7O_{12}$ and $LaMn_7O_{12}$ have been found to be multiferroic. The multiferroic transition in $LaMn_7O_{12}$ was found to be simultaneous the antiferromagnetic transition of the B-site ions, and we find some evidence that favors the hypothesis of coupling between electric and magnetic orders. These results are described in a paper in submission process [42]. In contrast, the ferroelectricity $NaMn_7O_{12}$ is found below the ordering temperature of both B and A' sites. There is no new magnetic ordering at this temperature, but important magnetic and elastic anomalies are present at this transition, evidencing the possibility of coupling also in this material. These results are also to be published in a paper which is currently being written.

The thesis is structured as follows: the next chapter explore the theoretical foundations necessary in the study. Chapter 3 presents the experimental methods necessary to the development of the thesis. Chapters 4 and 5 present the results of the experiments in $(LaMn_3)Mn_4O_{12}$ and $(NaMn_3)Mn_4O_{12}$, respectively. Chapter 6 presents a discussion and further interpretation of the main aspects of the results. Finally, the conclusions are presented in chapter 7.

2 Theoretical Fundamentals

2.1 Magnetic and Structural Mechanisms in Manganites

The main mechanism for the exchange interaction in Manganese oxides is called the *superexchange interaction*. Because of the presence of the oxygen ions between the metallic cations, there is almost no overlap between the electronic wavefunctions of the Mn ions, and therefore direct exchange plays a very reduced role.

Instead, there is orbital overlap between the Mn d orbitals and the p orbitals in oxygen, forming an excited $3d^{n+1}2p^5$ exited state through the virtual transfer of one electron to each cation [43]. The exchange between the electrons forming the excited state mediates the exchange between the Mn ions through the antiparallel pairing of electrons in the oxygen p orbital, as shown in figure 2.1.

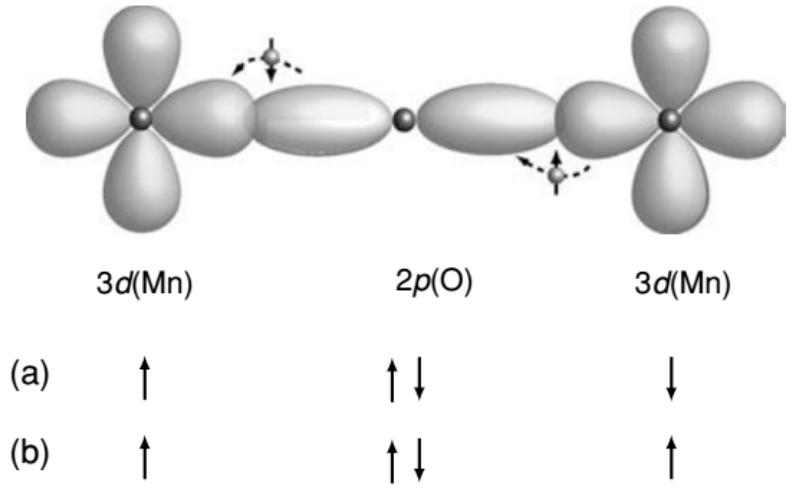

Figure 2.1 – Typical superexchange mechanism in a $Mn - O - Mn$ bond. Dashed arrows show virtual electron transfer. Because of the direct exchange between O and Mn electrons, the configuration a) is of lower energy than b). Adapted from [43].

As the figure shows, this type of linear bond leads to antiferromagnetic coupling of the metallic ions. However, there is a very strong dependence of bond distance and angle. The relative position of the ligand also plays a larger role. This can be easily seen comparing panels a and b of figure 2.2. In panel b of figure 2.2, a case in which the wavefunction overlap is require by symmetry to vanish, leaving the weaker direct exchange

to dominate and create a ferromagnetic coupling between the Mn ions [44]. [45, 46]

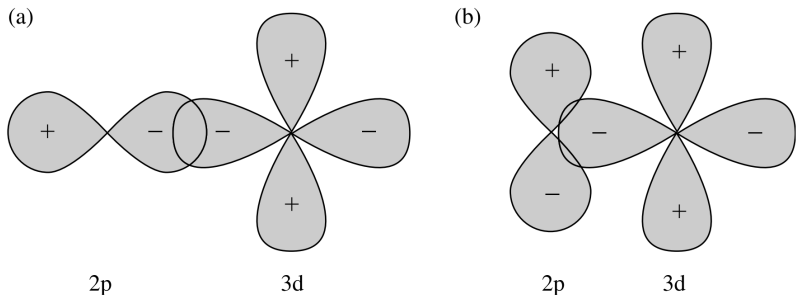

Figure 2.2 – a) Non-zero wavefunction overlap that favors antiferromagnetic coupling. b) Symmetry required zero wavefunction overlap that favors ferromagnetic coupling. Adapted from [44].

Another mechanism for magnetic exchange in oxides is the *double exchange* mechanism. This interaction requires mixed valence cations in sites through which the surplus electrons can hop. In each site the extra electron obeys Hund's rule, and by hopping to different sites they become the medium of and effective ferromagnetic exchange interaction. However, for being dependent on electron hopping, this mechanism becomes dependent on the electrical conductivity of the oxide.

Given the diversity of exchange mechanisms involved, from direct exchange to double and superexchange, the prediction of magnetic structures in manganites in a difficult task. The work of Goodenough[46] delves deeply into the competing interactions and how they depend on bond distance and angle, consolidating the different coupling types into the Goodenough-Kanamori-Anderson (GKA) rules, through which many aspects of magnetic structure in oxides can be predicted.

There is a very important mechanism for structural stabilization in manganites that links lattice and electronic degrees of freedom, being usually implicated in structural and elastic anomalies in these materials. The crystal field splitting is a very strong way into which lattice interact with electronic properties. The splitting of the d orbitals in a octahedral coordination separates the higher energy e_g level (corresponding to the d_{z^2} and $d_{x^2-y^2}$ orbitals) and the lower energy t_{2g} levels (corresponding to the orbitals d_{xy}, d_{xz} and d_{yz}), as shown in figure 2.3. The energy splitting can be understood in function of electrostatic repulsion between the transition metal electron and the negatively charged O^{2-} at the vertexes of the octahedra, it's seen from figure 2.3 that the electrons in the low energy orbitals are on average more distant to the oxygen than their high energy counterparts.

It is attributed to Jahn and Teller[47] the insight that apical elongation or compression in that picture can lead to a permanent structural distortion. When compressed or elongated, the energy of the d orbitals shift, further lifting the degeneracy as the apical

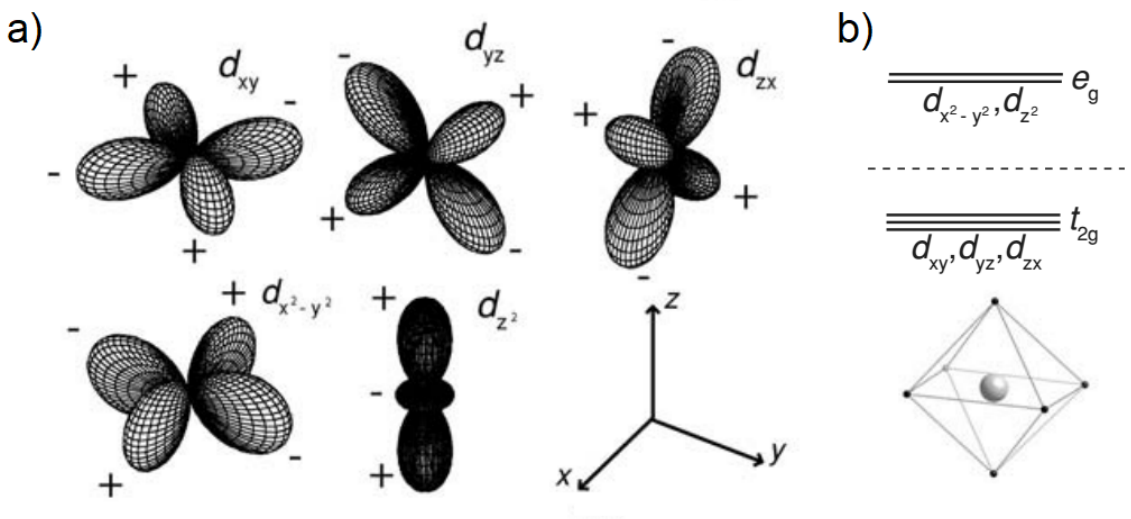

Figure 2.3 – d orbitals (a) and energy levels for octahedral crystal field splitting (b). Adapted from [43].

O^{2-} get farther or closer to the probable position of the electrons, the further splitting of the energy levels under this tetragonal distortion is shown in figure 2.4. For small distortion, the energy gain of distorting the octahedra is proportional to the strain ϵ, while the elastic energy cost of the distortion is quadratic in ϵ. This leads to a variation in energy $\delta E = -A\epsilon + B\epsilon^2$, leading to an equilibrium distortion $\epsilon^{(0)} = B/A$ [43].

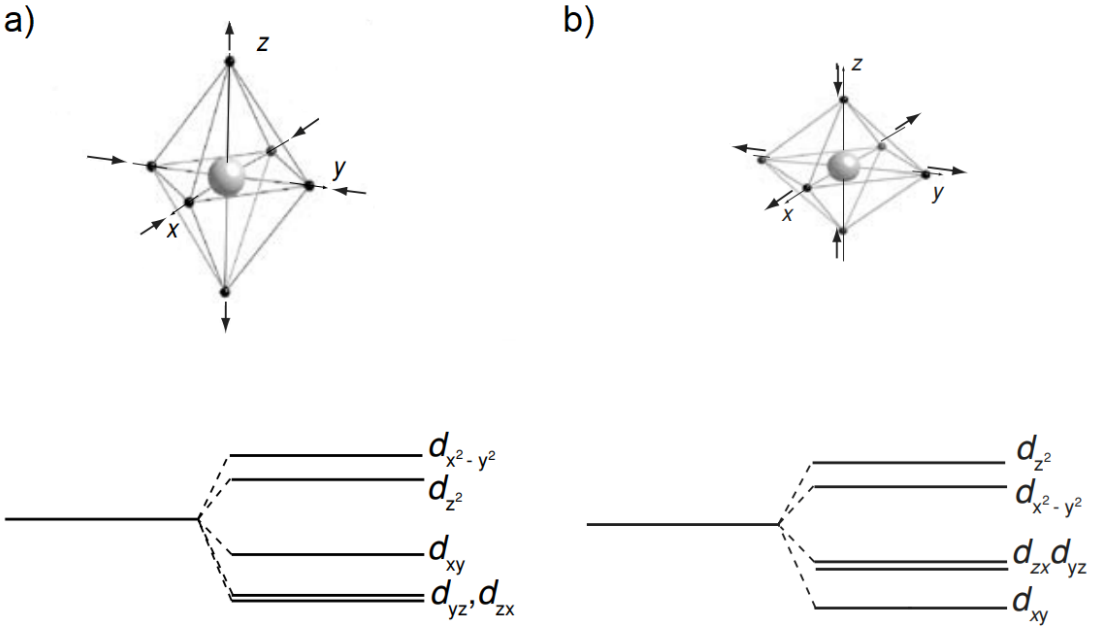

Figure 2.4 – d orbital energy level splitting of e_g (d_{z^2} and $d_{x^2-y^2}$) and t_{2g} (d_{xy}, d_{xz} and d_{yz}) for elongated (a) and compressed (b) octahedral coordination. Adapted from [43].

This can be a particularly efficient distortion stabilization mechanism for ions like the d^9 Cu^{2+} and, more importantly for this work, it is very effective for the d^4 Mn^{3+} since all four t_{2g} electron favor the lifting of the degeneracy. Particularly for the material studied in this work, the Jahn-Teller mechanism is the main source of the structural distortion in the single valence $LaMn_7O_{12}$ and the interplay between the $Mn^{3+/4+}$ has to be considered as one of the driving forces in its structural distortion and modulation.

2.2 Basic Aspects of Multiferroicity and Magnetoelectricity

There is some degree of incompatibility between the most usual kinds of ferroelectric materials and ferromagnetic ordering [4]. The most common mechanism of proper ferroelectricity, *i. e.* ferroelectricity in which the polarization is the order parameter in the ferroelectric phase transition, involves an empty d shell transition metal bonding with surrounding oxygen ions, forming electric dipoles in the process. A prime example is $BaTiO_3$. On the other hand, the usual mechanism for the ferromagnetic exchange interaction depends on the virtual hopping of electrons occupying the partly filled d shell of neighboring ions. For that reason, the same ion cannot perform both functions in the lattice, making these ordering mutually exclusive in this way [4].

One solution is to have to distinct ions performing the two functions, as in the case of $BiMnO_3$. The Mn ions order ferromagnetically and the lone pair of $6s$ electrons in Bi moves away from the centrosymmetric position in the oxygen surrounding, creating the dipoles for the proper ferroelectric ordering. However, different ions beings responsible for different orderings often generate a scenario of weak coupling, and $BiMnO_3$ can be considered a multiferroic, but not magnetoelectric material in the definition given by Eerenstein, Mathur and Scott[2]. An important exception to that rule is the Bismuth ferrite $BiFeO_3$, that shows ME coupling at room temperature [22].

There are, however, several mechanisms in which magnetic order (not restricted to ferromagnetism) can cause and be coupled to improper ferroelectricity. This is the case in which the polarization is not the order parameter in the phase transition [48]. In this type of ferroelectric, polarization arises as consequence of a structural transition, of charge ordering (electric polarization in magnetite during the much studied Verwey transition being an important example [49]), or of magnetic ordering [4]. In particular, mechanisms in which magnetic order can cause improper ferroelectricity will be discussed in section 2.3, since they are the most likely mechanisms to achieve robust coupling.

The symmetry properties that are inherent to the magnetic and electric orderings give powerful insight into which materials and crystalline space group can harbor the phenomenon of multiferroicity [2, 4]. The relations between the ordering and symmetry is shown in figure 2.5. The simplistic picture of a magnetic moment, a charge in a small circular

orbit, shows that the magnetic moments break time symmetry, their sign changes under time inversion. From the analogous picture of electric dipoles being spatially separated charges, it can be seen that they break spatial symmetry, changing sign under spatial inversion. It is the required that a material breaks both time and spatial symmetry at the same time in order to admit multiferroicity. That way, the materials that present multiferroicity must belong to space groups that break both spatial and temporal symmetries [3].

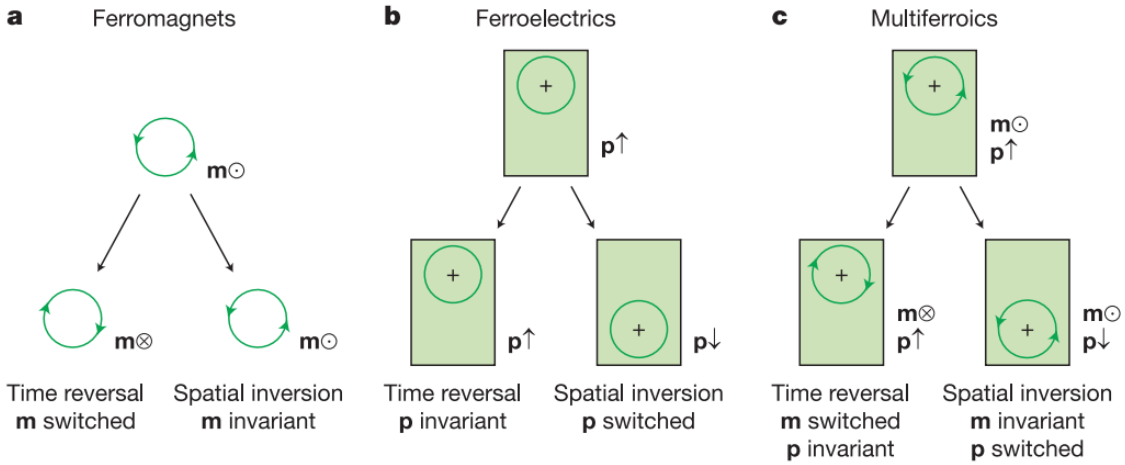

Figure 2.5 – Temporal and spatial symmetries broken by magnetically ordered (a), electrically ordered (b) and multiferroic (c) materials. Adapted from [2].

One simple, phenomenological way to model magnetoelectric coupling is by applying Landau theory to write the free energy F in terms of the electric and magnetic fields of components E_i and H_i, respectively [2]. Therefore, in S. I. units, and in absence of hysteresis, that free energy can be expressed up to third order as

$$-F(E,H) = \frac{1}{2}\epsilon_0\epsilon_{ij}E_iE_j + \frac{1}{2}\mu_0\mu_{ij}H_iH_j + \alpha_{ij}E_iH_j + \frac{\beta_{ijk}}{2}E_iH_jH_k + \frac{\gamma_{ijk}}{2}H_iE_jE_k + \cdots \quad (2.1)$$

Where ϵ_0 and μ_0 are the permittivity and permeability of free space, respectively. The two first terms describe the usual responses to an electric and magnetic field through the relative permittivity (ϵ_{ij}) and permeability (μ_{ij}) tensors. The tensor α_{ij} is called the magnetoelectric tensor, and describes the linear coupling between the electric and magnetic fields in the material. The second order tensors β_{ijk} and γ_{ijk} are called the quadratic magnetoelectric tensors. The model can be extended to ferroic materials by incorporating the spontaneous ordering of magnetization and polarization, and this can be accomplished by admitting that $\epsilon_{ij}(T)$ and $\mu_{ij}(T)$ (and also the magnetoelectric tensors, in fact), beyond varying with temperature, also have hysteretic behavior with respect to the fields.

The electric polarization P_i and magnetization M_i can be calculated via the relations $P_i = -\frac{\partial F}{\partial E_i}$ and $\mu_0 M_i = -\frac{\partial F}{\partial H_i}$

$$P_i = \epsilon_0 \epsilon_{ij} E_j + \alpha_{ij} H_j + \frac{\beta_{ijk}}{2} H_j H_k + \frac{\gamma_{ijk}}{2} H_j E_k + \cdots \tag{2.2}$$

$$\mu_0 M_i = \mu_0 \mu_{ij} H_j + \alpha_{ij} E_j + \frac{\beta_{ijk}}{2} E_j H_k + \frac{\gamma_{ijk}}{2} E_j E_k + \cdots \tag{2.3}$$

These equations show that even though in first order the magnetoelectric coupling must be dominated by the same coefficient (α_{ij}), the higher order and mixed components can cause very different magnetoelectric responses in polarization and magnetization. It is very important to remark that single phase magnetoelectric materials have a theoretical upper bound to the magnitude of their magnetoelectric tensor components, which is given by [2]

$$\alpha_{ij}^2 \leq \epsilon_0 \mu_0 \epsilon_{ij} \mu_{ij} \tag{2.4}$$

This upper bound serves as a remark to the importance of the search multiferroic magnetoelectric materials. Since the ferroic materials have a tendency towards higher values of ϵ_{ij} and μ_{ij}, they are the ideal candidates for high magnitude magnetoelectric coefficients.

2.3 Mechanisms of Multiferroicity in Single Phase Materials

There have been several approaches to explain the arising of electric polarization from magnetic ordering. From the specific cases of transition metal oxides [50], perovskite structures [51] and manganites [52]. Many other works regard the role of non-collinear spin structures in the origin of polarization [53, 54] and, given its presence in the especially notable quadruple perovskite $CaMn_7O_{12}$ [34, 35], it is worthy delving into a phenomenological approach by Mostovoy[55]. This approach presents a more general phenomenological picture than the previous section, particularly by admitting spatially inhomogeneous magnetic structure. This is a Ginzburg-Landau theory approach that, in order to respect the time inversion properties of the magnetization and the space inversion properties of the polarization, couples them into a magnetoelectric free energy term that is linear in $\mathbf{P}$, quadratic in $\mathbf{M}$ and contains one gradient of the magnetization.

$$\Phi_{ME} = \gamma \mathbf{P} \cdot [\mathbf{M}(\nabla \cdot \mathbf{M}) - (\mathbf{M} \cdot \nabla)\mathbf{M} + \cdots] \tag{2.5}$$

Where γ is a proportionality coupling constant. Adding that to the electric free energy $\Phi_E = \frac{\mathbf{P}^2}{2\chi_E}$, with χ_E being the electric susceptibility. Minimizing the total free energy with respect to $\mathbf{P}$ provides

$$\mathbf{P} = \gamma\chi_E[\mathbf{M}(\nabla\cdot\mathbf{M}) - (\mathbf{M}\cdot\nabla)\mathbf{M}] \tag{2.6}$$

If the magnetization is given by a spin density wave with wavevector $\mathbf{Q}$,

$$\mathbf{M} = M_1\cos(\mathbf{Q}\cdot\mathbf{x})\mathbf{e}_1 + M_2\sin(\mathbf{Q}\cdot\mathbf{x})\mathbf{e}_2 + M_3\mathbf{e}_3 \tag{2.7}$$

A polarization will be produced, and its average over a unit cell $\bar{\mathbf{P}} = \frac{1}{V}\int \mathbf{P}d^3x$ will be

$$\bar{\mathbf{P}} = \gamma\chi_E M_1 M_2[\mathbf{e}_3\times\mathbf{Q}] \tag{2.8}$$

Which shows that the polarization produced by a helical or conical spin order is perpendicular to the propagation vector of said order.

Although useful to understand how an inhomogeneous magnetic order can produce a finite, macroscopic polarization, it doesn't explain the magnetic origins of the polarization via a microscopic model. A review paper by Tokura, Seki and Nagaosa[23] provides an overview of the main mechanisms by which magnetic order can give rise to electric polarization and, more importantly, to the mechanisms that have been shown to be more important in the study of quadruple perovskite manganites.

The first discussed model is called the *Symmetric Exchange Striction* model. The name of the model arises from the lattice distortion arising from spatial variations of the magnitude of the exchange interaction between neighboring spins. That is, when we have $J_{ij} = J_{ij}(r_{ij},\theta_{ij})$ in the exchange Hamiltonian $\mathcal{H} = \sum_i J_{ij}\mathbf{S_i}\cdot\mathbf{S_j}$. Therefore, if we write $r_{ij} = r_{ij}^{(0)} + \delta r_{ij}$ and $\theta_{ij} = \theta_{ij}^{(0)} + \delta\theta_{ij}$ and expand $J_{ij} = J_{ij}(r_{ij},\theta_{ij})$ around the equilibrium positions we have

$$J_{ij} = J_{ij}(r_{ij}^{(0)} + \delta r_{ij}, \theta_{ij}^{(0)} + \delta\theta_{ij}) = J_{ij} = J_{ij}(r_{ij}^{(0)},\theta_{ij}^{(0)}) + \delta r_{ij}\frac{\partial J_{ij}}{\partial r_{ij}} + \delta\theta_{ij}\frac{\partial J_{ij}}{\partial\theta_{ij}} + \cdots \tag{2.9}$$

Where the neglected terms are quadratic or of higher order. It is important to notice that if the derivatives in equation 2.9 are non-zero, the exchange striction contribution will appear in the energy expansion in lower order than the elastic energy, which is always quadratic, therefore making the exchange striction a relevant distortion mechanism despite the lower energy scale of the exchange interaction compared to the electronic energy scale that rule crystalline structure. This mechanism doesn't privilege any polarization direction in particular, and is dependent on the collinear component of the spin structure. That is, the polarization can be written in the form $\mathbf{P}_{ij} = \mathbf{\Pi}_{ij}(\mathbf{S}_i\cdot\mathbf{S}_j)$.

In one dimension and with an exchange constant J that changes sign, this mechanism can lead to parallel spin dimmers, as shown in figure 2.6. In higher dimensions, the

rich dependency with distance and angle of the exchange constant in $Mn-O-Mn$ can lead to this kind of distortion in manganites. Rare earth manganites RMn_2O_5 systems and simple perovskites like $HoMnO_3$ are examples of compounds in which this mechanism leads to multiferroicity [23, 29].

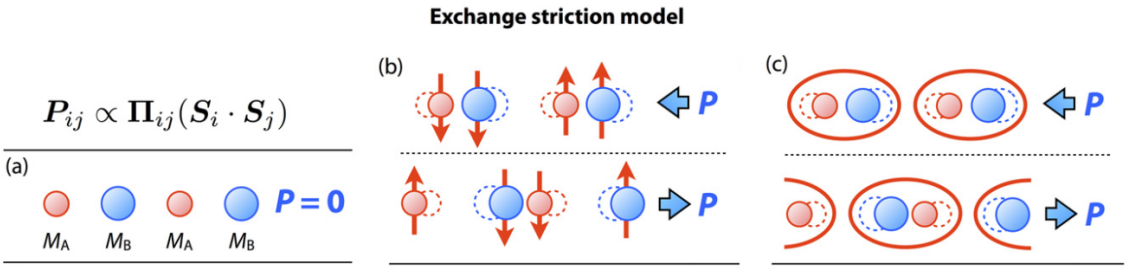

Figure 2.6 – Symmetric exchange striction mechanism to magnetic driven polarization. a) Magnetic and valence inequivalent ions in their equilibrium position. b) and c) Spin coupled dimmers in their distorted position, leading to polarization represented by blue arrows. Adapted from [23].

The second mechanism to multiferroicity that both depends and helps to stabilize non-collinear spin structures in transition metal oxides is the *Inverse Dzyaloshinsky-Moriya Interaction* or *Asymmetric Exchange Striction* mechanisms. It is based in the Dzyaloshinsky-Moriya interaction, a spin orbit coupling exchange interaction that favor perpendicular spins instead of the usual parallel-favoring exchange interaction. It takes place in a $M-X-M$ bond, where M is a metal and X is a ligand, like oxygen of fluorine. It has the form $\mathcal{H} = \mathbf{D}_{ij} \cdot \mathbf{S}_i \times \mathbf{S}_j$ where $\mathbf{D}_{ij} \propto \mathbf{r}_i \times \mathbf{r}_j$, $\mathbf{r}_i$ and $\mathbf{r}_j$ are the vectors that link the metal ions i and j to the ligand atom.

This mechanism favors non-collinear spins structures, like helical, conical or spiral orderings, as well as favor a displacement of the ligand atom in a direction perpendicular to the direction linking the metal ions, and therefore induces an electric dipole in that direction. Thus, as shown in figure 2.7, the polarization produced by this mechanism is $\mathbf{P}_{ij} \propto \mathbf{e}_{ij} \times \mathbf{S}_i \times \mathbf{S}_j$, where $\mathbf{e}_{ij}$ is the vector that links the two metal ions.

This model is also called *Spin Current* model. Being the product of the spin and momentum operator, the first being reversed under time inversion and the second by both time and spatial inversion, the spin current has the same symmetry property as the electric polarization or the electric field. Coupling spin current and electric field for a spatially invariant energy term produces the exact same result as the DMI mechanism [23], but since the DMI seems more related to the present case of manganites it is the preferred picture in this work. The inverse Dzyaloshinsky-Moriya mechanism is thought to be behind not only of the multiferroicity of several rare earth manganites of perovskite structure [23], but also of the quadruple perovskite $CaMn_7O_{12}$ and its very high polarization [34, 35].

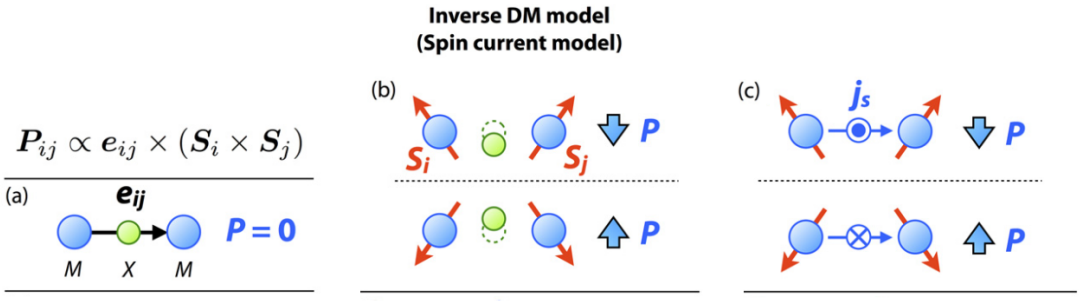

Figure 2.7 – Asymmetric exchange striction mechanism to magnetic driven polarization. a) Shows the non-polar configuration of metal ions M and ligand X. b) Shows ligand displacement that gives rise to the polarization represented by the blue arrow. c) Shows the spin currents involved, which produces polarization in the same direction as panel b. Adapted from [23].

Finally, the third mechanism discussed in [23] is the *spin dependent p-d hybridization* model. Based on the orbital hybridization of the d orbitals of metal ions and the p orbitals of the ligand. It was studied under perturbation theory with the hybridization parameter and spin orbit coupling constant as perturbation terms [56,57]. The origin of the polarization is the virtual charge transfer originated from the asymmetric form of the hybridized orbital. The study shows a non-zero component of the polarization that doesn't depend on the relative orientation of neighboring spin, but on the relative orientation of a single spin and the direction linking the metal and the ligand. So, naming that direction $\mathbf{e}$, we have a local component of the polarization $\mathbf{P} \propto (\mathbf{S} \cdot \mathbf{e})^2 \mathbf{e}$. Evidently, structures with mirror planes perpendicular to $\mathbf{e}$ will lead to a zero total polarization, but as shown in figure 2.8, some structures, like tetrahedral, will lead to a finite macroscopic polarization. One example of multiferroic material led by this mechanism are rare-earth Boron ferrites $RFe_3(BO_3)_4$ [23].

Apart from mechanisms of magnetically induced polarization, there is a very interesting coupling mechanism between electrical and magnetic propertied is described by Belashchenko[58]. The mechanism regards the domain boundaries of an magnetoelectric antiferromagnet. Since the normal direction to a domain boundary provides the same symmetry reduction associated with a uniform electric field, *i. e.* from even to odd regarding spatial inversion. This effect lifts the degeneracy between boundary states with reversed spins by removing the symmetry operation mapping them into each other. The net result is a finite thermodynamic average over the antiferromagnetic border. The microscopic mechanisms by which the magnetic moments in certain sites is reversed to accomplish an equilibrium non-zero magnetization are shown in figure 2.9. These mechanisms involve more drastic effects like direct spin flips for certain sites, but also subtler ones like distinct thermal averages over distinct sites according to their distance to the border, or the

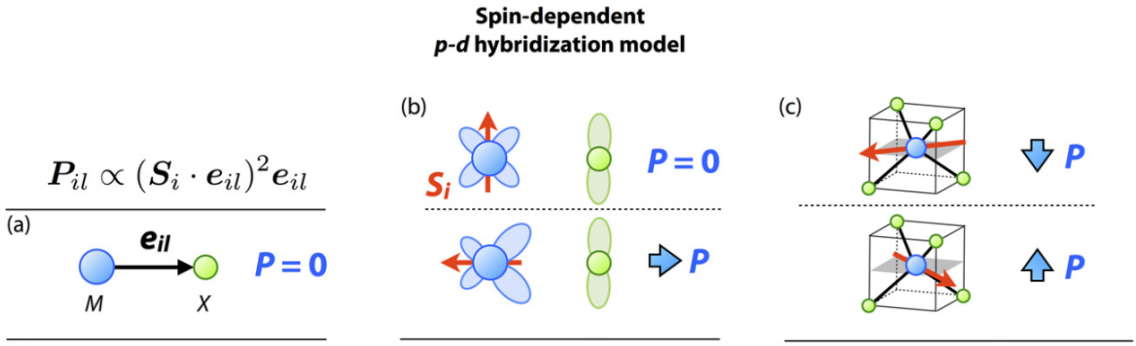

Figure 2.8 – Spin dependent p-d hybridization mechanism. a) Shows the $\mathbf{e}_{il}$ vector between the metal and ligand ions. b) Shows the polarization resulting from different orientations of the spin relative to the position of the ligand. c) Show that in tetrahedral structures a finite polarization is preserved. Adapted from [23].

different spin states in certain sites.

This effect is compatible with the main mechanisms for multiferroicity in the studied quadruple perovskites and should be present in all situations where $\alpha_{ij} \neq 0$. This opens a wide range of study possibilities in magnetoelectric antiferromagnets since a finite a switchable boundary magnetization is much better suited for applications than the hard to flip bulk antiferromagnetic magnetization.

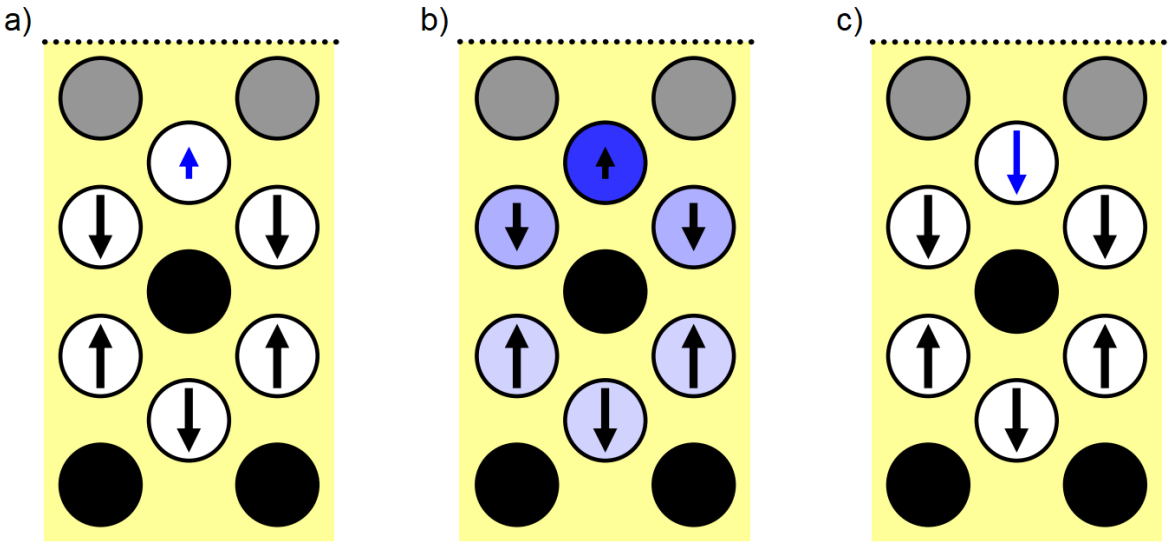

Figure 2.9 – Mechanisms to accomplish finite border magnetization. a) Site selective different spin state (blue arrow). b) Different thermal averages indicated by blue shading and arrow size represented thermal disorder and moment average. c) Spin flip indicated by blue arrow. Adapted from [58].

3 Materials and Methods

3.1 Synthesis and Samples

The quadruple perovskite family of compounds usually presents greater density and more symmetrical structures when compared with the available simple perovskites [59]. That may explain the higher stability of the simple perovskite phase, and the usual necessity of high pressures and temperatures to synthesize the quadruple perovskite structure. Although some compounds in the quadruple perovskite family can be synthesized by other means, like the $ACu_3Mn_4O_{12}$ class that can be fabricated via hydro-thermal route [59], the synthesis of $NaMn_7O_{12}$ and $LaMn_7O_{12}$ so far has only been achieved by solid state reaction under high pressures and temperatures [32, 59]. The samples used in this work have been produces by Edmondo Gilioli's group in the Institute of materials for electronics and magnetism (IMEM) in Parma, Italy.

The used method for achieving the pressures in the order of tens of GPa is described in [60] and details of this kind of press are found in figure 3.1. The primary element of pressure applying are the pressure plates (G_{1-2}), which are acted on by a uniaxial press. Six wedges (A_{1-6}) are circularly disposed on top and bottom of the tungsten-carbide corner-truncated cubic anvils (C). Those, in turn, distribute pressure onto the pressure medium (D), an octahedral MgO cell where the platinum foil capsules containing the reagents and a Pt/Pt-Rh10% thermocouple are placed for temperature measurements. This kind of configuration allows the uniaxial pressure of the press to be distributed in a quasi-hydrostatic fashion, and allows pressures up to tens of GPa.

The optimal conditions for synthesis regarding purity and large crystal sizes for $NaMn_7O_{12}$ has been studied and is summarized in [33] and a phase diagram can be seen in figure 3.2. The best condition for large crystals was determined to be 3 GPa and 550 °C. The capsule is prepared with a mixture of Mn oxides (MnO_2 and Mn_2O_3) and $NaOH$ pellets in proportion 5-10 % mol-richer in Na than $NaMn_7O_{12}$ stoichiometry. Alternatively, pre-reacted $NaMn_5O_{10}$ is also used.

In the P-T phase diagram (see figure 3.2), the largest crystal sizes were obtained barely outside the stability field of the quadruple perovskite phase and had to be manually picked apart from the reagents in the capsule. Going into the stability field reduces the amount of secondary phase to under 5% but decreases crystal sizes, being favorable only for the production of polycrystalline pellets. Under very specific conditions, shorter reaction times led to small, but very regular crystals, heating rates had mostly no effect over the synthesis and humidity is shown to favor the reaction but not the crystalline quality

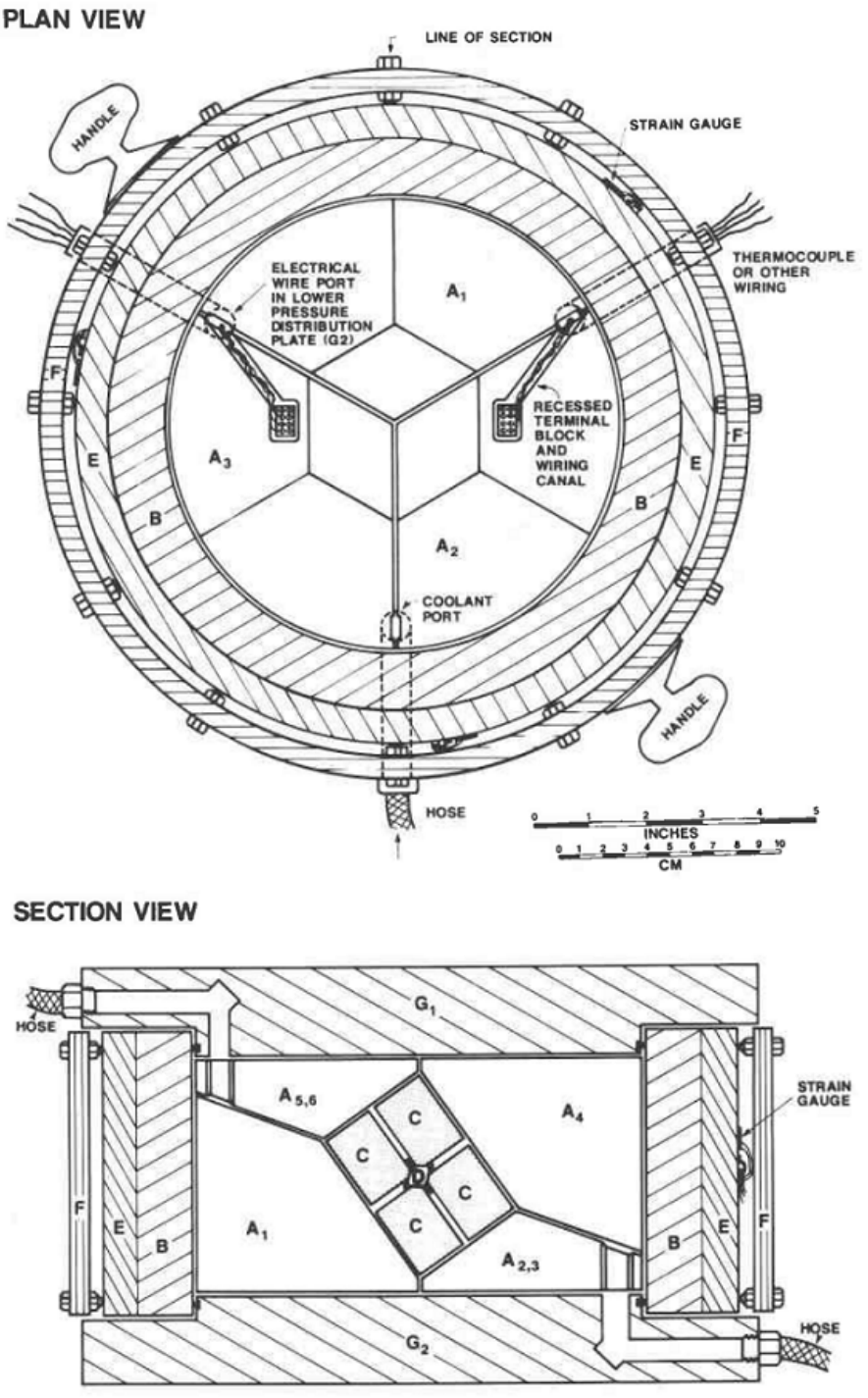

Figure 3.1 – Plan and section views of multi-anvil press module and main components. (A) Tool steel wedges. (B) Tool steel cylindrical containment ring, main body of the modulus. (C) Tungsten-carbide corner-truncated cubic anvils. (D) MgO sample cavity and pressure medium. (E) Steel safety ring jacketing main body. (F) Polycarbonate scatter shield. (G) Tool steel pressure plates. Adapted from [60].

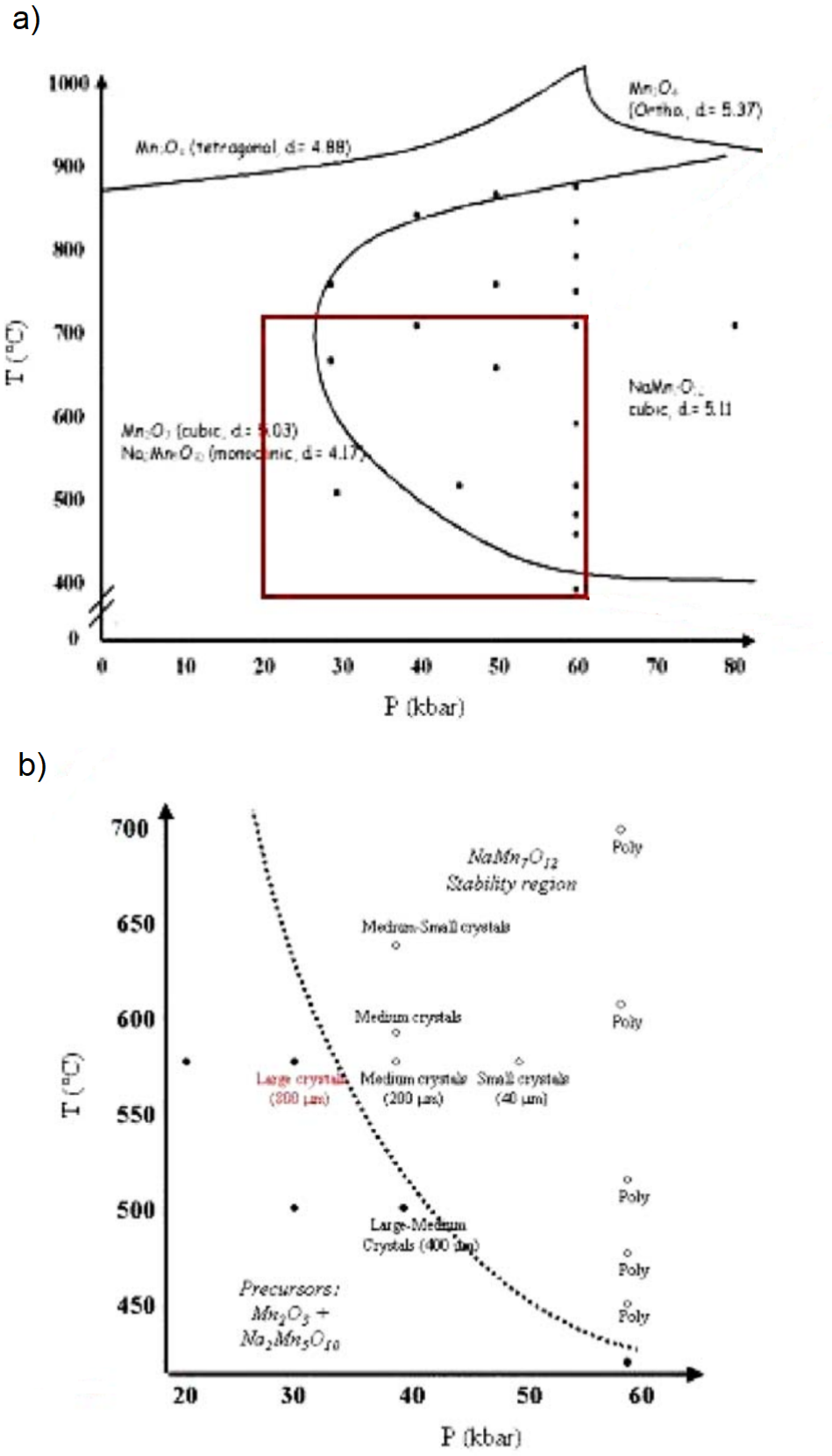

Figure 3.2 – a) Phase diagram for the formation of $NaMn_7O_{12}$. b) zoom into the investigated region for formation of large crystals [33].

and size. 5% molar excess of Na compared to the stoichiometric ratio was found to be optimal both for crystal sizes and purity ratios, a lesser excess led to the presence of unreacted precursors and excess over 5% was found to lead to secondary phase formation. In parallel experiments, previously reacted $NaMn_5O_{10}$ presented better performance [33]. The best obtained samples include several hundred-micron crystals and over 95% purity polycrystalline pellets.

For $LaMn_7O_{12}$, very little improvement was achieved regarding crystal sizes and reaction completion when compared to the first synthesis [31,59]. In contrast with $NaMn_7O_{12}$, $LaMn_7O_{12}$ crystals reach larger sizes under longer reaction times. The stoichiometric 7:1 mixture of Mn_2O_3 and La_2O_3 are submitted to 4 GPa and 1000 °C for 1-2 hour for polycrystalline pellets and 10 hours for larger crystals, reaching 300 μm. The polycrystalline samples purity is as high as 95%, the main secondary phases are unreacted precursors and the simple perovskite phase $LaMnO_3$ [31, 59].

3.2 Magnetization Measurements

All magnetization measurements were performed in a Quantum Design MPMS3 SQUID-VSM, the setup of which can be seen in figure 3.3. Currently, the most precise method for measuring magnetic moments is using a *superconducting quantum interference device* (SQUID). It makes use of a balanced Josephson junction to measure quanta of magnetic flux, which can be calibrated to measure magnetic moments. The MPMS3 makes use of SQUID-equipped detection coils to build a gradiometer to achieve 10^{-8} emu precision in measuring magnetic moments in two main modes.

In VSM (vibrating sample magnetometry) technique, the sample is vibrated in the center of the gradiometer with known amplitude and frequency. The total magnetic moment in the center of the gradiometer will be proportional to the amplitude of the electric signal with the same frequency that will be induced in the gradiometer coils. This is the preferred method of magnetization measurements and the one that achieves higher accuracy, when combined with SQUID detection.

In certain occasions, it's more advisable to utilize a measuring method that causes less acceleration in the sample holder (e. g. when using the homemade sample holder, which is very delicate). For this and other occasions the MPMS3 also offers the possibility of measurements in extraction mode, also called DC mode. In this mode, the sample is pulled through the ensemble of the gradiometer coils with known velocity. The sample transit induces a waveform in the gradiometer coils, which can be fitted to obtain the magnetic moment.

To achieve the high magnetic fields many times necessary in magnetic characterization, the MPMS 3 is equipped with a niobium-titanium (NbTi) superconducting coil

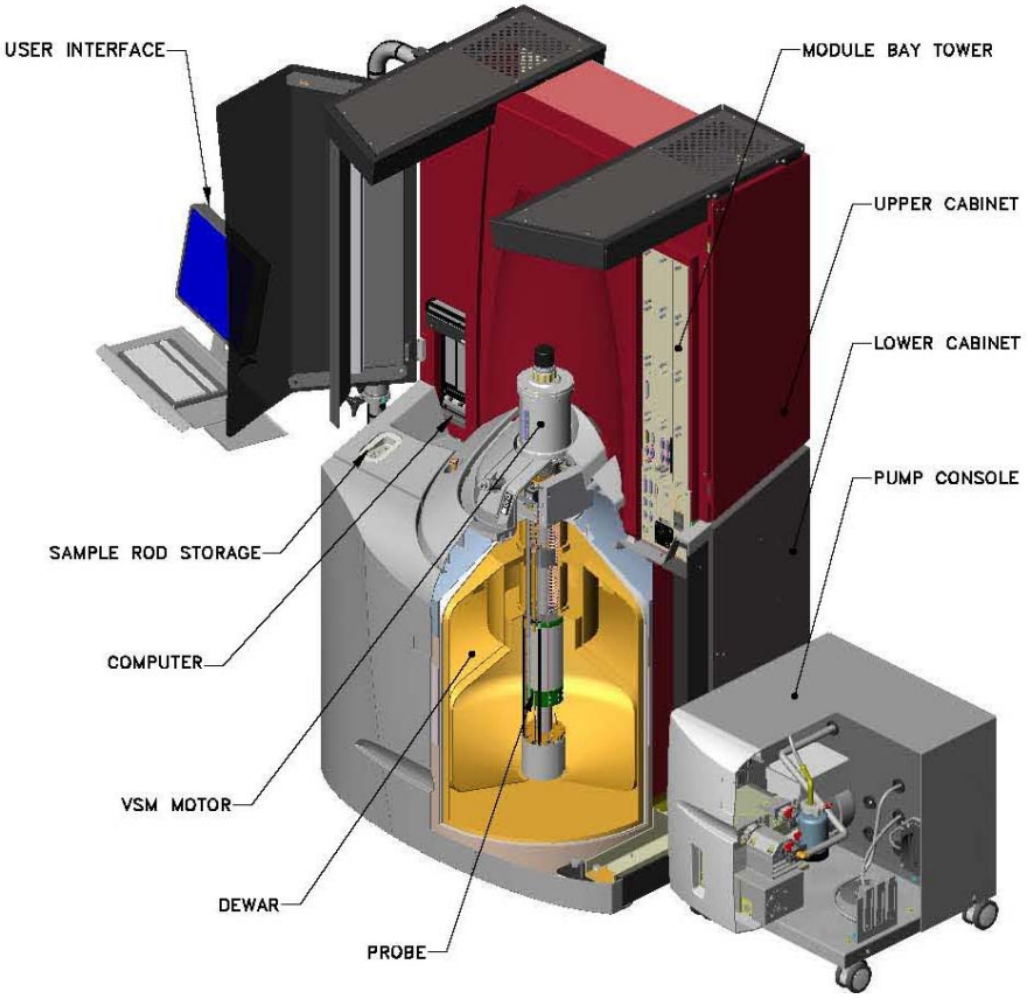

Figure 3.3 – Quantum Design MPMS3 SQUID-VSM general setup. Adapted from [61]

mounted around the sample chamber. It is capable of delivering magnetic fields up to 70 kOe in persistent mode, which can be charged at a rate up to 700 Oe/s. The field magnitude is measured via the current in the superconducting coils and the whole ensemble can be quenched (e. g. heated above the superconducting phase) to eliminate the common problem of trapped magnetic flux in the superconducting coils. The magnetic field is calibrated using a NIST certified palladium sample, which is readily available to perform corrections for residual magnetic fields in the low-field region.

A liquid Helium cryostat is used both to keep the magnet coil and the squid sensors at superconducting temperatures and to provide temperature control capabilities to the sample chamber. By pumping Helium gas at a controlled flow into the outside of the low-pressure sample chamber, the MPMS 3 is capable of achieving sample temperatures varying from 1.8 K to 400 K with temperature rates that can reach 50 K/min. A set of thermocouples is used to precisely determine the temperature in the sample chamber. To reach temperatures in the range from 300 K to 1000 K, an oven accessory and special

sample holder is also available.

Another important technique in magnetic characterization is the AC magnetic susceptibility (also called AC magnetization). Instead of providing magnetic excitation by vibrating or pulling the sample through the gradiometer, the excitation is provided by applying an alternating magnetic field. The resulting variation in magnetization has an in-phase (χ') and an out-of-phase (χ'') components. The in-phase component, χ', is related to the derivative of the magnetization with respect to the magnetic field. On the other hand, the out-of-phase component, χ'', is related to eddy currents, phase transitions and other dissipation processes. Besides the possibility of performing AC susceptibility, the capability of providing alternating fields and providing its drive signal to external instruments is very important to the possibility of performing Magnetoelectric Susceptibility measurements on the MPMS 3, which will be discussed in details in the next section.

To perform electric measurements using the MPMS 3 temperature and magnetic field facilities, a homemade sample holder was adapted by Alexandre Gualdi, combining a regular quartz sample holder with an oven accessory sample holder. This allows the usage of the oven accessory electric connections to obtain electric access to the sample chamber, which was of paramount importance in the setup of the experiments involving magnetoelectric susceptibility, thermally stimulated current and magnetization under electric fields. A photo of the homemade sample holder is available in figure 3.4.

Figure 3.4 – Homemade sample holder adapted for electric measurements.

3.3 Magnetoelectric Susceptibility

The Lock-In technique for measurements of magnetoelectric susceptibility has been described in [62]. There's great similarity between the AC magnetic susceptibility and its

electric counterpart. Both use and alternating magnetic field to excite a sample response in the same frequency. Instead of measuring the gradiometer signal, like in the AC magnetic susceptibility, the measured quantity is the induced voltage through the sample, which is associated to the change in polarization that a magnetoelectric sample undergoes when exposed to an alternating field.

To measure said voltage, leads in the sample surface are connected to an EG&G Lock-In Amplifier Model 7260 via the homemade sample holder for electric measurements. The Lock-In is locked to the frequency of the MPMS 3 AC field drive signal, as shown in figure 3.5. Both AC and DC are applied by the MPMS 3 and a custom PC is used to synchronize it to the external instruments via a LAN connection. .

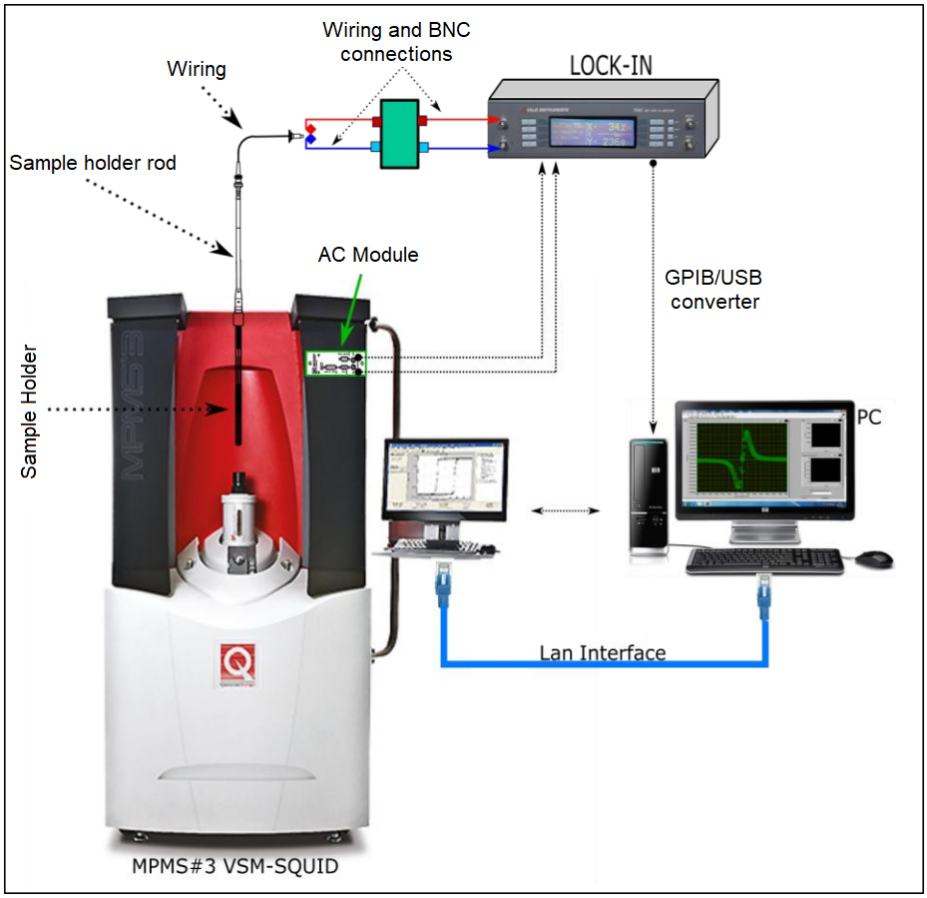

Figure 3.5 – Setup for magnetoelectric susceptibility measurements. Adapted from [63].

If the sample exhibits magnetoelectric effect, a magnetic field dependent voltage should arise, which can be expanded in

$$V_{out}(H) = V_0 + \alpha H + \beta H^2 + \cdots \tag{3.1}$$

Given the thickness d of the sample, and the constant and alternating components of

the magnetic fields $H = H_0 + h\cos\omega t$, it can be shown [62] that the linear magnetoelectric coefficient α equals, up to first order

$$\alpha = \frac{\partial E}{\partial H} = \frac{V_0}{dh} \tag{3.2}$$

Using this setup, the linear magnetoelectric coupling coefficient α can be measured directly, as well as its dependence with magnetic field, temperature and frequency. This can, in time compared to other indirect evidence of the existence or absence of magnetoelectric coupling in the samples.

3.4 Pyroelectric Current

One of the most common and effective methods of detecting ferroelectric polarization in a given material is through the method of the thermally stimulated currents, also called pyroelectric current method. The basis of of this method is the measurement of the depolarization current that goes through the sample when it undergoes a phase transition between a ferroelectric and a disordered phases. That current is due to the movement of the separated charges that cause polarization back into their equilibrium, non-polarized positions. It is also noteworthy that in the polarized state there is charge accumulation in the surface of the sample and from the classical electrodynamics equation $\mathbf{P}\cdot\hat{\mathbf{n}} = \sigma_P$ [64] it can be seem that the depolarization current from a polarization $\mathbf{P}$ is equivalent to the current caused by the surface polarization charge density σ_P moving back to a electrostatic equilibrium position.

Let then be a pooled sample that is crossed by a current I when heated at a constant rate R, the change in polarization ΔP between two instants t_1 and t_2 is given by

$$\Delta P = \frac{\Delta Q}{A} = \frac{1}{A}\int_{t_1}^{t_2} I dt = \frac{1}{A}\int_{t_1}^{t_2} I\frac{\partial t}{\partial T}dT = \frac{1}{A}\frac{1}{\frac{\partial T}{\partial t}}\int_{t_1}^{t_2} I dT = \frac{1}{AR}\int_{t_1}^{t_2} I dT \tag{3.3}$$

Where ΔQ is the total displaced charge, A is the surface area of the sample and T_1 and T_2 are the corresponding temperatures to the instants t_1 and t_2.

Using the homemade sample holder for electric measurements, thermally stimulated current measurements were made available in the MPMS 3 cryostat in the temperature range of 15 - 300 K ad fields up to 70 kOe. A Keithley Model 617 electrometer was used to measure the currents in the picoampere scale and a Keithley Sourcemeter 2635 was used as voltage source for polarization procedures under up to 100 V.

3.5 Specific Heat

The most important principle for the measuring of specific heat and heat capacity at constant pressure is a precise control of heating power, temperature measurement and heat losses. The Physical Properties Measurement System (PPMS), also produced by Quantum Design, makes available a heat capacity measurement option. The heat capacity

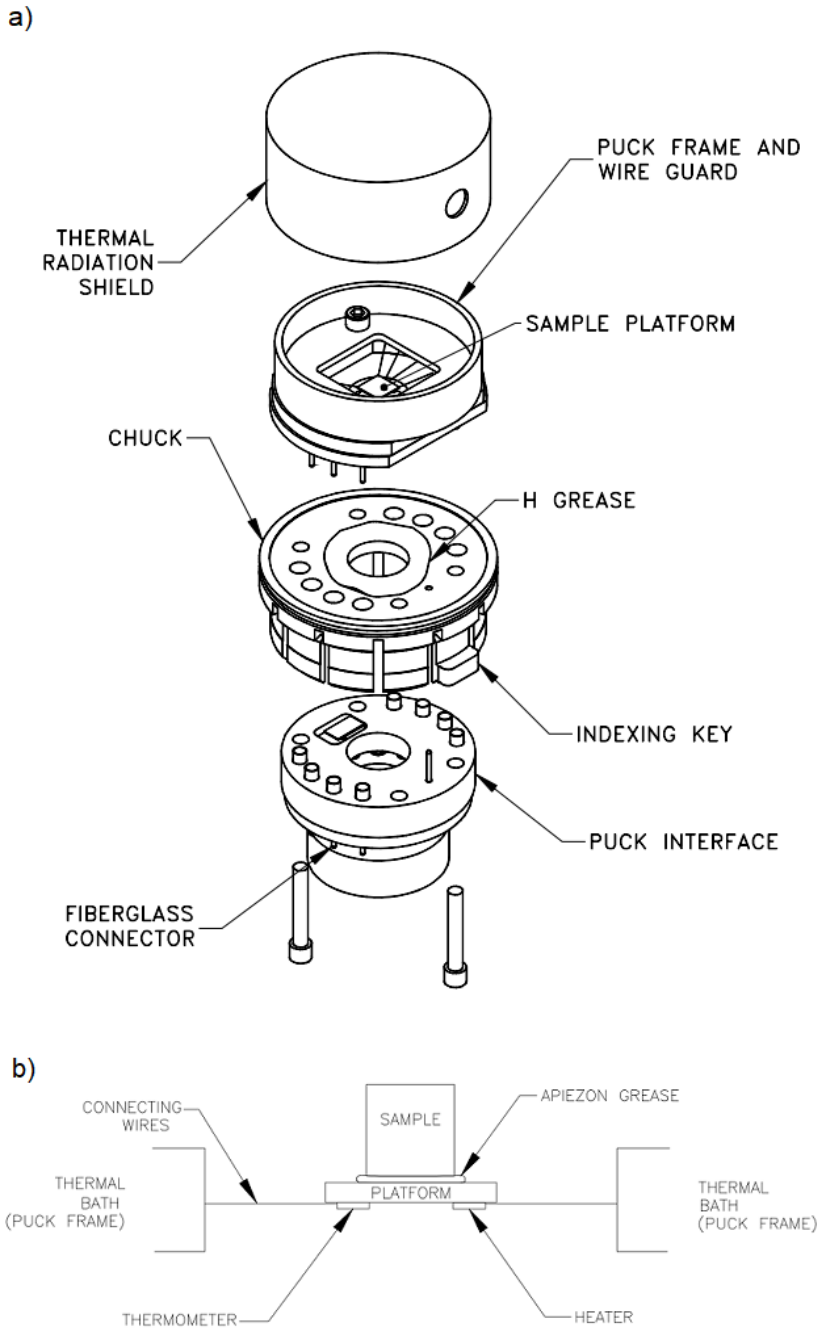

Figure 3.6 – a) Exploded view of the sample puck used for the specific heat measurements setup. b) Detailed schematic of the experimental region of the specific heat measurement. Both adapted from [65]

measurements are performed by fixing the sample in a monocrystalline sapphire base using Apiezon cryogenic vacuum grease. The whole ensemble is heated using RuO_2 electrical heater deposited into the underside of the base. A thermometer is attached to the sapphire base for accurate acquisition of temperature data. The sapphire base is suspended from platinum wires in order to thermally separate it from the rest of the puck, the wires also provide electrical and thermal connections to the sample space. A sketch of the puck and sample spaces can be seen in figure 3.6.

By applying current to the heater at constant power during a known time interval, the quantity of heat transferred to the sample-platform ensemble can be precisely determined. The temperature at the bottom of the base is measured during the heating and cooling processes and can be compared to the thermal bath in which the rest of the puck and the sample chamber (which are kept at constant temperature) are immersed. A high-vacuum pump keeps the chamber pressure under 1 mTorr, making the heat losses to the atmosphere negligible. The radiation shielding in the puck shown in figure 3.6 a) avoids losses via radiation and the very reproducible thermal behavior of the platinum wires guarantees that the conduction losses can be accounted for.

The temperature data in each heating-cooling cycle is then fitted into a model that considers losses to the wires and the thermal relaxation between the platform-sample set and the exterior thermal bath, as well as the internal sample-platform relaxation. This assures that precise heat capacity measurements can be obtained even when the grease mediated thermal contact between the sample and the platform is poor [65]. Finally, a previous calibration using only the platform and the grease is used in the model to subtract their contribution, resulting in the heat capacity belonging only to the sample.

3.6 Raman Spectroscopy

The Raman spectroscopy is named after Sir C.V. Raman, who showed in partnership with K. S. Krishnan that light can be inelastically scattered by a fluid. For the discovery, Raman was given the Nobel prize in 1930 and, despite the difficult conditions in which the experiment was performed, new developments in optics and laser technology made inelastic scattering of light into a powerful technique for the investigation of vibrational properties of molecules and crystalline solids alike [66].

The principles of the inelastic scattering of light can be understood in classical approach. Under an electric field $\mathbf{E}$, a molecule or crystalline solid will develop an electric dipole $\mathbf{p}$. The two quantities can be related via the polarizability tensor $\boldsymbol{\alpha}$, where $\mathbf{p} = \boldsymbol{\alpha} \cdot \mathbf{E}$. The polarizability tensor is determined by the structure of the molecule or crystal. Therefore, to account for changes in polarizability due to the deformation caused by the electric field a first order approximation can be used:

$$\boldsymbol{\alpha} = \boldsymbol{\alpha_0} + \sum_k \left(\frac{\partial \boldsymbol{\alpha}}{\partial Q_k}\right)_0 \cdot Q_k + \cdots \tag{3.4}$$

where Q_k are the positional coordinates of the atoms in the k^{th} normal mode of vibration, calculated in the harmonic approximation and the index zero in the partial derivative indicates that these harmonic oscillations are calculated with respect to a system undisturbed by the electric field. Let then the electric field $\mathbf{E} = \mathbf{E_0}\cos(\omega_0 t)$ be the electric part of a light wave. From the harmonic approach, the movement of the atomic coordinates will be $Q_k = Q_{0k}\cos(\omega_k t + \phi_k)$, where ω_k is the frequency of the k^{th} normal mode and ϕ_k the associated phase delay. Then we can write the contribution of each frequency ω_k to the electric dipole as

$$\mathbf{p}_{\omega_\mathbf{k}} = \boldsymbol{\alpha_0} \cdot \mathbf{E_0}\cos(\omega_0 t) + \boldsymbol{\alpha}' \cdot \mathbf{E_0} Q_{0k}\cos(\omega_0 t)\cos(\omega_k t + \phi_k) \tag{3.5}$$

Where $\boldsymbol{\alpha}' = \left(\frac{\partial \boldsymbol{\alpha}}{\partial Q_k}\right)_0$. Using a trigonometric identity, it can be shown that equation 3.5 is equivalent to

$$\mathbf{p}_{\omega_\mathbf{k}} = \boldsymbol{\alpha_0}\cdot\mathbf{E_0}\cos(\omega_0 t) + \frac{1}{2}\boldsymbol{\alpha}'\cdot\mathbf{E_0}Q_{0k}\cos[(\omega_0+\omega_k)t+\phi_k] + \frac{1}{2}\boldsymbol{\alpha_k}'\cdot\mathbf{E_0}Q_{0k}\cos[(\omega_0-\omega_k)t-\phi_k] \tag{3.6}$$

or, alternatively, for each vibrational frequency ω_k of the crystal (or molecule), we have

$$\mathbf{p}_{\omega_\mathbf{k}} = \mathbf{p}(\omega_0) + \mathbf{p}(\omega_0+\omega_k) + \mathbf{p}(\omega_0-\omega_k) \tag{3.7}$$

From equation 3.7 it can be seen that the induced dipoles for each excitable frequency in the sample will have three radiating components. The first is the elastic scattering process, which is in the same frequency as the incident light, and is usually filtered out in experiments since its intensity overcomes all the other processes. The second term is called the Anti-Stokes process, and it radiate with energy higher than the incident. The last process is called the Stokes process and it has lower energy than the incident one. The Raman spectra are usually expressed in wavenumber difference (cm^{-1}) from the incident light, in such way that Stokes processes appear as positive wavenumbers. A typical Raman specter can be seen in figure 3.7, showing the Stokes, Anti-Stokes and elastic scattering peaks.

For an energy mode to be detectable via Raman, spectroscopy, however, it is necessary for it to have a non-vanishing derivative of the polarizability tensor, that is, $\boldsymbol{\alpha}'_\boldsymbol{k} = \left(\frac{\partial \boldsymbol{\alpha}}{\partial Q_k}\right)$. This condition relates to the possibility of the electric field of the radiating light changing the induced electric moments related to the referred normal mode. This is

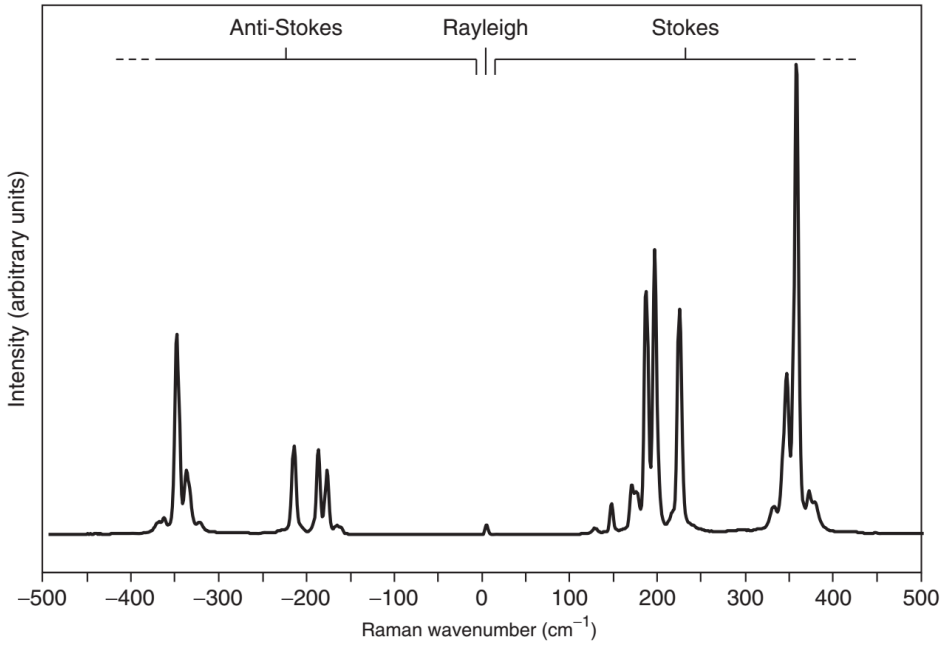

Figure 3.7 – Raman specter for As_4S_4 showing Stokes, Anti-Stokes and elastic scattering peaks. Elastic intensity attenuated by a filter [66].

in contrast with the conditions for infrared spectroscopy, which relates to the *permanent* electric dipoles and how they are affected by the incoming electric field. Both in infrared and Raman spectroscopy, Group Theory analysis and symmetry properties can be used to determine which modes are active in each technique.

Raman spectroscopy experiments were performed using T64000 Jobin Yvon spectrometer in the 200 – 700 cm^{-1} energy range (incident light at 514 and 454 nm) and at temperatures from 15 to 250 K. Low temperature specters (2 K) were also taken under magnetic fields up to 9 T using a superconducting magnet attached cooled by the same Helium cryostat.

3.7 Inelastic X-Ray Scattering

Although the first experiments regarding the inelastic scattering of x-rays dates to the experimental verification of the Compton Effect it has become an important technique in the characterization of fundamental excitation in crystalline solids, especially since the advent of intense synchrotron light sources in the mid 1980 [67]. The basics of the scattering kinematics is shown in figure 3.8. The incoming photons from the light, carrying a fixed energy $\hbar\omega_1$ and wavevector $\mathbf{K_1}$ are scattered by the sample and the scattered phonons are measured by the detector array at an angle θ with the incident direction.

From the measured scattered energy and wavevector, ω_2 and $\mathbf{K_2}$ respectively, and

the conservation of energy and momentum, it is easy to determine the energy $\omega = \omega_1 - \omega_2$ and momentum $\mathbf{q} = \mathbf{K_1} - \mathbf{K_2}$ which are transferred during the scattering process. There are several different scattering processes that can occur in IXS measurements. Important examples range from phonons (which can be seen in figure 3.8) to short range correlations and polarons which are reported with energies very close to the quasielastic peak [68]. Electron hole excitations, plasmons and core level excitations, which are very important in the resonant version of the technique (RIXS) are also detectable in the energy ranges shown in figure 3.9.

Compared to Raman spectroscopy, which is a light scattering technique of much easier access, the main advantage of IXS is the greater access to the reciprocal space of samples. Because of the relation between momentum and energy of photons ($\omega = c\,|\mathbf{q}|$) it is easy to see how the much higher energy of synchrotron sources provide a much wider cover of reciprocal spaces, compared to which the visible light used in most Raman spectrometers rests very close to the vectors $\mathbf{q} = 0$. Another important technique used to probe phonon dispersion curves is the inelastic scattering of neutrons (INS). When comparing the two inelastic scattering experiments, the greatest highlight of with X-rays is the possibility of performing experiments in much smaller samples (hundreds or even tens microns in diameter usually suffice) than required to neutron scattering (which usually require crystals of at least millimeter size) [69]. Besides, the higher energies of individuals x-ray photons compared to neutrons grants an energy resolution independent from energy transfer and there's nearly no background in IXS besides the quasielastic peak lorentzian tail and multi phonon scatterings. On the other hand, neutron scattering provides higher resolution at low energies and simultaneous cover of a large area of reciprocal space in each acquisition, making it the usually preferred when larger samples are available [69].

The general setup for an IXS experiment can be seen in figure 3.10. The first step

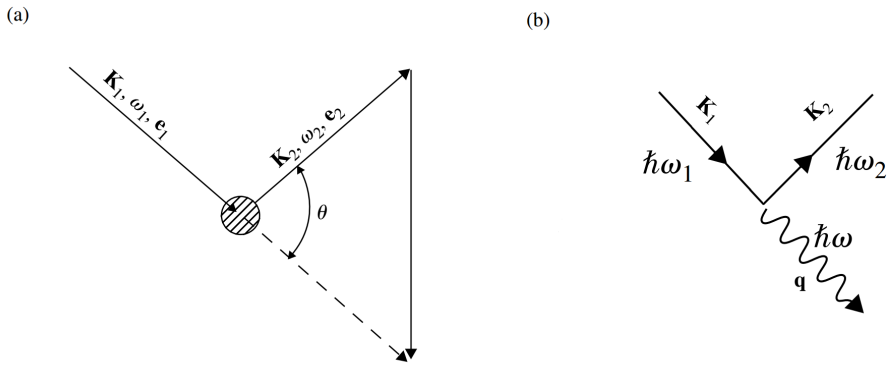

Figure 3.8 – (a) Sketch of IXS experiment. (b) Example of a one phonon scattering process. Adapted from [67].

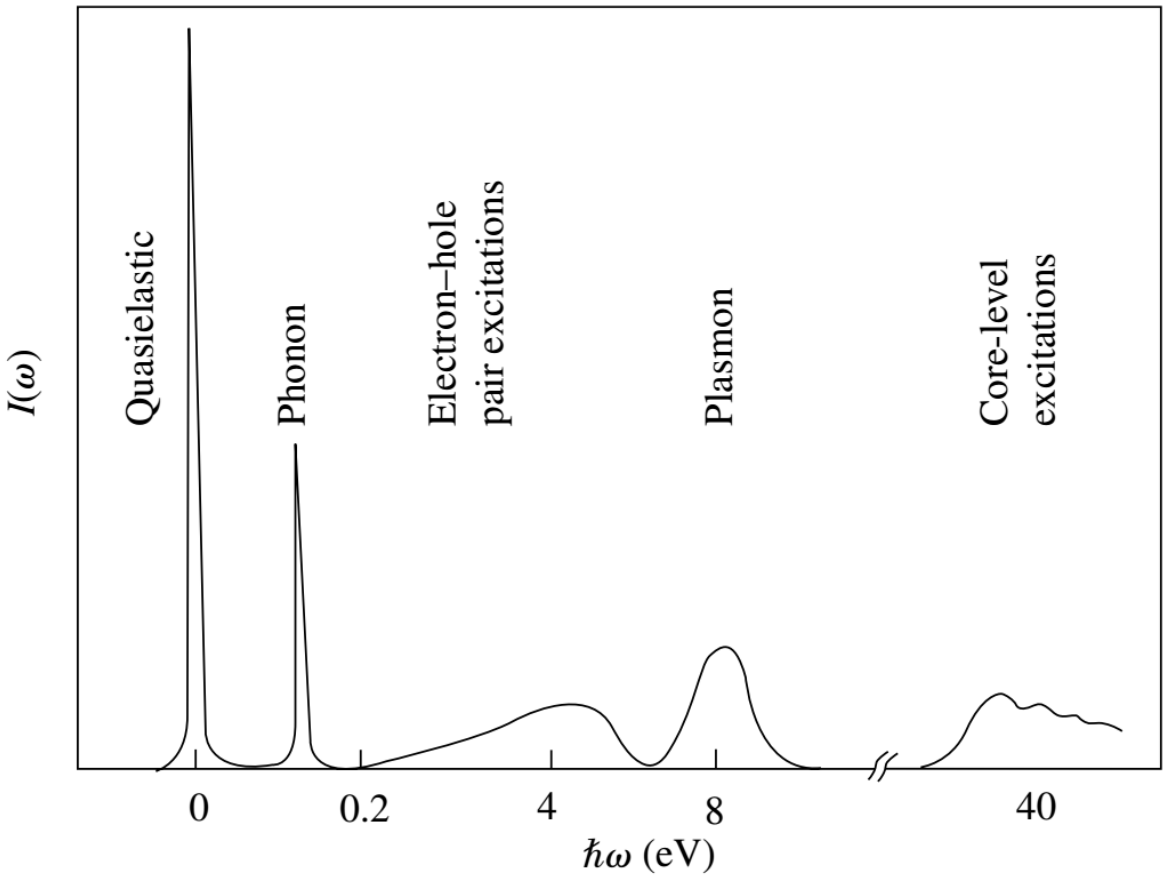

Figure 3.9 – Approximate energy range for different excitations measurable via IXS. Adapted from [67].

is to pass the synchrotron source beam through a monochromator, which is usually made of silicium. The monochromator separates different frequencies using the diffraction of the beam when passing through a massive silicium single crystal, the monochromator also works as a polarizer for the beam. Usually the (lll) reflection are used, as l increases, energy resolution increases, but at the cost of photon fluency. Many times, a two-stage monochromator is used, the first with a lower order reflection, like (111), and the other, final monochromator with a higher order reflection ($l = 7 - 13$).

The optional components shown in dashed lines in figure 3.10 are a polarimeter, to achieve circular polarization configurations, focusing optical elements to increase collimation and a monitor of photon flux. The energy analyzer and photon detector array must be mounted in an angle θ with the incident beam, and must be equipped with a window allowing only a small solid angle of the scattered light to reach the sensors.

The inelastic X-ray scattering in this work were performed in the ID28 beamline of the European Synchrotron Radiation Facility (ESRF) in Grenoble, France. The acquisitions were performed with an 0.6968 Å wavelength and the (999) silicium monochromator, which

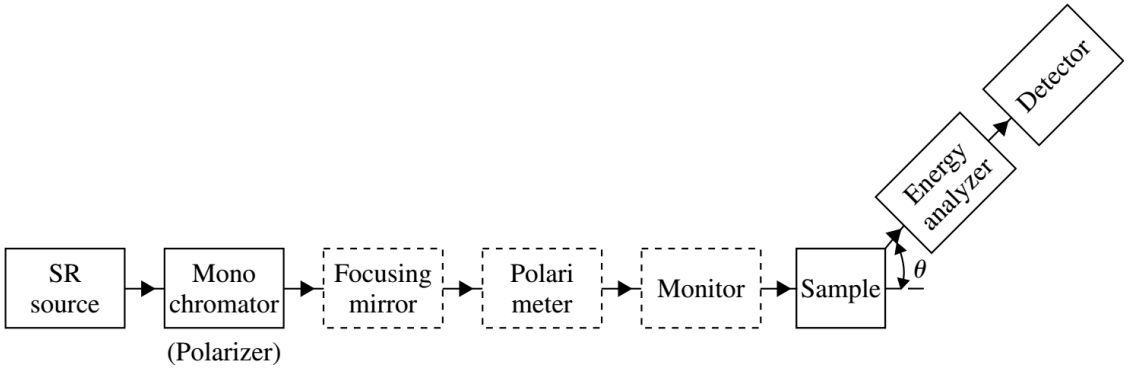

Figure 3.10 – Schematics of the main components of an IXS experiment. Adapted from [67].

provides a resolution of 2.4 meV.

3.8 Diffuse X-Ray Scattering

Usual techniques of x-ray diffraction are characterized by portraying the average position of atoms in lattices. In most scenarios that is an extremely precise framework, since the thermally induced movement of ions is small and centered in the said mean positions. Nevertheless, several important phenomena involve important deviations of ions (or groups of ions) from their mean position in the lattice. Motion of crystallized proteins, correlated disorder, polarons or incipient order preceding a structural phase transition or

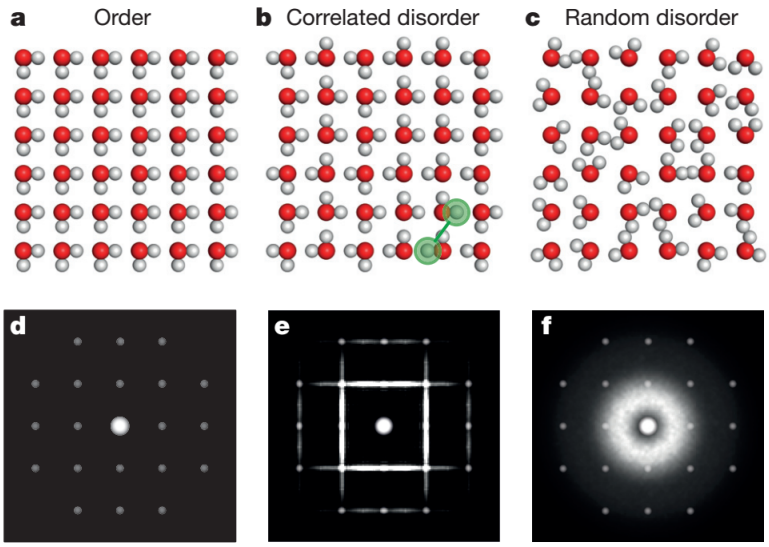

Figure 3.11 – Examples of diffraction patterns for water ice (a/d) in an ordered lattice, (b/e) in a hydrogen bonding respecting correlated disorder, (c/f) in random disorder. Adapted from [70].

distortion are a few examples of phenomena that can be better understood by looking into diffraction patterns that deviate from the perfect crystalline Bragg peak framework [40, 70–72].

Because they deviate from the ideal conditions for x-ray diffraction, this kind of feature is of very low intensity, two to four orders of magnitude lower than regular Bragg peaks, and their first records were obtained under very long exposition times, still in photographic films. They usually assume the form of diffuse features between peaks, as seen in figure 3.11, and sometimes form broad, low intensity peak-like shapes, depending on the phenomenon originating the diffuse scattering. Using modern sensors and high intensity synchrotron sources, diffuse x-ray scattering images can be acquired quickly and with very high cover and resolution. The diffuse scattering data in this work was acquired in the ID29 beamline at the ESRF, under wavelengths of 0.715 Å using the PILATUS 2M detector [73].

4 $(LaMn_3)Mn_4O_{12}$

4.1 Introduction

Among potentially complex quadruple perovskite and simple perovskite manganites ($A'Mn_3Mn_4O_{12}$ and $AMnO_3$ respectively), $LaMn_7O_{12}$ offers a simple picture. The trivalent Lanthanum ions assure that the only valence state in manganese is Mn^{3+}. With charge out of the picture, the only competing orders in $LaMn_7O_{12}$ are orbital and magnetic ones. Its structure belongs to the $I2/m$ space group in the whole temperature range studied in this work. It only goes through the cubic to monoclinic ($Im\bar{3}$ to $I2/m$) structural

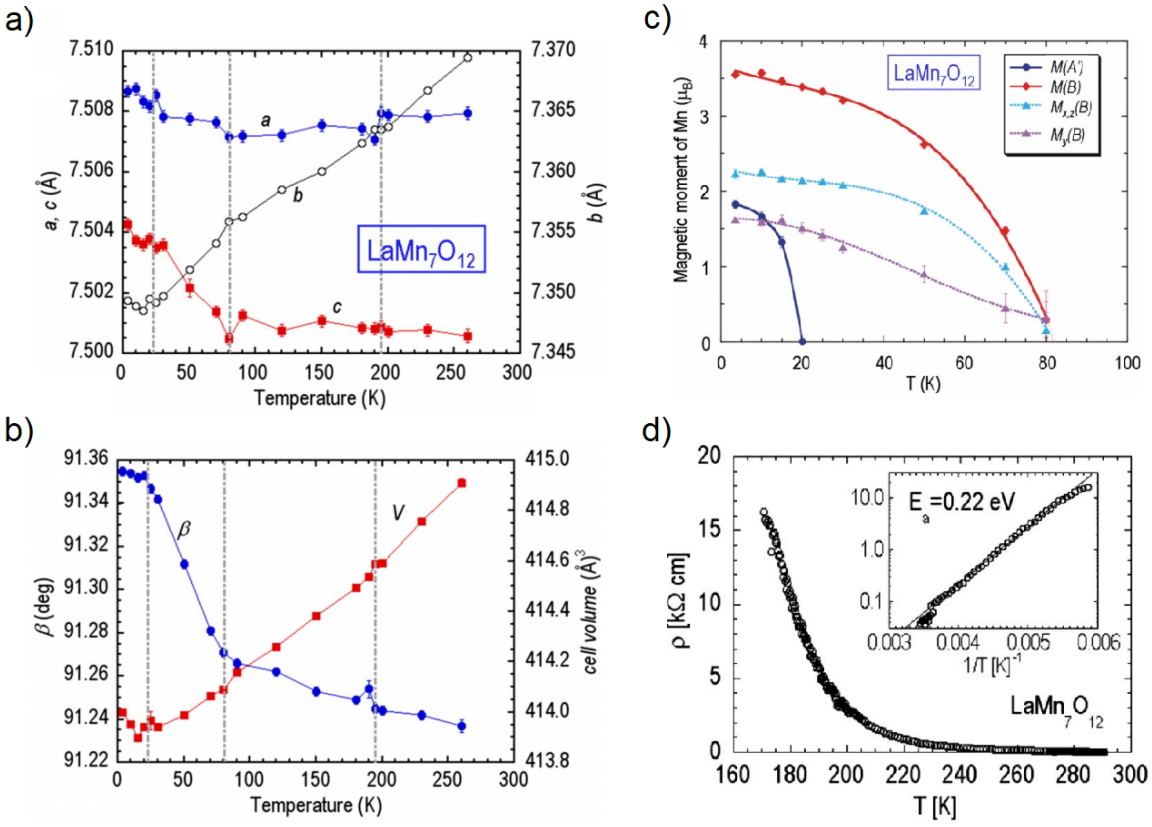

Figure 4.1 – a) and b) Lattice parameters and unit-cell volume of $LaMn_7O_{12}$ as a function of temperature. Dashed lines indicate magnetic transitions at $T_{N,A'} = 21$ K and $T_{N,B} = 78$ K, dashed line at 200 K indicates an anomaly related to trace amounts of impurities. c) Components of sublattice magnetization for the A' and B sites, obtained from neutron diffraction data. d) Evolution of dc electrical resistivity of $LaMn_7O_{12}$ with temperature. Inset: Arrhenius plot showing the thermally activated behavior of the charge carriers. The solid line is a linear fit. Adapted from [59].

transition at $T_C = 653$ K [74]. Compared to its simple perovskite counterpart $LaMnO_3$, $LaMn_7O_{12}$'s higher density and more compact structure is achieved through a very large, but rigid buckling of the MnO_6 octahedra [59]. Figure 4.1 shows the behavior of the lattice parameters in the whole temperature range. Parameters a and c decrease with temperature in region below $T_{N,B}$ while parameter b increases with temperature in all phases. Panel b shows that the monoclinic angle β decreases at a steeper pace between $T_{N,A'}$ and $T_{N,B}$. These effects of magnetic order over lattice parameters make $LaMn_7O_{12}$ a promising candidate to multiferroic material with robust coupling. The manner in which crystalline symmetry determines a different magnetic order in the A' and B sites also seems to support that scenario.

The point of view of magnetic structure, the A' Mn ions in $LaMn_7O_{12}$ order at $T_{N,A'} = 21$ K, as seen in the neutron diffraction data in panel c figure 4.1. The refined antiferromagnetic structure can be seen in panel a of figure 4.2. The B site in the other hand, orders at $T_{N,B} = 78$ K (see panel c in figure 4.1), but the refined magnetic structure (panel b of figure 4.2) was found to be a C-type, which consists of antiferromagnetic ac planes coupled ferromagnetically. This is very different from the A-type structure of $LaMnO_3$, which is composed of ferromagnetic ac planes coupled antiferromagnetically.

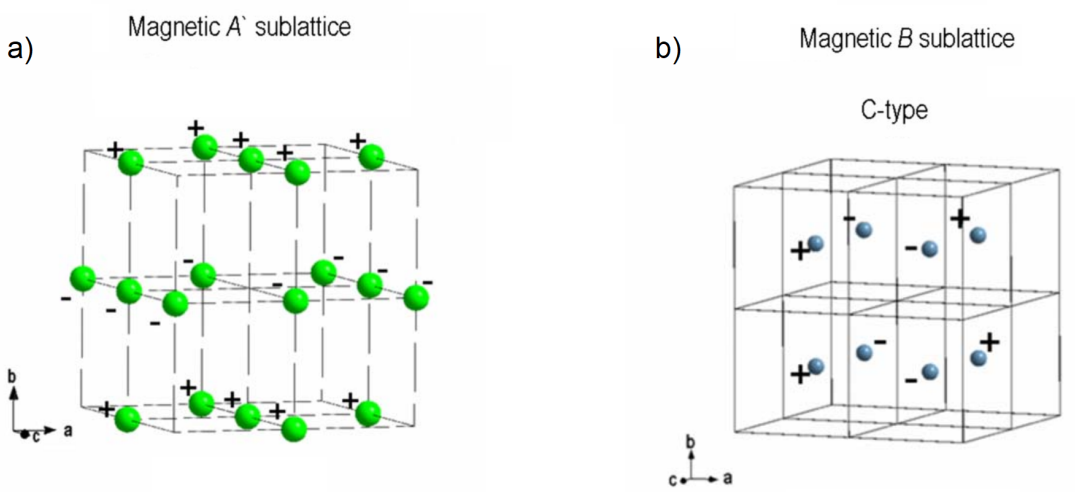

Figure 4.2 – a) C-type antiferromagnetic structure of the B-site in $LaMn_7O_{12}$. Besides from opposing magnetic moments, + and - signs also differentiates the 4e and 4f sites in the $I2/m$ structure. Adapted from [59].

The difference has two main causes. The first being that the two distinct positions occupied by Mn sites in the B sites (4e and 4f) cause very small differences in the $Mn-O$ bond lengths for different sites, leading to different superexchange interactions in different positions in the B site sublattice. The other reflects the fact that, as shown in figure 4.2 b, the 4e and 4f positions in the B site have opposing magnetic moment, which is not

allowed by the symmetry properties of the *Pnma* space group of $LaMnO_3$. Furthermore, being in a distinct crystallographic site with a completely different coordination, the Mn A' sublattice is unfit for comparison to $LaMnO_3$.

Regarding electric transport, $LaMn_7O_{12}$ provides a much simpler picture than the similar compound $NaMn_7O_{12}$. DC electric resistivity for a $LaMn_7O_{12}$ polycrystalline pellet can be seen in figure 4.1 d. As expected from the half-filled e_g bands of the octahedral Mn ions, $LaMn_7O_{12}$ behaves as an insulator through the whole temperature range. The inset shows the typical Arrhenius thermally activated behavior with an activation energy of 0.22 eV.

4.2 Magnetic Characterization

The magnetic characterization was performed in GSM using the Quantum Design MPMS 3 SQUID-VSM in single $LaMn_7O_{12}$ crystals. These measurements were performed in the zero-field cooling/field cooling (ZFC/FC) protocol. That is, the sample is first cooled from the disordered phase to 5 K with no magnetic field applied (ZFC), the field is then turned on and the sample is heated above its paramagnetic transition while magnetization is measured. Finally, with the field still on, the sample is cooled again while this field cooled (FC) magnetization curve is measured. The results of magnetic moment as a function of temperature were show in figure 4.3. These results are consistent with previous work [59]. In these measurements is possible to identify both magnetic transitions at $T_{N,A'} =$ 21 K and $T_{N,B} = 78$ K, but the transition of the B site resembles more a ferromagnetic transition than an antiferromagnetic one, with a sharp rise in magnetization.

This can be explained in terms of the so-called weak ferromagnetism, caused by the canting of the moments in the AFM lattice that can be caused by the Dzyaloshinsky-Moriya (DM) interaction. Canting via DM interaction requires particularly asymmetric deformations in the magnetic sublattices, a condition that is met by the buckled octahedra in the quadruple perovskite structure [59]. Since the canted component of the moment is very small, this picture is consistent to the determined magnetic structure. Moreover, the downturn in magnetization that can be seen at $T_{N,A'}$ is typically antiferromagnetic, which indicates that, as expected, only the B lattice is subject to the canting.

On the other hand, the transition temperature $T_{N,A'}$, while precisely at 21 K in the low field measurements (4.3 a and b), seems to shift to lower temperatures at higher fields (4.3 c and d). This is actually not true. Panel f of figure 4.3 shows the signature of the phase transition at 21 K even at the highest measured field (panel e). The shift of local maxima in panels a to e is due to the sum of the B site weak ferromagnetic component of the magnetization with the usual linear temperature response of an antiferromagnet (which can be seen very clearly in panel d, for example).

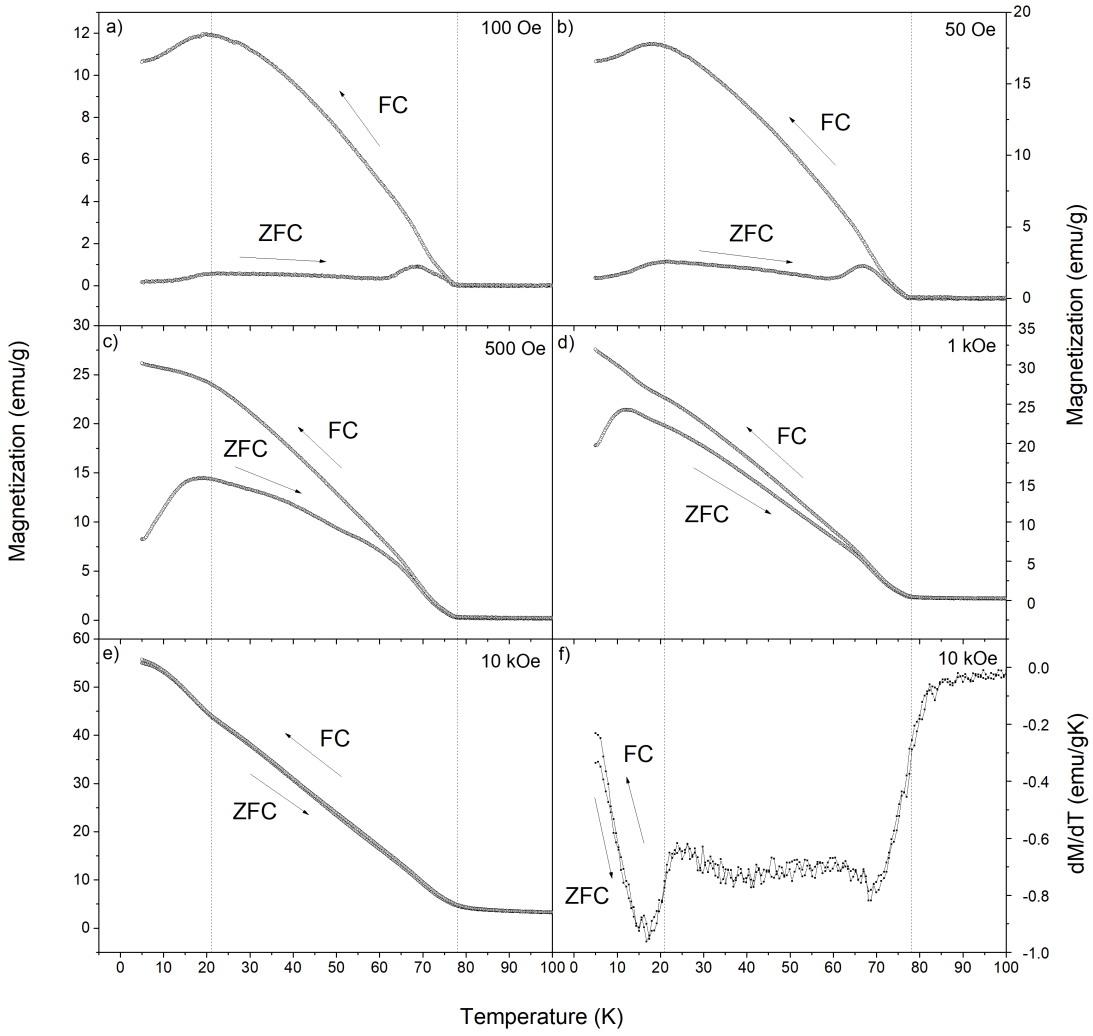

Figure 4.3 – Magnetization versus temperature for a single unoriented $LaMn_7O_{12}$ crystal under 50 Oe (a), 100 Oe (b), 500 Oe (c), 1 kOe (d) and 10 kOe (e). Panel (f) shows the derivative with respect to temperature of the curve shown in panel (e). Dashed lines show transition temperatures described in text.

Magnetization as a function of applied magnetic field measurements are presented at figure 4.4. The change in the non-saturated AFM-like slope of the MxH curve from 20 to 30 K while the remnant magnetization and coercive fields remain unchanged shows that the canted ferromagnetism found in the MxT curves belongs to the B site, and that the response of the A' site is purely antiferromagnetic. This is confirmed by the $T_{N,B}$ transition, when the spontaneous magnetization and hysteretic behavior disappear. Also, the non-saturated behavior of the curves at high magnetic fields, combined with the very quick rise in magnetization at low fields, show that the weak FM component saturates at

around 500 Oe, and the high field response is dominated by AFM behavior.

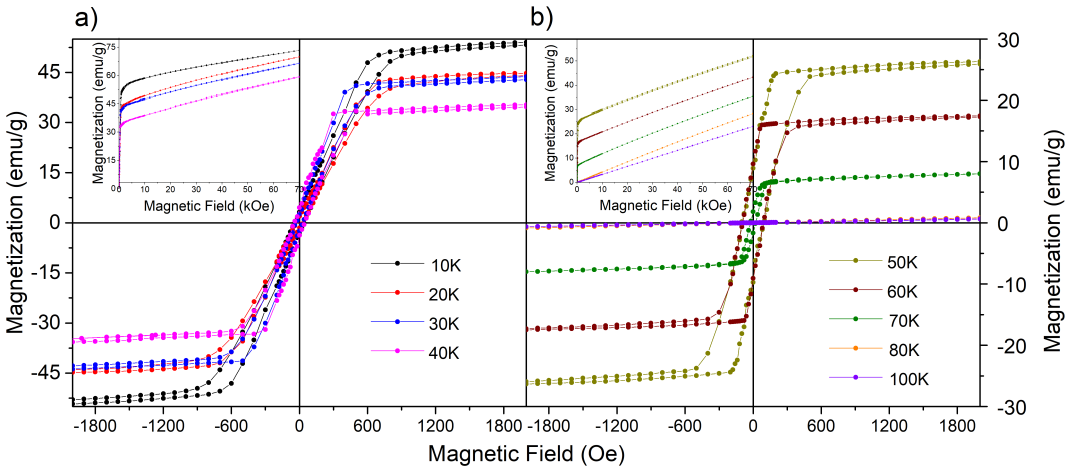

Figure 4.4 – Magnetization as a function of applied magnetic field of a single unoriented crystal of $LaMn_7O_{12}$ at lower (a) and higher (b) temperatures. Panels divided for clarity.

4.3 Magnetoelectric Measurements

The changes in lattice behavior at magnetic transitions, a magnetic structure greatly influenced by crystal symmetry, and a weak ferromagnetic canted component of the magnetization highly dependent of MnO_6 buckling (which is very important for ferroelectricity) all hint at the possibility of multiferroicity and magnetoelectric coupling in $LaMn_7O_{12}$.

In order to search for magnetoelectric coupling, one quadrant magnetization measurements were performed in a $LaMn_7O_{12}$ polycrystalline pellet (because single crystals are too small to place electric leads) using the homemade sample holder in the MPMS 3, at GSM. The following pooling procedure was applied in order to get a polarized state in any possible electric ordering that might coexist with a magnetic ordered phase. The sample was first cooled to 70 K and the pooling field was applied (see figure 4.5), the sample was then cooled to 60 K and kept for a 30-minute pooling time. It was then cooled still under electric field to the measuring temperature K and the magnetization measurements were performed with the electric field still on via the extraction method, since the homemade sample could be damaged by the VSM method.

Results can be seen in figure 4.5. The electric field didn't seem to have any effect over the magnetization curves in any of the ordered phases (panels a and b) and neither close to the transition temperature of the B site. The temperature sweeps also failed to show any sign of coupling over magnetization. The minute differences that can be seen are attributed to limitations in the experiment and equipment resolution. The main reason

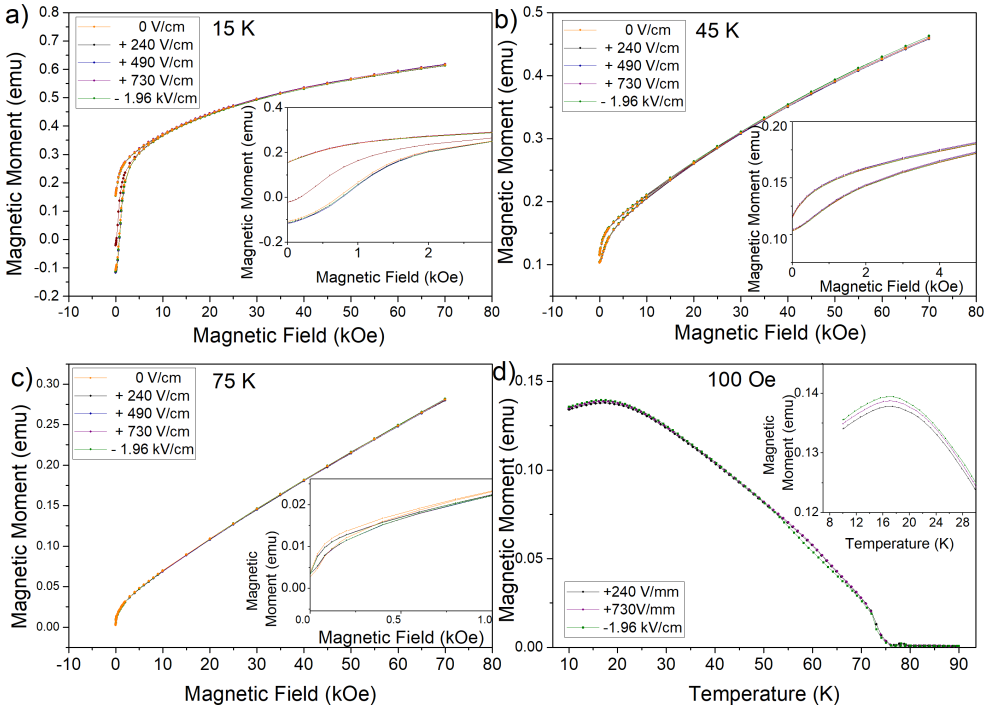

Figure 4.5 – One quadrant magnetization of a $LaMn_7O_{12}$ polycrystalline pellet versus magnetic field under different electric fields at 15 K (a), 45 K (b) and 75 K (c). d) Temperature evolution of field cooled (FC) magnetization under 100 Oe for different magnetic fields.

to explain the lack of coupling are the small magnitudes of electric field that can be applied using the homemade sample holder, that has a 100 V voltage limit. The usage of thinner samples should permit the investigation of electric effects over magnetization in a higher electric field range. The method used in these measurements, namely the extraction method, is very sensitive to small changes in positioning of the sample, which also comes to explain the very small difference in the curves, which were not reproductible and have shown no specific trend with respect to the magnitude of the electric field.

In order to tackle the problem of ME coupling with a different approach, magneto-electric susceptibility measurements were performed at GSM on a $LaMn_7O_{12}$ polycrystalline pellet. The same pooling procedure was applied, with an added 10 minutes of short circuiting the sample after lifting the electric field at the measuring temperature. This is done to remove spatially accumulated charges that could compromise the experiment.

Figure 4.6 shows the ME coefficient and its behavior with the magnetic field at several different temperatures. It is remarkable that, as shown in the inset of figure 4.6, the maximum amplitude of the ME coefficient drops abruptly at temperatures higher than $T_{N,A'}$. Because of the octahedra buckling related spin canting, it was expected that the B

site would play the larger role.

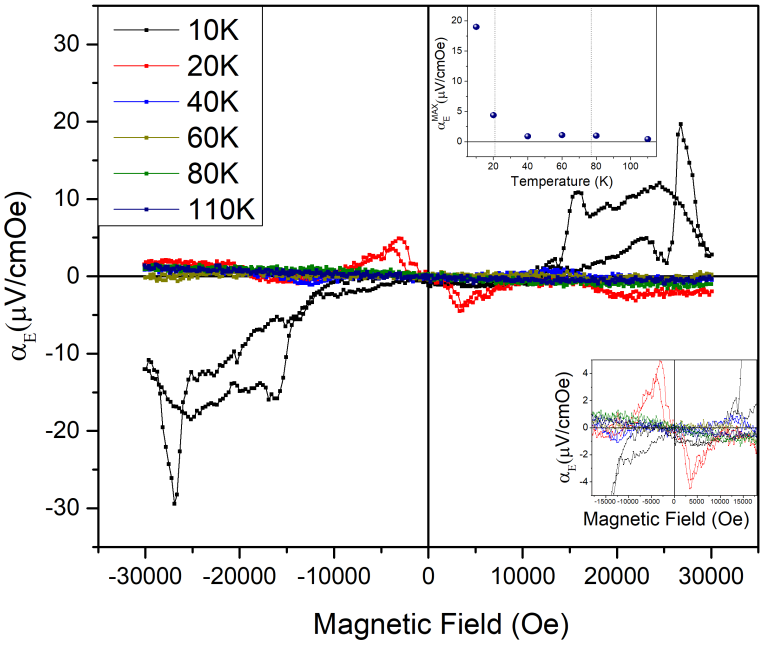

Figure 4.6 – Magnetoelectric susceptibility of a $LaMn_7O_{12}$ polycrystalline pellet as a function of magnetic field for different temperatures. Lower inset zooms the center regions to show other temperatures. Upper inset shows maximum amplitudes of ME coefficient as a function of temperatures.

It must be said, however, that at later attempts, this result could not be reproduced. Despite being a single instance, however, the clear relation to the magnetic order hints to the presence of magnetoelectric coupling in $LaMn_7O_{12}$, even if it has to be proven by different means.

4.4 Thermally Stimulated Currents

Another approach to detect multiferroicity and magnetoelectricity is to detect a ferroelectric transition coincident to a magnetic one, which points in the direction of a common origin. Moreover, magnetic control over the ferroelectric properties cements the coupling between the orders. Given the limitations of the homemade sample holder used to run pyroelectric current in the MPMS 3 cryostat, a more complete pyroelectric current study was performed by Prof. Flavio Milton at the Group of Ferroic Materials (GMF) at UFSCar's Physics Department, which is equipped with much more complete facilities for ferroelectric characterization. The protocol for pooling samples is similar to the ones used for magnetoelectric susceptibility. The sample are cooled in a closed-cycle cryostat to 100 K, and submitted to the 10 - 36 kV/cm for 30 minutes by a high voltage source.

The sample is then cooled up to 15 K, relieved of the electric field and short circuit for 10 minutes for the backflow of spatially distributed charges. Finally, the sample is heated at different rates.

A typical result can be seen in figure 4.7. A peak centered at $T_{Peak} = 74$ K was found. The inversion of the peak under a reversed electric field while other thermally stimulated currents conserve their polarity, as seen by the rising currents in the end of the scale in figure 4.7, makes a strong case for a ferroelectric transition at this temperature instead of other kinds of thermally stimulated currents caused by experimental artifacts like the ones reported in [75].

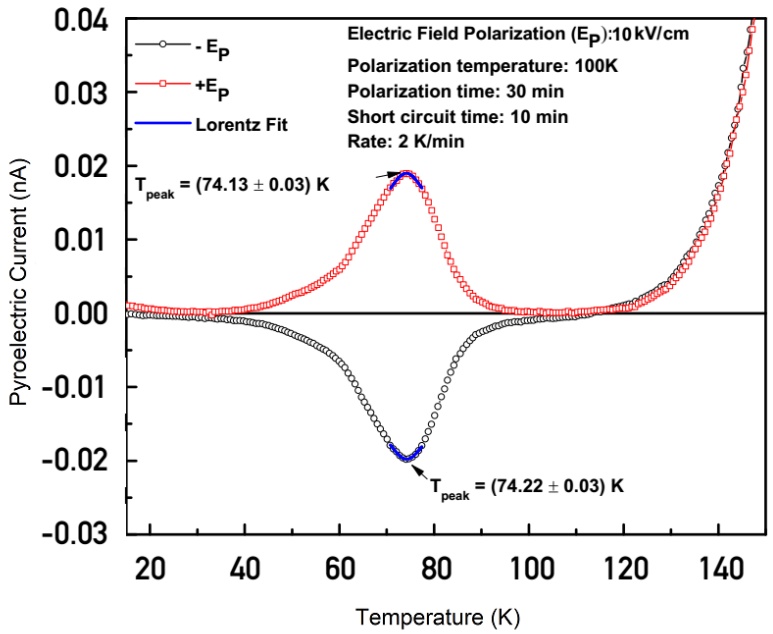

Figure 4.7 – Pyroelectric current profiles of a $LaMn_7O_{12}$ polycrystalline pellet in function of temperature for a pooling field of $E_P = \pm 10$ kV/cm, measured at a 2 K/min rate. Blue line shows a lorentzian fit.

Because the peak is very close to $T_{N,B}$, it is necessary to determine the transition temperature very carefully. Since the thermally stimulated current are proportional to heating rate, the signal quality can be enhanced with higher heating rates. On the other hand, faster heating rates lead to sample thermalization problems, that lead to a shift in the pyrocurrent peaks in the direction of higher temperatures. In order to precisely determine the transition temperature, a more careful study of the evolution of the peak position with the heating rate was performed, shown in figure 4.8. It can be seen that with higher rates, the peak shifts to the right very quickly, going quickly above the $T_{N,B}$. However, the measurements in the low rate end point to positions below $T_{N,B}$ and the lowest rate shows a position of $T_C = 74$ K for the ferroelectric transition.

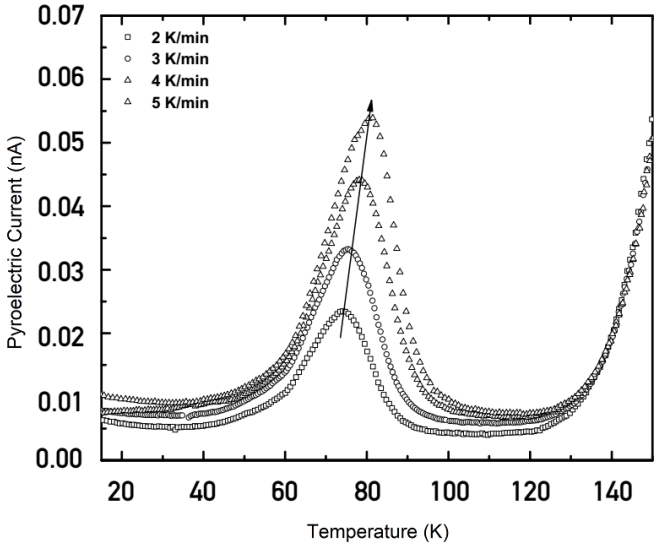

Figure 4.8 – Pyroelectric current profiles evolution of a $LaMn_7O_{12}$ polycrystalline pellet with respect to heating rate for a pooling field of $E_P = \pm 10$ kV/cm. The arrow indicates the shift of peak position with increasing rate.

Finally, the polarization was computed from the pyroelectric current profiles, the evolution of polarization with temperature for different electric fields can be seen in figure 4.9. Even at the lowest pooling field, we can see a remnant polarization of 0.22 $\mu C/cm^2$, in the same order of magnitude as reported for $CaMn_7O_{12}$ [34, 35]. At the highest applied field, an even higher value of 0.45 $\mu C/cm^2$ is achieved, with sings that saturation is still relatively far. An estimation using a Langevin model fit of the polarization predicts a value of 0.56 $\mu C/cm^2$ at saturation. This is the highest registered value of ferroelectric polarization in a single phase multiferroic, and the expectation is that for single crystals higher values of polarization can be achieved, reaching the order of magnitude of 1 $\mu C/cm^2$.

In order to probe for coupling between magnetic and the newly found electric order, pyroelectric current measurements were performed under magnetic field in the MPMS 3 cryostat, at GSM. The pooling procedure was the same as described before, with the magnetic field being introduced simultaneous to the electric field (with exception to one run, when the magnetic field was applied at low temperature immediately before starting the heating). As shown in figure 4.10 the magnetic field didn't seem to have any effect in the pyroelectric current profiles. Throughout the different scales of magnitude, the different in the current curves are within the limitations of the experiment, and the application of the ZFC protocol also didn't change this scenario. The phase under $T_{N,A'}$ was also unchanged, which is puzzling considering the evidence of ME coupling in this temperature range. Given that the ferroelectric transition is simultaneous to the magnetic transition of the B site, which is marked by a very lattice sensitive canted weak ferromagnetic component to the magnetization, the lack of effect of magnetic field over the electric polarization is puzzling, especially because of the large similar effect that is found in $CaMn_7O_{12}$ [34, 35].

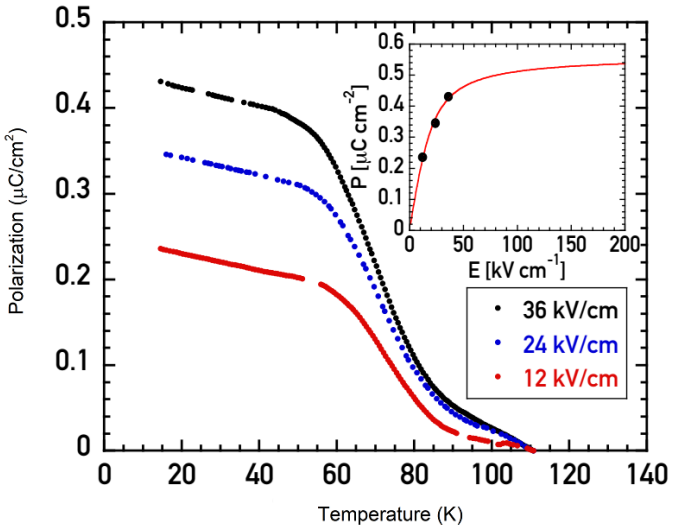

Figure 4.9 – Remnant polarization of a $LaMn_7O_{12}$ polycrystalline pellet versus temperature for different pooling fields. Inset shows electric field evolution of low temperature polarization. Red line shows a Langevin function fitting.

Perhaps, as with other materials, a higher magnetic field is necessary to a sizable effect over polarization [76].

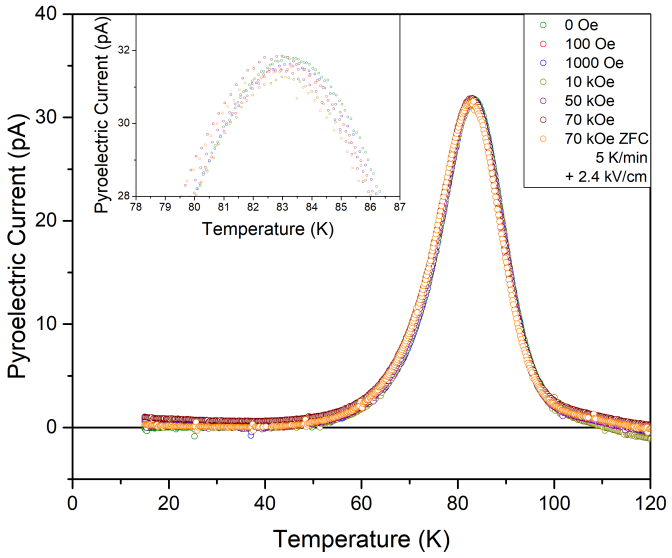

Figure 4.10 – Pyroelectric current profiles evolution of a $LaMn_7O_{12}$ polycrystalline pellet with respect to magnetic field for a pooling field of $E_P = \pm 2.4$ kV/cm. Heating rate of 5 K/min.

5 $\left(\mathbf{NaMn_3^{3+}}\right)\left(\mathbf{Mn_2^{3+}Mn_2^{4+}}\right)\mathbf{O_{12}}$

5.1 Introduction

In the family of quadruple perovskite manganites $AMn_3Mn_4O_{12}$, the sodium ion (Na^{1+}) in the A site provides a perfect one to one Mn^{3+}/Mn^{4+} balance in the B site, in sharp contrast with the single valence (Mn^{3+}) of $LaMn_7O_{12}$. At higher temperatures, $NaMn_7O_{12}$ crystallizes in a cubic ($Im\bar{3}$) structure with the Mn^{3+}/Mn^{4+} sharing the 8c positions in a disordered fashion. At 176 K, the material goes through a first-order structural transition into the monoclinic $Im/2$ space group, with the Mn^{3+} and Mn^{4+} ordering into the distinct 4e and 4f crystallographic positions [77]. The charge order and structural phase transition come accompanied by a commensurate structural modulation in the $\mathbf{q}_{CO} = \left(\frac{1}{2}, 0, -\frac{1}{2}\right)$ direction consisting of a zig-zag elongation pattern of octahedra containing the Mn^{3+} ions in the B site, as shown in figure 5.1 [78].

The monoclinic phase is characterized by a very large splitting in the $Mn-O$ distances and the volumes of the MnO_6 octahedra, as shown in figure 5.2 a-b. This picture is in agreement with the charge ordering since the $Mn^{3+}O_6$ octahedra are much larger than the $Mn^{4+}O_6$ ones [78]. It might at first seem from figure 5.2 a that in the monoclinic phase, the $Mn^{3+}O_6$ octahedra are compressed, since they present two $Mn-O$ bonds (4 and 1) larger than the third (2). However, this picture averages over adjacent cubic unit cells, like the 1 and 2 sites in figure 5.1 b, which are distorted in perpendicular directions. A more detailed analysis of $Mn-O$ bond lengths can be seen in table 5.1. The data in the table clarifies that the octahedra containing Mn^{3+} are elongated, and not compressed, in a way consistent with the structural distortion of figure 5.1 b and also clarifies how an averaging of the 1 and 2 positions (figure 5.1 b and table 5.1) produces the prior result of figure 5.2 a. This pictures also corroborates the larger volumes of the Mn^{3+} octahedra compared to the Mn^{4+} ones, as indicated to the bond valence sums. The larger dispersion of bond lengths (indicated by the Δ parameter in table 5.1) are consistent with the doubling of the unit cell that comes with the commensurate modulation since the same site (regarding the red unit cell of figure 5.1 b) can be placed in two different configurations (1 and 2 in figure 5.1 b) propagating in a zig-zag pattern in the $\mathbf{q}_{CO} = \left(\frac{1}{2}, 1, \frac{1}{2}\right)$ direction.

The elongation of the $Mn^{3+}O_6$ octahedra leads to an elongation of the e_g $3z^2 - r^2$ orbitals, so that an orbital ordering is also established with the structural modulation (see figure 5.1 b). Finally, since the Mn^{3+} e_g, electrons are Jahn-Teller active, this mechanism is thought to be an important driving force in this structural transition and distortion. Furthermore, the highly symmetrical position of the oxygen in the structure ($2/m$) and

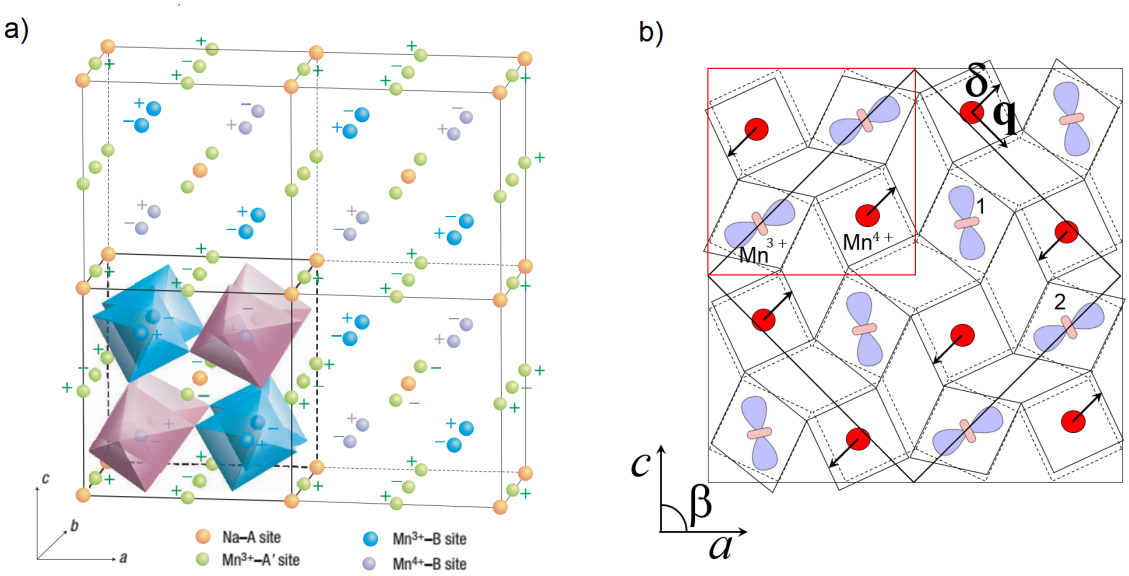

Figure 5.1 – a) $NaMn_7O_{12}$ unit cell showing charge and magnetic order patterns. Magnetic moments of Mn^{3+} in the A' and B lattices lie in the ac plane while those of Mn^{4+} in the B site are parallel to the c axis. Magnetic order shown by the + and - signs, representing up and down spins. Adapted from [77]. b) Model of the commensurate structural modulation in the monoclinic phase. The red square in the upper left corner show the undistorted cubic unit cell while the black tilted large square shows the modulated supercell. Solid and dashed lines show respectively the distorted and undistorted positions of the MnO_6 octahedra. The $\boldsymbol{\delta}$ vector shows the displacement of Mn^{4+} ions perpendicular to the propagation direction $\mathbf{q}_{CO}$. Labels 1 and 2 refer to sites referred to in table 5.1. Adapted from [78]

their high coordination lead to a nearly defect free charge-ordered structure. That means that $NaMn_7O_{12}$ is free from chemical disorder, unlike many other mixed valence perovskite compounds, with a perfect one to one charge imbalance.

A very interesting feature in $NaMn_7O_{12}$ electric properties can be seen in figure 5.2 c. The electric resistivity of $NaMn_7O_{12}$ experiences a sudden, two order of magnitude rise when going through the cubic to monoclinic transition at 176 K. This sudden jump in resistivity is reminiscent of a similar phenomenon that takes place in magnetite (Fe_3O_4), being first described by Verwey in 1939, which granted the phenomenon the name of Verwey transition [49]. The first hypothesis to explain this leap in resistivity assumed a simple charge ordering phenomenon (much like the one present in $NaMn_7O_{12}$) to be responsible, but this proved to be a too simplistic model for the complex structural distortion of magnetite. Recently, structural distortions involving triads of Fe ions, named trimerons [79], provided a more substantiated explanation. Nevertheless, the complexity of the structure is the main obstacle in the full understanding of this phenomenon. Presenting a much simpler structural distortion than magnetite, simpler even than the

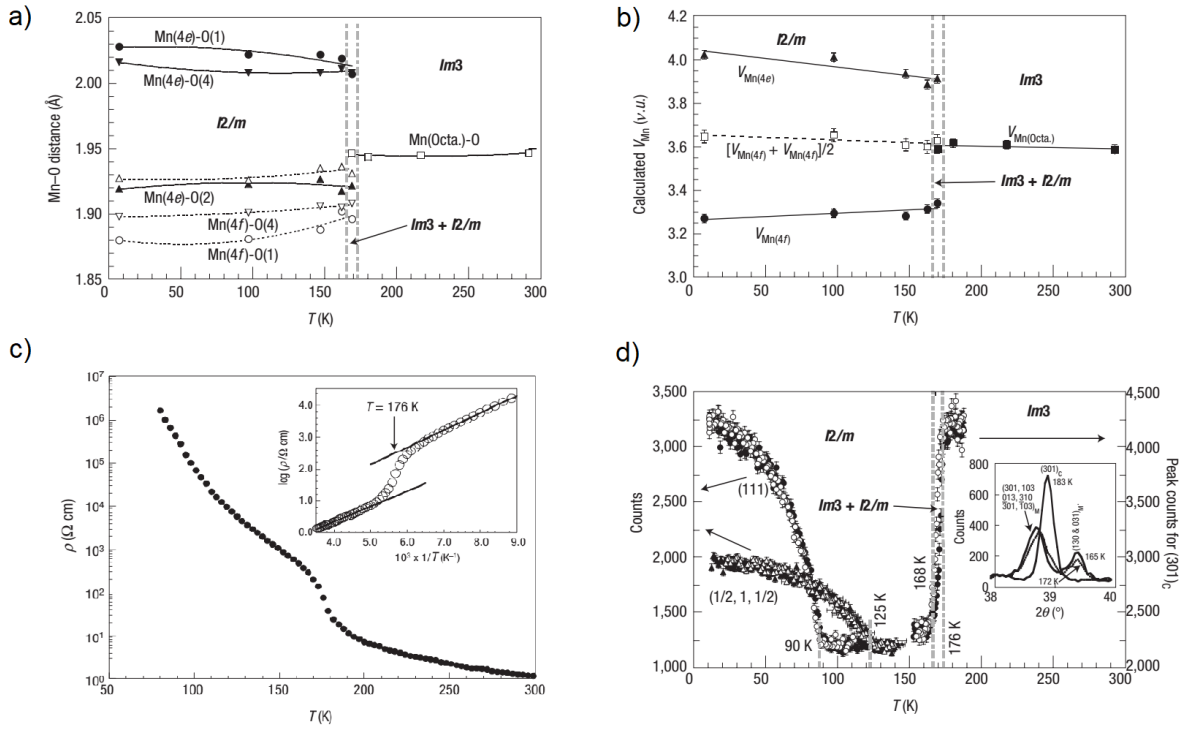

Figure 5.2 – Temperature evolution of $Mn-O$ distances (a), calculated volume of MnO_6 octahedra (b), electrical resistivity (c) and neutron diffraction intensity (d) for the reflections corresponding to the magnetic sublattice A' (111) and B $\left(\frac{1}{2}, 0, -\frac{1}{2}\right)$. The inset in (d) shows the splitting of the (301) peak in the cubic to monoclinic transition. Adapted from [77].

non-commensurate modulation in $CaMn_7O_{12}$ [40], the Verwey transition in $NaMn_7O_{12}$ is an interesting model to investigate the dynamic origins of this phenomenon, which couples charge, lattice, orbital and spin degrees of freedom.

Regarding the magnetic ordering, $NaMn_7O_{12}$ goes through two distinct antiferromagnetic transitions, which can be visualized in figure 5.1 a and which neutron diffraction intensities can be seen at figure 5.2 d. Panel d of figure 5.2 shows the neutron intensity of the (111) reflection, corresponding to the antiferromagnetic ordering of the Mn^{3+} ions in the A' sites, with magnetic moments lying in the ac plane. The Néel temperature for this magnetic sublattice is $T_{N,A'} = 92$ K and it orders as an anti-body centered antiferromagnet.

The B site magnetic order can be seen by the intensity of the $(\frac{1}{2}, 1, \frac{1}{2})$ reflection in figure 5.2 d. Both the Mn^{3+} and Mn^{4+} ions order in a CE-type antiferromagnetic structure as shown in figure 5.1 a. The Mn^{4+} magnetic moments are parallel do the c axis and the Mn^{3+} one lie in the ac plan like their A' site counterparts, both Mn^{3+} and Mn^{4+} at the B site order at a Néel temperature of $T_{N,B} = 125$ K.

Therefore, $NaMn_7O_{12}$ hosts a range of complex phenomena despite a relatively simple structure and distortion. A further understanding of how lattice, charge, orbital

Table 5.1 – $Mn-O$ bond distances for the two distinctly distorted Mn^{3+} (1 and 2, see figure 5.1 b) and the Mn^{4+} sites at the monoclinic phase at 4.2 K. Mean distance, bond valence sums (BVS) and the distortion parameter $\Delta = \frac{1}{6}\sum_{i=1}^{6}\left|\frac{d(Mn-O)-\langle d(Mn-O)\rangle}{\langle d(Mn-O)\rangle}\right|^2$ also reported. Adapted from [78].

Mn B site	Mn^{3+} (1)	Mn^{3+} (2)	Mn^{4+}
$d(Mn-O)$ (Å)	1.922	1.922	1.929
	1.922	1.922	1.929
	2.114	1.955	1.883
	2.114	1.955	1.883
	1.974	2.067	1.900
	1.974	2.067	1.900
$\langle d(Mn-O)\rangle$ (Å)	2.003	1.981	1.904
BVS	3.18	3.34	3.99
$\Delta(\times 10^{-4})$	16.33	9.84	1.00

and spin degrees of freedom couple and interact in this system might shed a new light into how complex phenomena arise in more complex systems. In particular, the driving interactions behind the structural instabilities and the mechanisms of multiferroicity in this system are a particularly fertile ground for advancing the understanding of strongly correlated systems.

5.2 Diffuse X-Ray Scattering

Much can be learned from the way that lattice, charge, orbital and spin degrees of freedom couple in $NaMn_7O_{12}$ by studying the driving mechanisms of the structural changes that the material undergoes at 176 K. Incipient ordering above transition temperature and short-range correlations can be probed via diffuse x-ray scattering (DXS).

The diffuse x-ray scattering measurements were performed at the ID-29 beamline in the European Synchrotron Radiation Facility (ESRF). A $NaMn_7O_{12}$ single crystal with dimensions around 70 μm was submitted to shutterless exposure to a wavelength of 0.715 Å, scattered light was collected in the PILATUS 2M detector [73]. The sample rotation axis was perpendicular to the beam and parallel to the beam polarization. The resolution was of 0.1° per image and each image had a 0.6 s exposure time. Raw data was analyzed using the CrysAlis software and reconstructed using ESRF-made software, Laue symmetry was applied to the data in the reconstruction process.

The expected result was to find, as T_{CO} is approached from above, short range correlation around the modulation wavevector as an indicator of incipient order, as found in $CaMn_7O_{12}$ [40]. In the cubic phase, due to crystal twinning in the monoclinic transition, diffuse spots were expected at positions $\mathbf{q}_{CO} = \left(h \pm \frac{1}{2}, k \pm \frac{1}{2}, l \pm \frac{1}{2}\right)$.

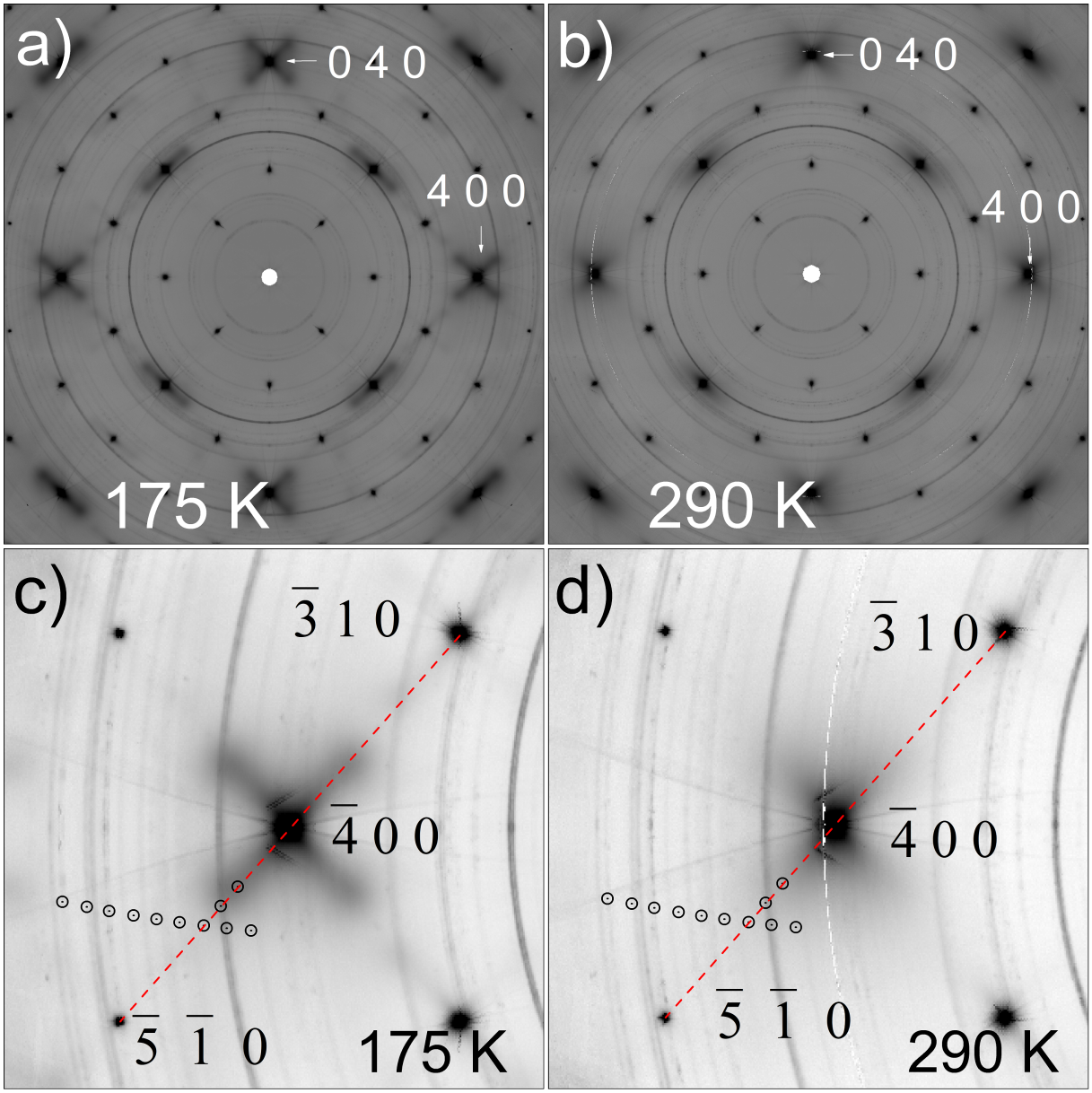

Figure 5.3 – Upper panels: reconstructed maps of reciprocal plane (hk0) acquired at 175 K (a) and room temperature (b). Lower panels: Close-up in the vicinity of the Bragg reflection $\left(\bar{4}00\right)$ at 175 K (c) and room temperature (d). Black-dotted circles represent the reciprocal space positions measured in the IXS experiment. The red-dashed line indicates the direction of the intensity profiles shown in figure 5.4.

The result, however, was unexpected. At room temperature, no features beyond the tails of the Bragg peaks could be observed, as seen in figure 5.3 b and figure 5.4. As temperature decreases, diffuse satellite peaks progressively appear at the positions $\left(h \pm \frac{1}{3}, k \pm \frac{1}{3}, 0\right)$, as seen in panel a of figure 5.3 and in figure 5.4. It's important to remark that, although most visible in the most intense Bragg peaks, like (400), these satellite diffuse peaks are present in all Bragg reflections. The intensity of these peaks intensifies as temperature decreases, then they disappear when the system enters the monoclinic phase.

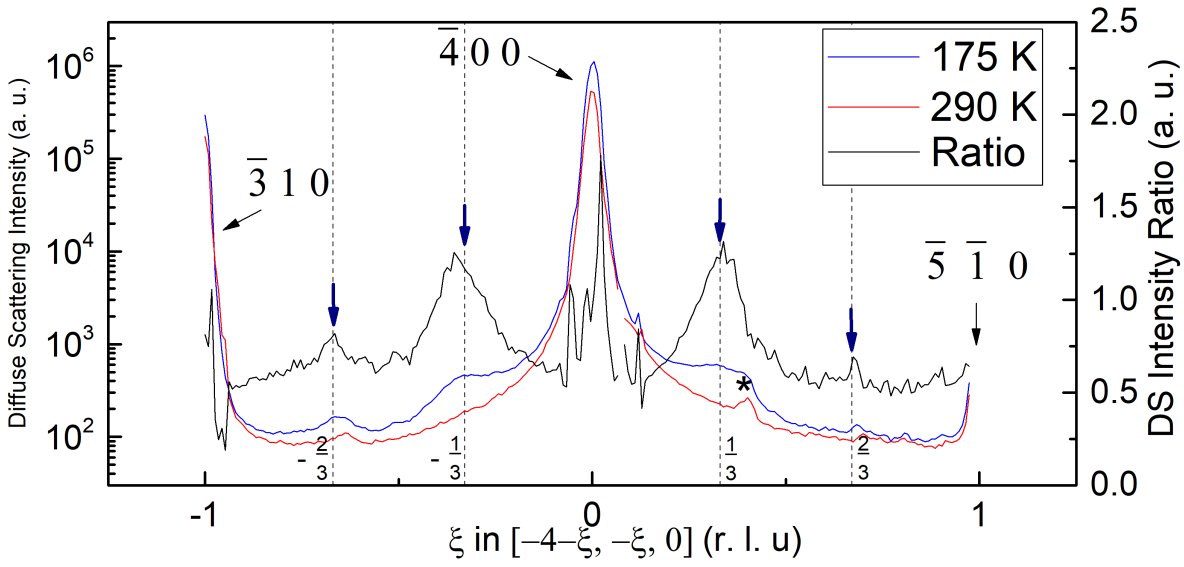

Figure 5.4 – Diffuse scattering intensity profile (red and blue lines) and intensity ratio (black line) in the $(-4-\xi, -\xi, 0)$ direction, blue arrows at $\mathbf{q} = \left(h \pm \frac{1}{3}, k \pm \frac{1}{3}, 0\right)$. Asterisk indicates the polycrystalline contribution to the diffraction pattern, which appears as the characteristic ring in the diffraction patterns of figure 5.3.

The transition is made clear by the appearance of the commensurate modulation peaks at the $\left(h \pm \frac{1}{2}, k \pm \frac{1}{2}, l \pm \frac{1}{2}\right)$, the satellites peaks of the modulation appear in all crystalline directions due to the twinning of the sample during the transition.

Contrary to the expectations, instead of finding short range correlations with commensurate modulation wavevector $\mathbf{q}_{CO} = \left(\frac{1}{2}, \frac{1}{2}, 0\right)$, a different 3-unit-cell-sized correlation was detected, with a wavevector $\mathbf{q}_{DS} = \left(\frac{1}{3}, \frac{1}{3}, 0\right)$. This is in contrast with the case of $CaMn_7O_{12}$, where signs of the structural modulation can be seen at a higher temperature as diffuse, short range order with the same wavevector [40]. One possible explanation for the different observed wavevector $\mathbf{q}_{CO}$ and $\mathbf{q}_{DS}$ are two competing structural instabilities, with $\mathbf{q}_{CO}$ appearing only at lower temperatures and abruptly overcoming $\mathbf{q}_{DS}$. But in order to study the dynamical instability at $\mathbf{q}_{CO}$, a study of softened phonons via inelastic x-ray scattering is necessary.

5.3 Inelastic X-Ray Scattering

To probe the dynamic aspects of the charge ordering transition at 176 K, we performed inelastic x-ray scattering experiments. This would allow the analysis of the behavior of phonons during the transition. Softening of phonons with displacement patterns similar to the low-symmetry phase distortion, which can be probed with inelastic x-ray scattering, can give important insights into the mechanisms that cause the structural

instability that lead to the phase transition. The experiments were performed in the ID28 beamline of the ESRF under a wavelength of 0.6968 Å and using a (999) silicon monochromator, which yielded an energy resolution 2.4 meV. Like in the DXS experiments, the spectra were taken at room temperature and at 175 K, which was the lowest temperature that could be achieved before the monoclinic transition is detected. Since the experiment would be rendered impossible in the monoclinic phase due to sample twinning, the best approach was to lower the temperature to just immediately before the appearance of the low temperature phase satellite peaks and probe the region of thermodynamic fluctuations that ensues in the vicinity of the transition temperature.

The (400) Bragg peak was chosen as a base for the acquisitions due to its great intensity (as seen in figure 5.3 and in [78]), which would provide higher photon counts than other positions in the reciprocal space. Therefore, the line $(-4-\xi, -\xi, 0)$ was chosen for data acquisition, probing the Σ line up to the N point. Because of the architecture of the array of detectors in the beamline, data from other positions is simultaneously obtained, which allowed for further analysis. A map localizing the analyzed positions in the reciprocal space can be seen in figure 5.5.

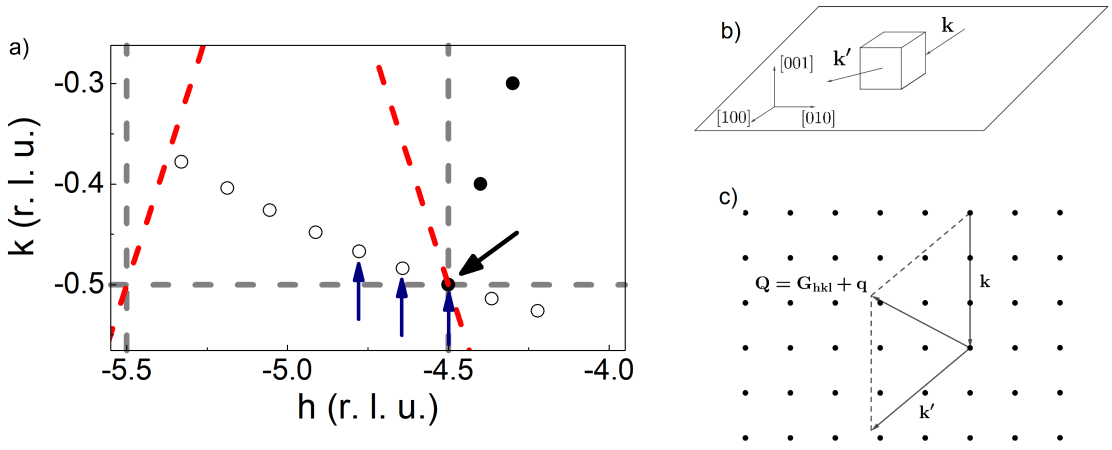

Figure 5.5 – a) Map showing the investigated region of the (hk0) reciprocal plane, filled circles represent points in the Σ line and empty circles show the positions of other detectors in the array. Black arrow indicates the N point, blue arrows indicate the position of the spectra shown in figure 5.7. Dashed lines indicate the Brillouin zone boundary of the cubic (red) and monoclinic (gray) unit cells. b) Schematic illustration of the geometry of the IXS experiment. $\mathbf{k}$ and $\mathbf{k}'$ lie in the scattering plane, perpendicular to the [001] direction. c) Representation of the incoming and scattered photon wave vectors and their relation to the exchanged momentum $\mathbf{Q}$ and reciprocal lattice vectors $\mathbf{G}_{hk0}$.

From the spectra that were taken, the dispersion relation along the Σ line could be determined, as shown in figure 5.6 a. The phonon peaks in the spectra are fitted

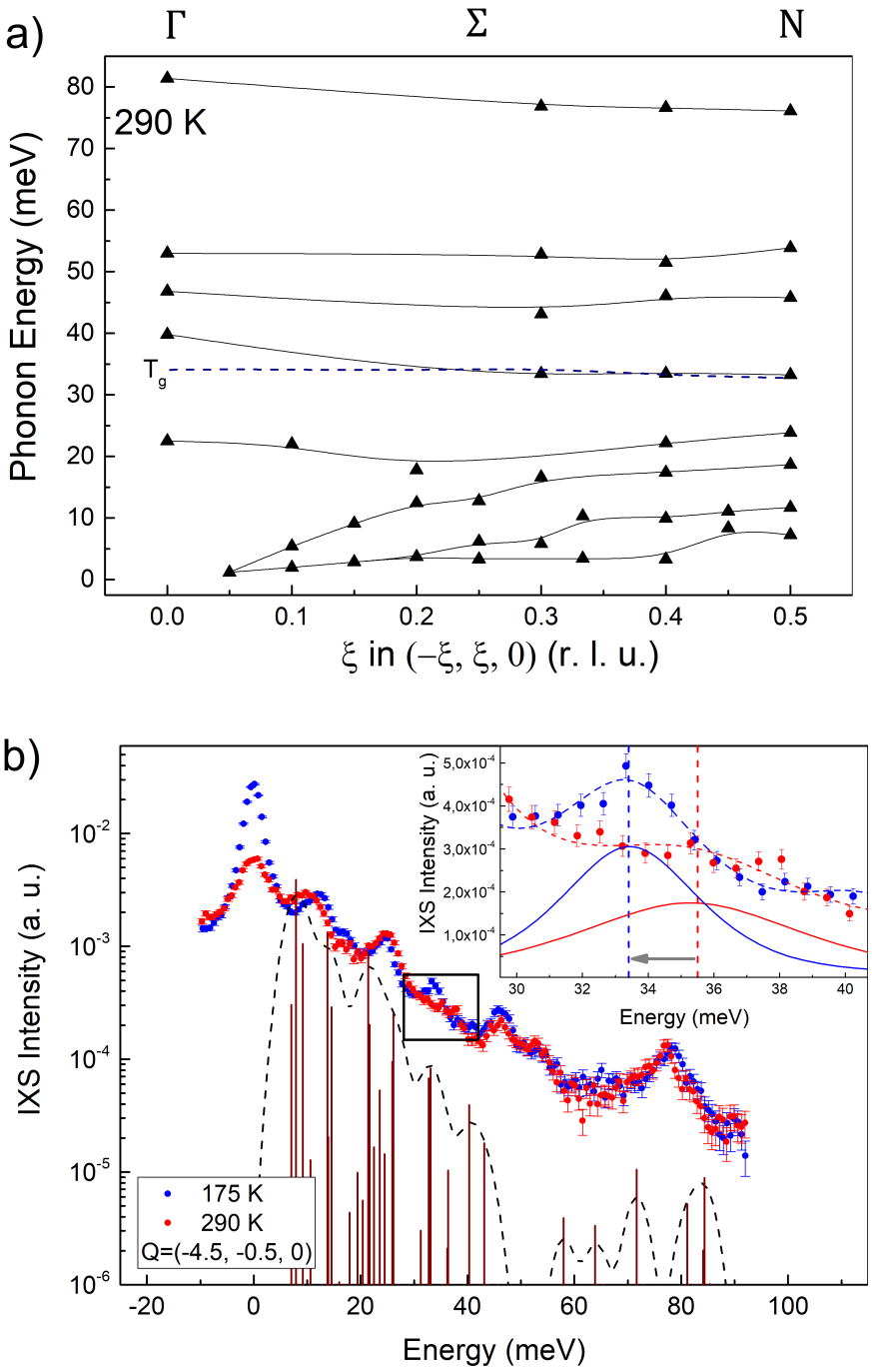

Figure 5.6 – a) Phonon dispersion in the $[\bar{1}10]$ direction at 290 K. Data at the Γ point taken from Raman experiments. Dashed blue line shows calculated dispersion and symmetry of the softened phonon. Black solid lines are guides to the eye. b) IXS spectra for the critical wavevector $\mathbf{Q}$ =(-4.5 -0.5 0) for 290 and 175 K. Dashed black lines show calculated intensities for phonons with frequencies and individual intensities indicated by red bars. Inset shows the phonon softening around 35 meV. Solid lines show individual fittings of the shown peaks and dashed lines show cumulative fittings with other peaks (not shown), vertical dashed lines show central frequencies and gray arrow emphasized the phonon softening.

using a pseudo-Voigt function with a fixed weight, while the elastic line was fitted using independent gaussian and lorentzian components to account for instrumental resolution and quasi-elastic scattering respectively. Figure 5.6 shows the three expected optical phonon branches, as well as several other optical branches. It is not possible to observe the total 60 phonon branches expected from a unit cell containing 20 atoms, for which there are two main reasons. Many phonons will have very close energy values, which makes their distinction hard even under the experimental resolution of 2.4 meV [41]. Additionally, many of the phonon modes will have low scattering cross sections at the explored region of the reciprocal space, which will lead to low photon intensities, rendering them undetectable. Both these effects can be seen in the calculated intensity and frequency profile to which we had access in figure 5.6 b, take note that many red bars are very close together, while other predict very low intensity.

Figure 5.6 b also shows a significant softening of a phonon with energy around 35 meV when going from room to near charge ordering temperature. Because of lesser thermal agitation and shortening of bonds in lower temperatures, the expected low-temperature behavior is a stiffening of the phonons, which can be observed for most of the other peaks in the spectra of figure 5.6 b, usually with an increase of around 2 meV phonon energies. The ideal conditions to observe the softening would be going completely into the monoclinic phase and observing the phonon energy of the soft mode approach zero. But as already mentioned, the twinning of the sample would make that impossible. Therefore, given the restriction to the region of thermodynamic fluctuation of the cubic phase, it's remarkable that the observed softening not only overcomes the expected hardening of phonon in lower temperatures, but also overcomes it by around 6% of its high temperature energy.

Further evidence of the phonon softening comes from the secondary detectors in the bank, represented by open circles in figure 5.5 a. Although they are located slightly above and below the scattering plane when compared to the main detector (estimated at 10^{-4}-10^{-3} reciprocal lattice units (r. l. u.) compared to 10^{-6} of the main detector), they still provide useful data to analyze the softening phenomenon from another direction. Additionally, the detectors' positions get closer to the scattering plane as they approach the main detector. As shown in figure 5.7 d-f, the phonon in question goes from the expected thermal hardening far from $\mathbf{q}_{CO}$ (panel d) to anomalous softening when reaching the modulation wavevector (panel f). This is reproduced in the [110] direction as shown in the inset of figure 5.7 a, where the phonon only softens when reaching $\mathbf{q}_{CO}$. The main panel in figure 5.7 a also shows that far from the critical wavevector the phonon hardens as expected, except at the extremities, which might be due to less precise positioning of the detectors far from (-4.5 -0.5 0) or even due to the approaching of $\mathbf{q}_{CO}$ under a different reciprocal lattice vector G_{hk0}.

To better understand these results, lattice dynamics calculations, performed by

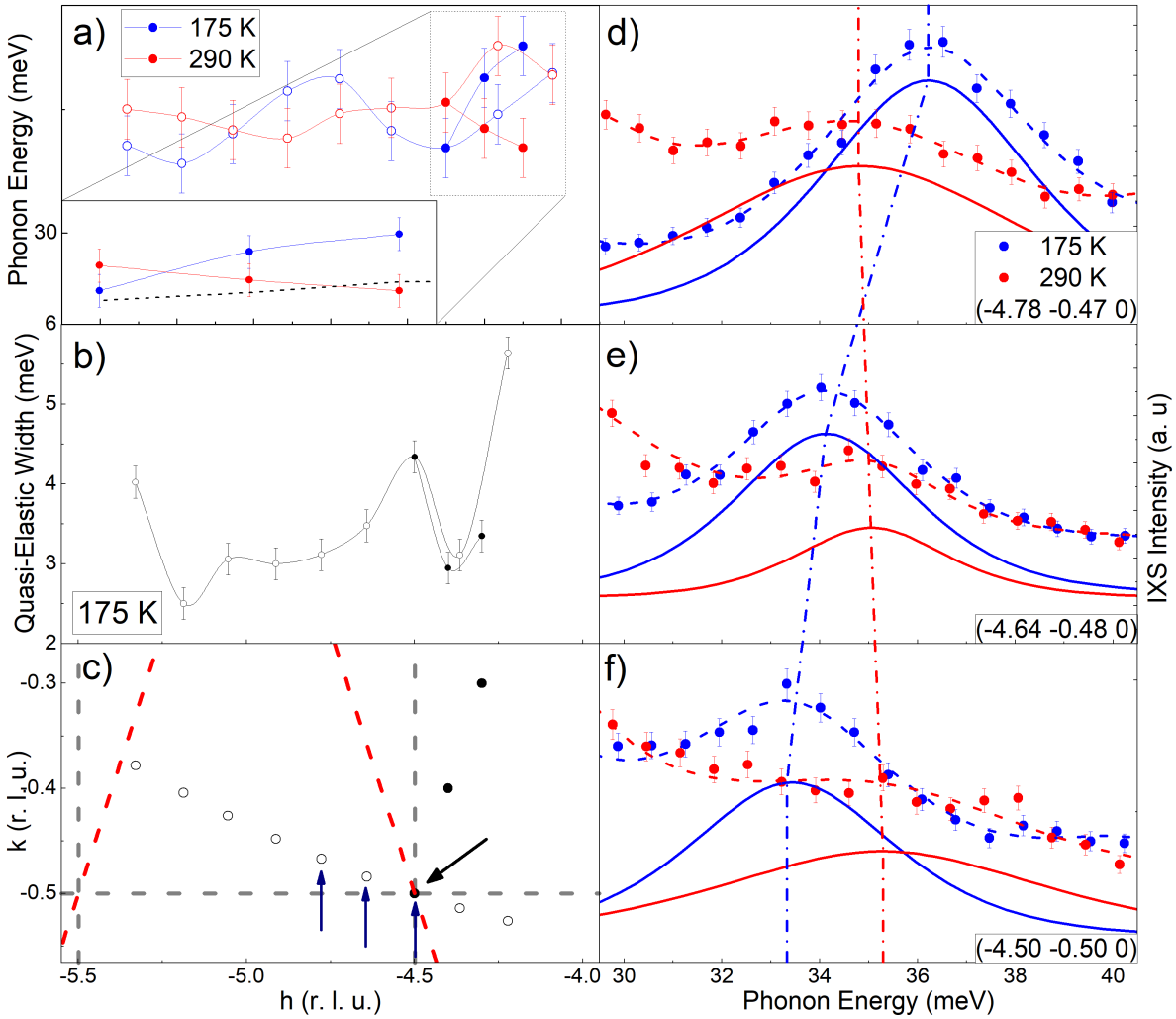

Figure 5.7 – a) Dispersion of the soft mode along the [110] direction (filled symbols and inset, with calculated dispersion shown in dashed line) and along the diagonal direction indicated in panel (c) (open symbols). Full symbols refer to the main detector of the detector array. Open symbols refer to the others detectors located slightly above and below the scattering plane. Note the mode softening seen in both data sets by approaching the critical wave vector $\mathbf{Q}* = \mathbf{G}_{400} + \mathbf{q}_{CO}$. b) Width of the quasi-elastic peak as a function of wave vector. Symbols are as above. c) Map showing the investigated region of the (hk0) reciprocal plane as in figure 5.5 for reference to panels (a) and (b). Black arrow indicates the N point, blue arrows indicate the position of the spectra shown in the left panels. (d) to (f) : close-up of the IXS spectra taken at (-4.50 -0.50 0) (d), (-4.64 -0.48 0) (e) and (-4.78 -0.47 0) (f), where the phonon softening is observed. Solid lines are pseudo-Voigt fits of the soft mode, dashed lines are a fit of the whole spectrum including contribution of other modes (not shown). Dashed-dot lines are a guide to the eyes showing the evolution of the peak position as a function of $\mathbf{Q}$.

M. N. Rao and described in [41], were incorporated to the analysis. As seen in figure 5.6 b, the calculations agree sufficiently in regards to position and intensity of the phonon peaks to be considered a valid description of the system. There are three phonon modes with energies in the vicinity of that of the soft mode, one of which is orders of magnitudes less intense than the other and was discarded. Among the other two, the displacement pattern and symmetry properties allowed for the attribution of the T_g mode with energy of 32.7 meV. The atomic displacements of this mode at Γ and $\mathbf{q}_{CO}$ points are displayed in figure 5.8. At $\mathbf{q}_{CO}$, the point group of the distorted structure is C_{2h}, coincident with the monoclinic structure. At Γ, it retains the same point group as the cubic structure, T_h, which is decomposed into A_g and B_g modes when going into the less symmetric group. Being invariant under z axis inversion (which, because of the cubic symmetry we identify with the monoclinic axis b in figure 5.8), it belongs to an A_g irreducible representation, containing all and only the symmetry elements of the monoclinic point group C_{2h}.

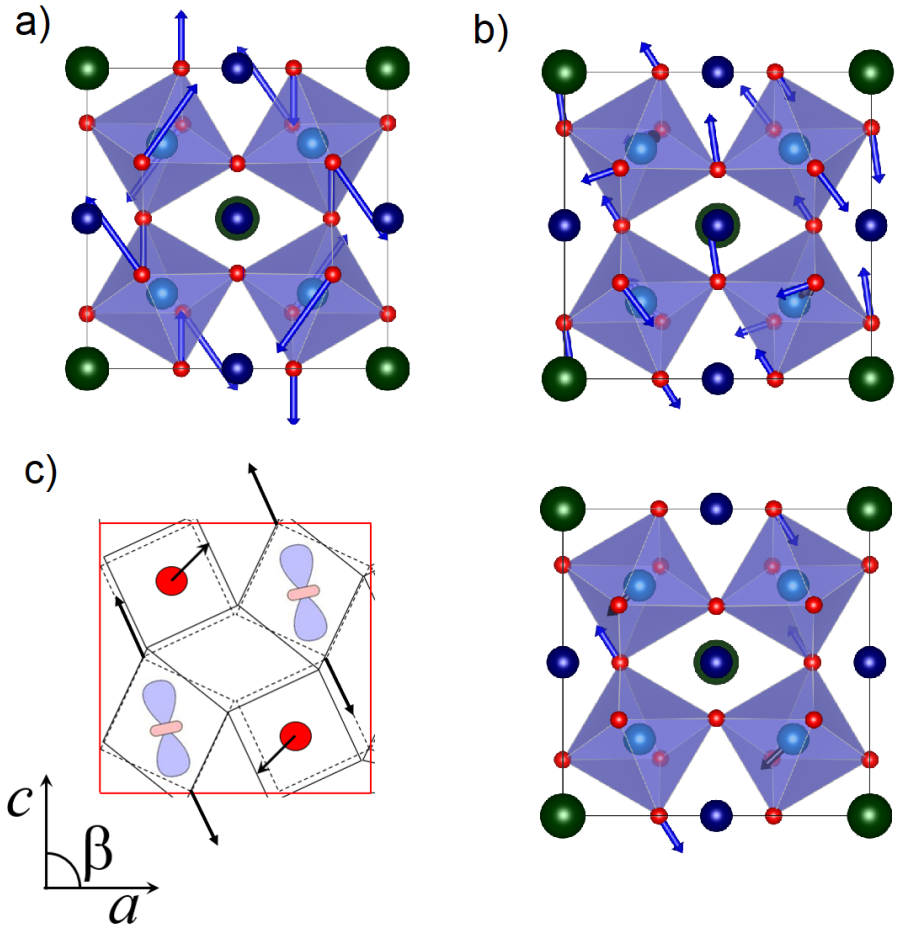

Figure 5.8 – (a)-(b) Calculated displacements of oxygen and B-site Mn for the softened phonon mode at Γ point (a) and N point (b). (c) Shows a comparison between a selected section of the commensurate structural distortion (right) a simplified representation of the soft mode at N point. Note that the blue arrows represent a vibration in the represented direction.

In this mode, and at $\mathbf{q}_{CO}$, half of the MnO_6 octahedra vibrates in a Jahn-Teller-like elongation/compression fashion while the remaining have large displacements of B-site Mn ions with no significant change in octahedra volume (see figure 5.8 b). This of alternating B-sites Mn ions and apical stretching/compression of MnO_6 octahedra propagation in the [101] direction keeps a remarkable similarity with the distortion found in the structural modulation [78]. The similarities between the structural distortion and the soft phonon is emphasized by the selected displacement directions in figure 5.8 c. This similarity with the monoclinic structure explains the softening of this phonon mode, and the presence of many Jahn-Teller active ions shows that the Jahn-Teller effect plays an important role in the instability of the high temperature, cubic structure of $NaMn_7O_{12}$.

An interesting phenomenon builds a link between the phenomena found in the diffuse x-ray scattering and inelastic x-ray scattering. The elastic peaks in the acquired spectra are significantly broader than instrumental resolution, as seen in figure 5.6 b. A possible explanation for this would be low energy acoustic phonons but the dispersion relation in figure 5.6 a shows that these have been detected and accounted for, the acoustic phonon peaks can even be seen in the low energy end of figure 5.6 b. Furthermore, there is a large difference in intensity of the elastic peak with respect to temperature (see figure 5.6 b), which is not expected in IXS experiments. There have been previous reports of quasi-elastic (QE) scattering in IXS experiments which were correlated with DXS features [68]. Therefore, we separated the fitting of the elastic peak into a Gaussian component, correspondent to the instrumental resolution of the beamline, and a Lorentzian one, correspondent to the quasi-elastic scattering. The first finding of this analysis was that the Lorentzian component could only be found at low temperature, the amplitude of the Lorentzian peak converged to zero in all room temperature peaks. This is strikingly similar of how the diffuse scattering features were absent at room temperature, so the amplitude of Lorentzian components is compared to DXS amplitude in figure 5.9.

The correlation between the amplitude the QE peaks and DS intensity in the Σ line is remarkable, the sharp drop in DS intensity around $\xi = 0.4$ is replicated by the much lower intensity of the QE peak at $\xi = 0.5$. The link between the quasi-elastic component of the IXS spectra and the diffuse scattering features is strengthened by looking at the widths of the QE peaks, as shown in panel b of figure 5.7. Data from the Σ line and from the secondary bank of detectors both show a sharp broadening of the QE peaks at the commensurate modulation wavevector $\mathbf{q}_{CO}$. Like with the softening data (figure 5.7 a), the outliers at the extremities might be related to the approach of $\mathbf{q}_{CO}$ under a different reciprocal lattice vector $\mathbf{G}_{hk0}$ and to the fact the detector get less accurate as they go further than the main one.

Given the correlation between QE peaks and the DS features, the sudden rise in width of the QE peaks can be attributed to a shortening in the lifetime of the short-range

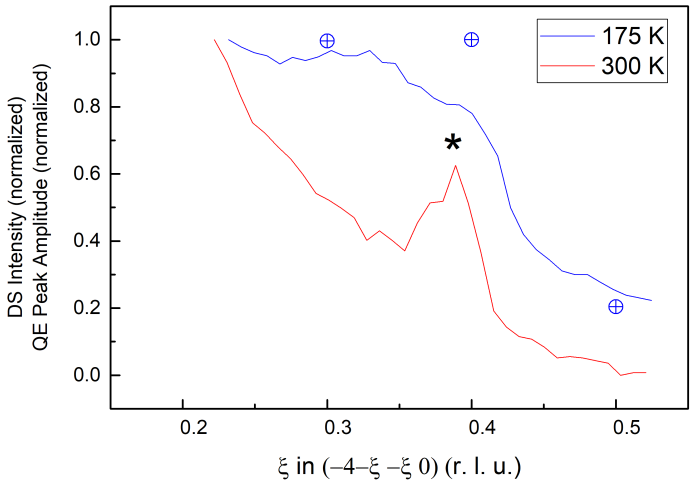

Figure 5.9 – Normalized diffuse scattering intensity (solid lines) and normalized amplitude of quasi-elastic peak in the (-1 -1 0) direction (crossed circles). Asterisk indicates the polycrystalline contribution to the diffraction pattern, which appears as the characteristic ring in the diffraction patterns of figure 5.3.

correlations shown by diffuse scattering. This indicates a competition between two distinct distortions with wavevector $\mathbf{q}_{DS} = \left(\frac{1}{3}, \frac{1}{3}, 0\right)$ and $\mathbf{q}_{CO} = \left(\frac{1}{2}, \frac{1}{2}, 0\right)$. As shown by DS data, the distortion with $\mathbf{q}_{DS}$ starts at higher temperatures, but the shortening of their lifetimes at $\mathbf{q}_{CO}$ shows that this latter distortion quickly overcomes the former and causes the transition into the monoclinic phase.

5.4 Raman Spectroscopy

Raman Spectroscopy is a powerful technique to probe lattice vibrations in a material. Considering that multiferroicity in a material necessarily involves robust spin-lattice coupling, multiferroicity in $NaMN_7O_{12}$ should imply anomalies in the phonon spectra according to the established magnetic order. To probe changes is phonon behavior with magnetic order and field, Raman spectroscopy were performed at Institut de minéralogie, de physique des matériaux et de cosmochimie (IMPMC), using a$NaMN_7O_{12}$ single crystals using a T64000 Jobin Yvon spectrometer with a 514 nm wavelength. A liquid Helium cryostat was used to control the temperature between 15 to 250 K. The reduced size of the crystal (usually in the tens on μm) makes the positioning of the laser spot difficult, and thermal dilation of the sample holder hinders a consistent positioning of the spot in the sample, which leads to great variation in Raman intensity through the temperature range. The obtained spectra are displayed in figure 5.10.

The first noticeable feature in the spectra set are the peaks that split in the monoclinic phase. Most clear among those are the large peak centered at 520 cm^{-1}, that

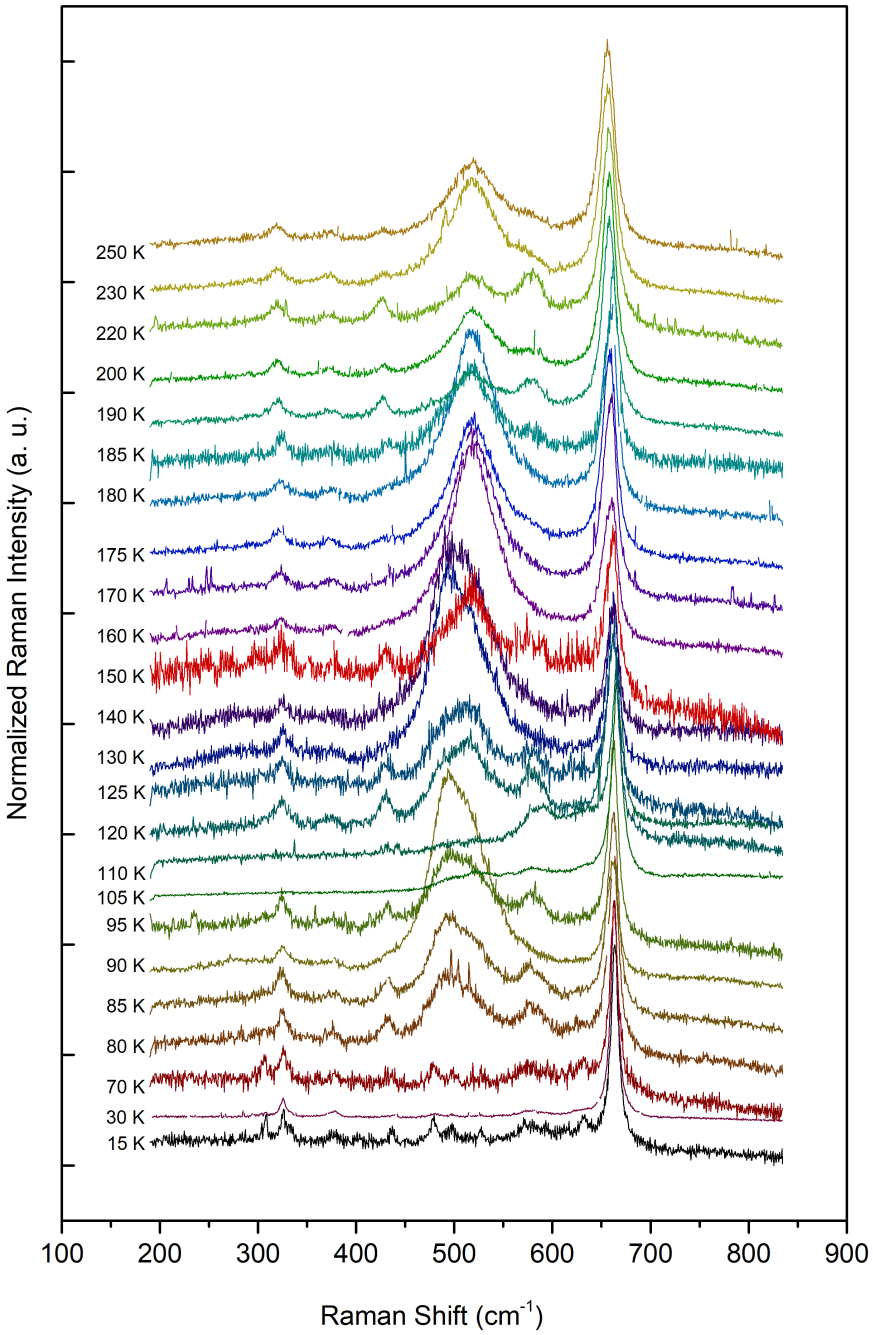

Figure 5.10 – Temperature evolution of normalized Raman spectra for a $NaMn_7O_{12}$ single crystal sample. Spectra are shifted for clarity.

despite an intensity that varies much with temperature can be clearly resolved in two peaks under 175 K, and the peaks around 300 cm^{-1}, that can be resolved at the lowest temperatures, but are definitely merged in the cubic phase. Additionally, the largest variation in intensity of the large peak at 520 cm^{-1} are around the transition temperatures, including the magnetic ones.

The peaks at 520 cm^{-1} and 660 cm^{-1} are the ones that show more significant

shifts in frequency, especially in the monoclinic phase. The evolution of their positions and widths is shown in figure 5.11. The similarity in the behavior of the widths is striking, both peaks widen at the magnetic transitions at $T_{N,A'} = 92$ K and $T_{N,B} = 125$ K and slightly narrows just above $T_{CO} = 176$ K. The peak positions behave differently, but both peak positions show either a discontinuity (both panels at $T_{N,A'}$ and panel a at $T_{N,B}$) or a local maximum (panel a at T_{CO} and panel b at $T_{N,B}$). It is also remarkable that the peak at 660 cm^{-1} is at significantly higher shifts in the phase where only the B-site Mn ions are magnetically ordered (between 92 and 125 K).

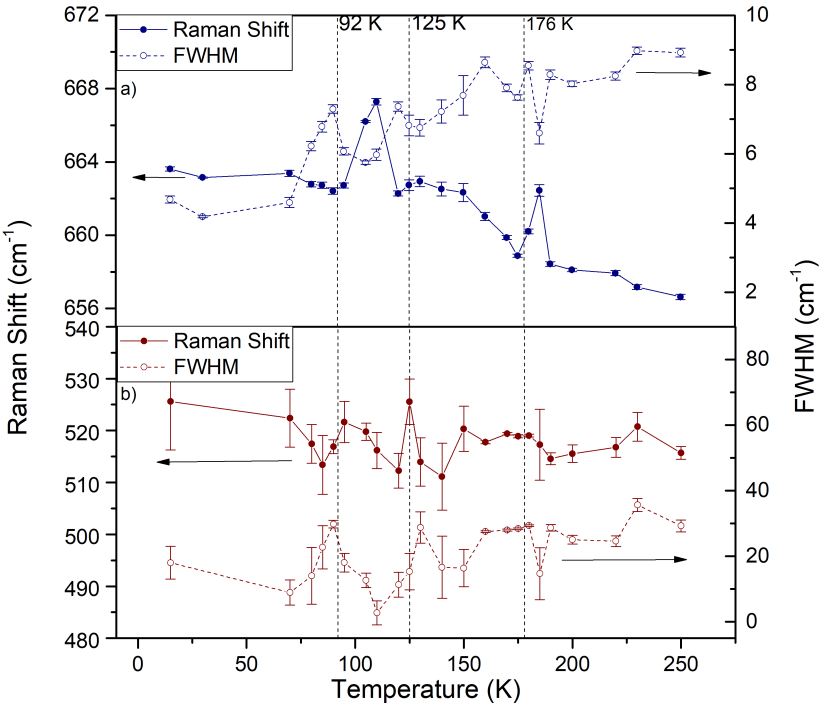

Figure 5.11 – Temperature evolution of position and full width at half maxima (FWHM), of the $NaMn_7O_{12}$ Raman peaks centered around 660 cm^{-1} and 520 cm^{-1}

It is important to remark that there is no evidence of large structural anomalies in previous work [77]. Figure 5.2 show that the lattice parameters and interatomic distances are well behaved in all the monoclinic phase. This evidences that the anomalies detected in the Raman spectra during the magnetic transition are due to spin-lattice coupling. Particularly, since we see broadening of peaks in both transitions for both studied modes, we see a shortening in phonon lifetimes upon changes in magnetic order.

To further study the interplay of lattice and magnetic degrees of freedom, Raman spectroscopy was also performed under magnetic fields, at the Institut des NanoSciences de Paris (INSP), in this experiment a wavelength of 454 nm. A Helium cryostat was used to cool both the sample and the superconducting magnet, but constrained the measurements to the temperature of 2 K, while magnetic fields of up to 9 T. The same kind of difficulty

regarding positioning of the laser spot was found in this experiment, but the influence of the magnetic field can still be seen in figure 5.12.

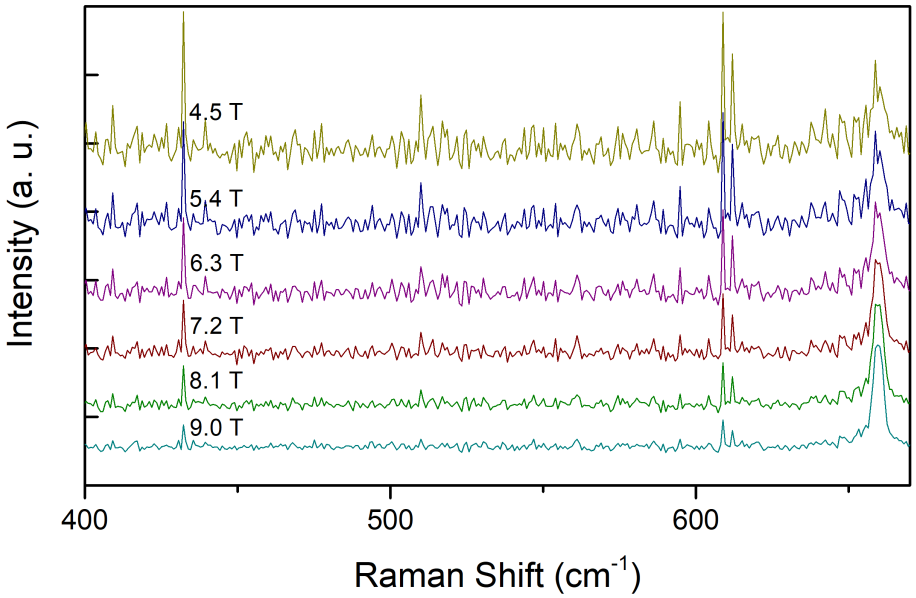

Figure 5.12 – Raman spectra taken at 2 K under different magnetic fields. Note the increase in the intensity of the 660 cm^{-1} peak opposed by the decrease of the 520 cm^{-1} one.

Many of the peaks seen in previous experiment can be seen in figure 5.12, all presenting very small widths due the much lower temperature. The magnetic field showed an opposing effect in the different peaks of figure 5.12. While the enhancement of the intensity is very clear in the 660 cm^{-1} peak, the magnetic field seems to have an opposing effect on the ones at 420 cm^{-1} and 520 cm^{-1}, this last one being barely visible at the higher fields. This shows that the presence of a magnetic fields can alter the scattering intensity of these phonons, further evidencing the presence of coupling between lattice and magnetic degrees of freedom in $NaMn_7O_{12}$, which is a possible driving force to magnetically driven ferroelectricity.

5.5 Specific Heat

Another powerful technique to detect coupling between elastic and magnetic properties is to perform specific heat measurements under magnetic fields. It can not only indirectly detect changes in the phonon behavior describe in the previous section, but also inform about phase transition and how they behave under magnetic fields.

The constant pressure specific heat (hereafter referred to simply as specific heat, for simplicity) measurements were made in IMPMC by Prof. Yannick Klein using a Quantum

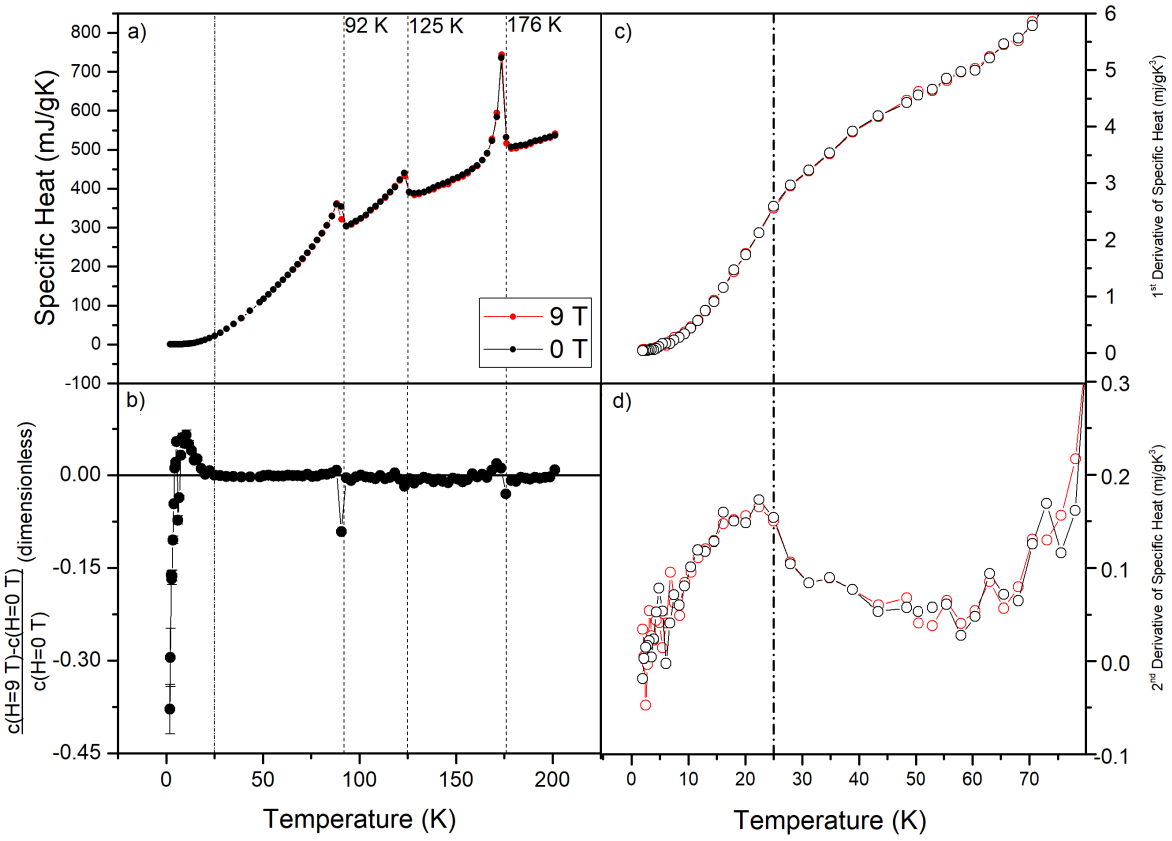

Figure 5.13 – a) Specific heat of a $NaMn_7O_{12}$ polycrystalline sample as a function of temperature, dashed lines at the discussed transition temperatures. Dash and dot line at the anomaly emphasized in panels b-d. b) Relative difference between specific heat under a 9 T and zero magnetic field. Right panels: First (c) and second (d) derivatives of specific heat, indicating a second order phase transition by the dash and dot line.

Design PPMS system, under magnetic fields of up to 9 T. The results are displayed in figure 5.13, panel a offers a general picture: the two magnetic and one structural/charge-ordering transitions can be clearly identified. The relative difference between the sample's specific heat under 9 T and zero magnetic field is shown in panel b, it is noteworthy that the difference is only appreciable in temperatures under 25 K and, in a much more limited range, close to the magnetic transitions. Panels c and d show an anomaly at the first and second derivatives of specific heat at that same temperature, which evidences a higher-order transition to a phase with enhanced spin-lattice interaction.

The relation between specific heat and magnetic field is further analyzed in figure 5.14. Panel a shows clearly the split between the 9 T and no field curves at low temperatures and panel b emphasized that the variation of specific heat with field reaches 40% at low temperatures, it has no influence whatsoever at higher temperatures. To investigate the reasons behind the coupling between specific heat and magnetic field, a Debye model fit

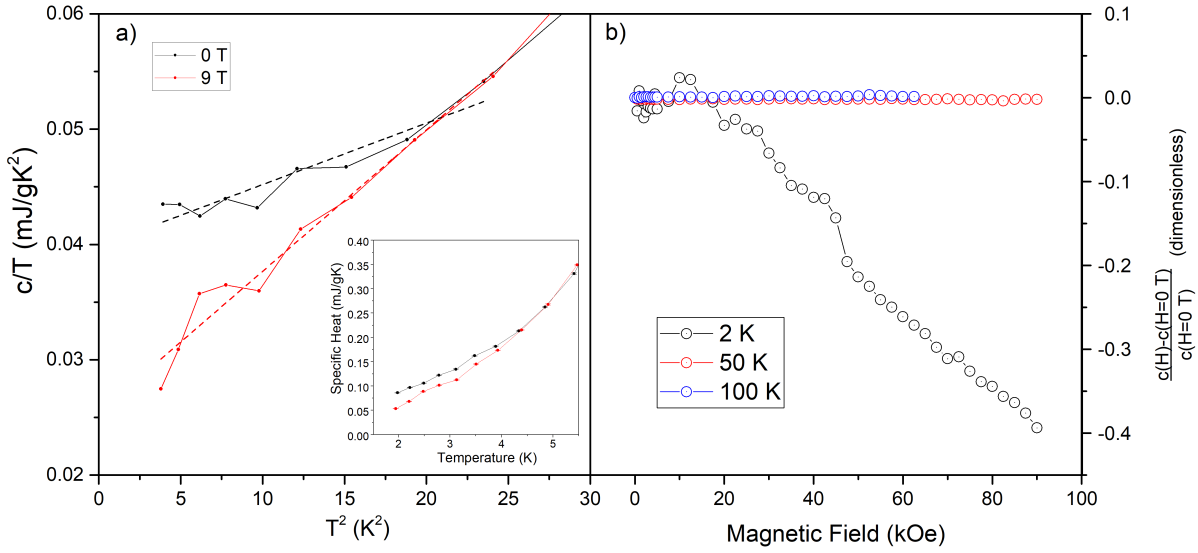

Figure 5.14 – a) $c/T \times T^2$ and Debye model fit with results in table 5.2. Inset shows zoom at low temperatures emphasizing the difference between specific heat with and without magnetic field. b) Relative difference in specific heat with respect to magnetic field at different temperatures.

was performed to get an estimation of electronic and phonon contribution to specific heat. The fittings can be seen in the inset of figure 5.14 a and the results are shown in table 5.2.

Both parameters of the cubic law fitting suffer considerable change under the magnetic 9 T field. The near doubling of the electronic linear component β can be explained in terms of the smaller availability of electronic states under a high magnetic field. The more interesting change, however, comes with the phonon component, γ, which drops do about half its original value. This indicate a softening of the lattice in the low temperature region.

Such softening, together with the anomalies in the derivatives of specific heat, are both compatible with a continuous lattice deformation that happen in some improper ferroelectric materials [80], suggesting this system possesses robust coupling between lattice deformations and magnetic order in the form of a non-conventional ferroelectric transition.

Table 5.2 – Results of the Debye model fit shown in figure 5.14.

$c = \beta T + \gamma T^3$	0 T	9 T
γ $(10^{-2} mJ/gK^2)$	4.0 ± 0.1	2.5 ± 0.1
β $(10^{-4} mJ/gK^4)$	5.3 ± 0.7	12.3 ± 0.8

5.6 Magnetic Characterization

Magnetization measurements were performed at GMS in the Quantum Design MPMS3 SQUID-VSM both in a single crystal and in polycrystalline pellet. Most of the

features in the magnetic characterization match previously reported features [81], but a few details merit further discussion and analysis. The evolution of magnetization with temperature is displayed in figure 5.15. All the phase transition temperatures can be easily identified in all panels, the structural transition at $T_{CO} = 176$ K standing out from the antiferromagnetic ones ($T_{N,B} = 125$ K and $T_{N,A'} = 92$ K) by its characteristic discontinuity in the magnetization, contrasting to the typical cusp found in the other ones. The magnetic behavior of both samples in general agrees with what was previously reported [81].

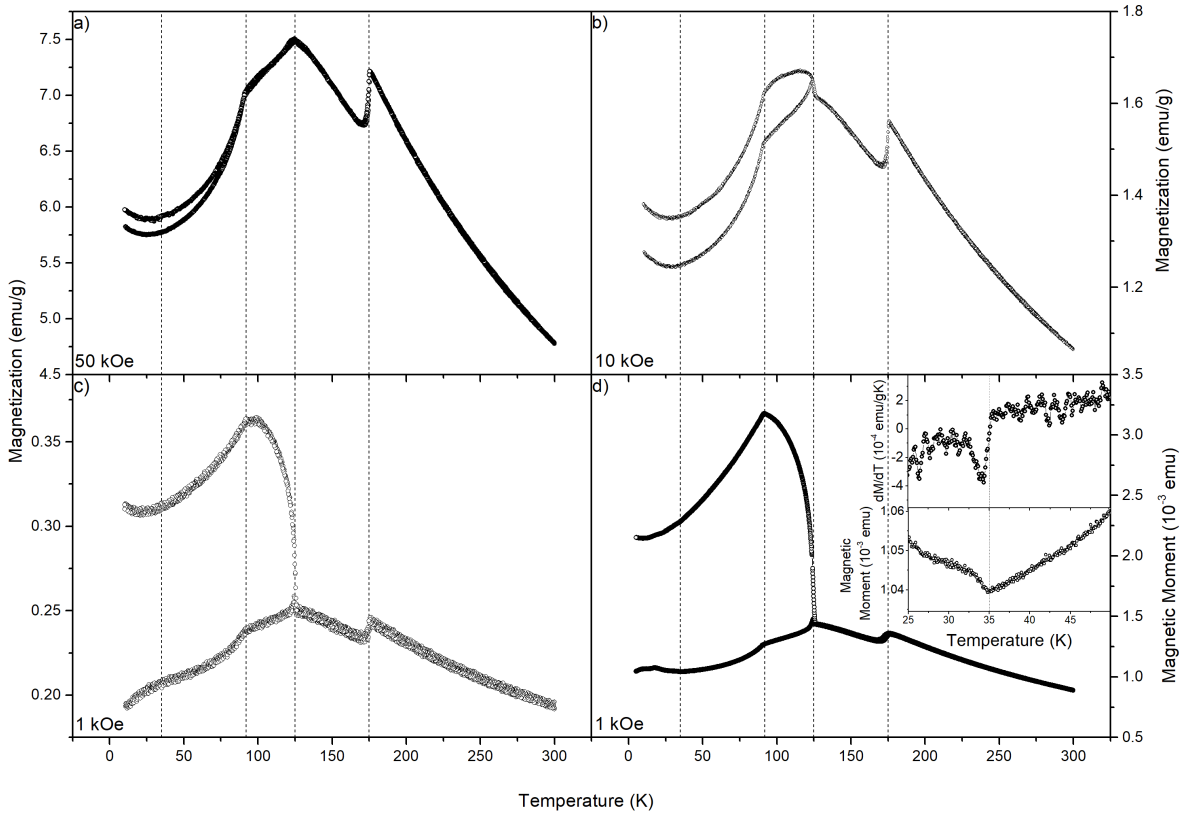

Figure 5.15 – Evolution of magnetization for a single crystal (a-c) and polycrystalline pellet (d) of $NaMn_7O_{12}$ under different magnetic fields. Dashed lines show transition temperatures described in text. Insets in panel d show the magnetization and its derivatives in region around 35 K.

One interesting feature in the MxT curves is the new magnetic transition at 35 K. This can be considered coincident with the transition detected in specific heat, since the change in the derivative of specific heat is smooth and broad. Although this transition can be seen more clearly in panel d of figure 5.15, it is also present in the characterization of the single crystal in panels a-c, where it appears as a local minimum in magnetization in panels and b, or as an inflection in panel c.

A set of hysteresis loops in a range of different temperatures is shown in figure 5.16. As expected from antiferromagnetically ordered phases, the applied fields are not enough to achieve magnetic saturation. The linear behavior observed around 2.5 kOe is kept in

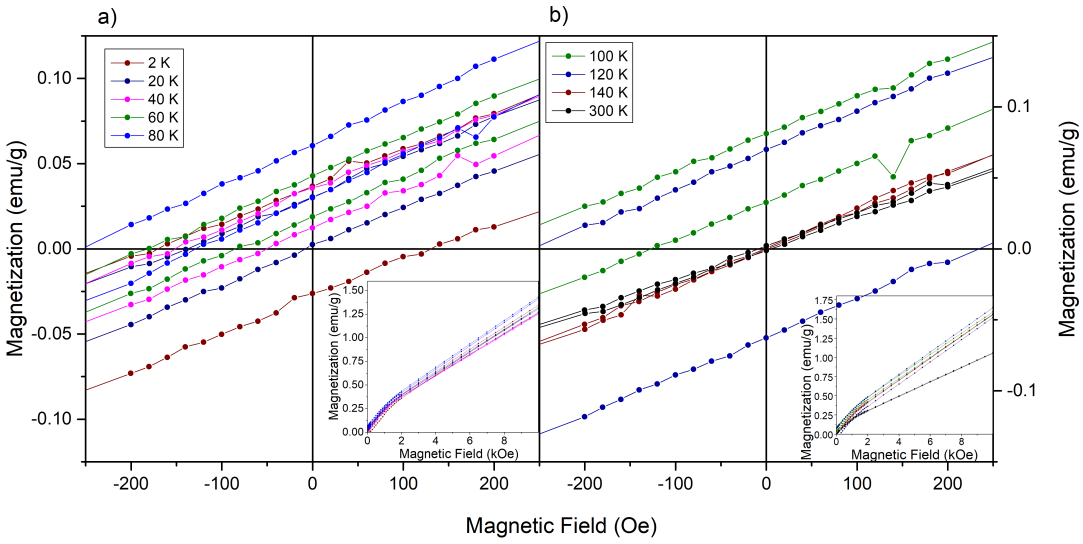

Figure 5.16 – Magnetic hysteresis loops of a single crystal of $NaMn_7O_{12}$ at lower (a) and higher (b) temperatures. Panels divided for clarity.

the whole range of applied fields, up to 70 kOe. The inset shows that the small hysteresis loops have a peculiar, exchange-bias like shift, which has been previously reported and attributed to the freezing of uncompensated spins in the antiferromagnetic lattice [81].

This phenomenon was further investigated by performing field-cooled hysteresis loops, *i. e.*, hysteresis loops measured after cooling the sample from room temperature

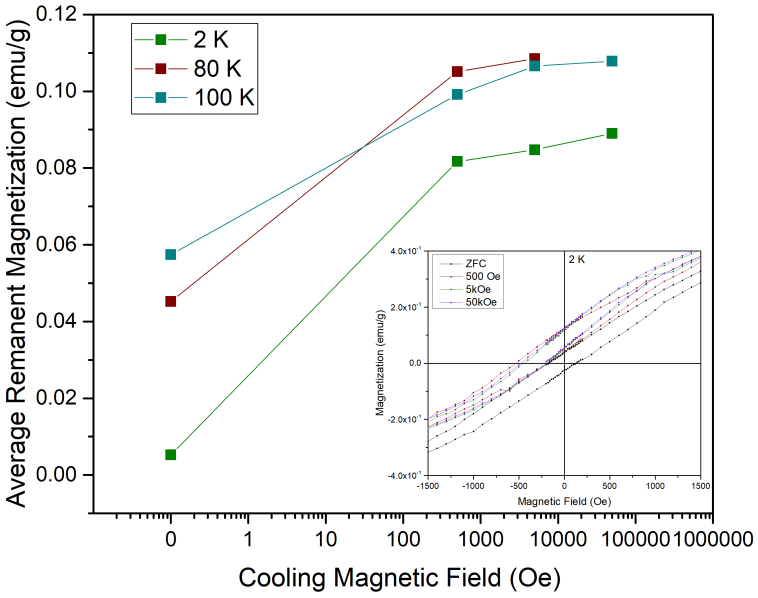

Figure 5.17 – Vertical center of hysteresis loops measured after cooling under magnetic field. Inset shows the hysteresis loops measured at 2 K.

under a magnetic field. This was done in order to freeze the uncompensated spins in a previously determined direction, showing that the shifts in hysteresis loops in figure 5.16 were not result of experimental error or trapped magnetic flux in the superconducting coils of the MPMS 3 magnet. The results can be seen in figure 5.17, which shows the vertical center of the hysteresis loops clearly responding to the cooling fields, and achieving a behavior close to saturation. The inset in figure 5.17 is also noteworthy, since it shows that the field cooled loops cross the vertical axis at two different positive values of magnetization. Similar behavior is seen for the horizontal center of the loops, as shown in the inset of figure 5.17. Additionally, because these measurements were performed in a single crystal, the possibility of exchange bias effects arising from intergranular boundaries can be discarded, and the uncompensated spins in the antiferromagnetic sublattices seem to be the suitable explanation for the hysteresis shifts.

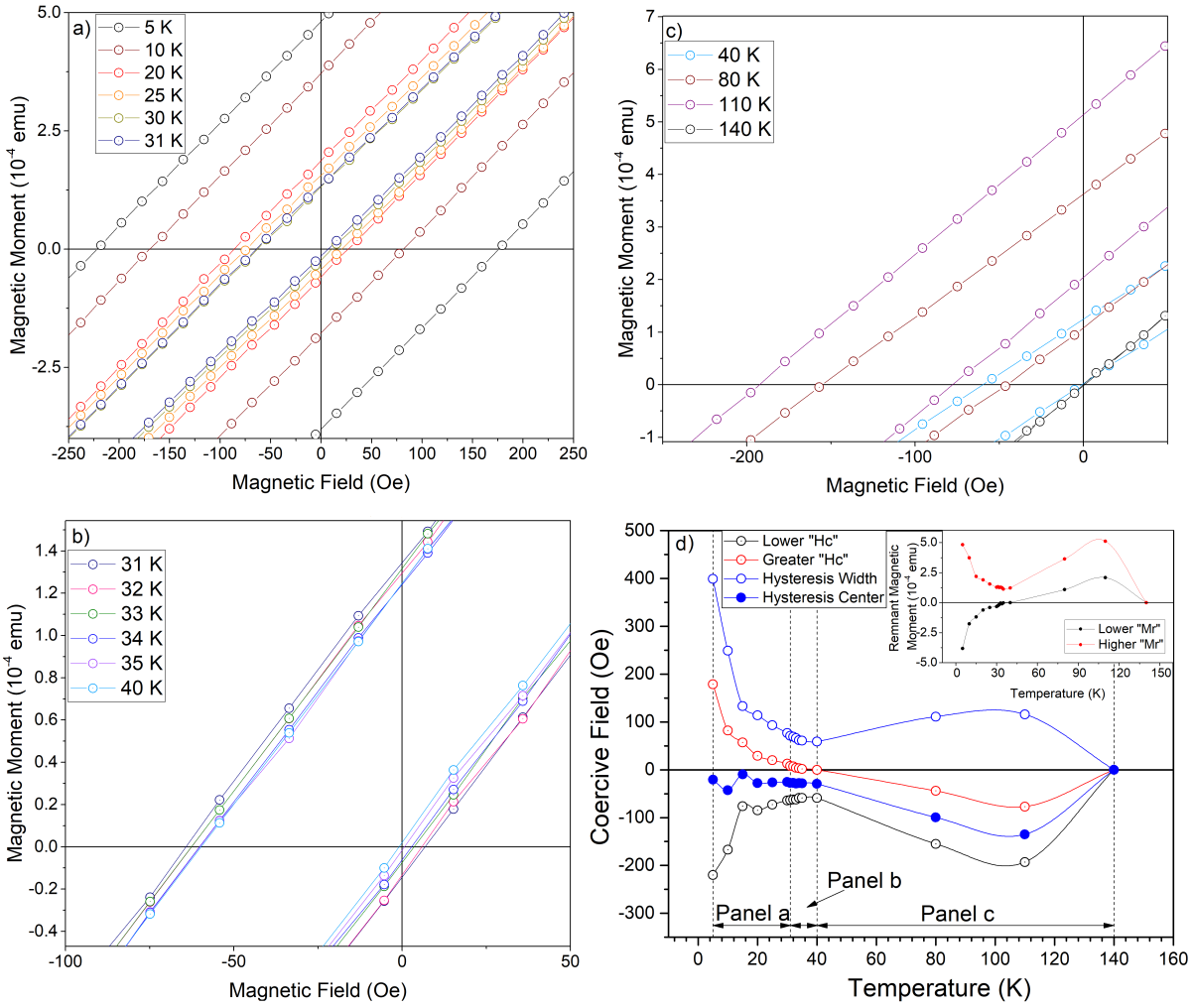

Figure 5.18 – Panels a-c: Low field zoom of magnetic hysteresis loops for a polycrystalline pellet of $NaMn_7O_{12}$. Panel d: Temperature evolution of the widths and centers of the hysteresis loops in the horizontal axis. Inset shows similar data for the vertical axis.

A more detailed analysis of magnetization versus field curves near the newly found transition revealed an interesting link between the shifts in the loops and this new transition. Figure 5.18 shows a very interesting pattern in the widths and shifts of the loop through the whole temperature range. By quenching the superconducting magnet before each loop and submitting a calibrated Palladium sample to the same protocol, we make sure the magnetic field is precisely determined, free from remnant fields due to trapped flux in the superconducting coils. In panel a, we can see the loops widths sharply dropping from the low temperatures of 2 K to the transition around 35 K. Panel details how the loops remain at a relatively constant width and position, restarting to widen and shift at around 40 K. And finally, in panel c, we see the loops widths largely grow and shift to the left, until their collapse after transitioning to the paramagnetic phase. Finally, panel d summarized the process, it is clear from it that the hysteresis widths go through a local minimum near the new transition. In a similar fashion, the hysteresis shifts are relatively small before the transition, but rise quickly after it.

Finally, we searched for direct magnetoelectric coupling by performing magnetization measurements under electric field in $NaMn_7O_{12}$, like also done with $LaMn_7O_{12}$. The sample began at 50 K for 30 minutes under an electric field 2.4 kV/cm, it was then cooled still under field to measurement temperature and one quadrant magnetization measurements were performed using the extraction method. Like with $LaMn_7O_{12}$, no direct coupling could be detected. The highest electric that could be applied (2.4 kV/cm) is relatively low compared to those used in typical ferroelectric characterization, and even magnetic field capabilities of the MPMS 3 are low compared to works that detect robust coupling [76], so the limitation in range of the fields might the reason behind the failure in detecting direct coupling.

5.7 Thermally Stimulated Current

The search for multiferroicity in $NaMn_7O_{12}$ can also be tackled by the ferroelectric side, so pyroelectric current measurements were performed in a polycrystalline pellet in order to detect ferroelectric ordering. The pyroelectric current measurements were performed using a Keithley 617 electrometer and the home adapted MPMS3 sample holder, at GSM. The 0.4 mm-thick sample pooling began by applying the 2.4 kV/cm electric field at 50 K for 10 minutes, the temperature was chosen to the highest in which the sample resistance was high enough so that the currents during pooling didn't exceed 5 μA. Similarly, the electric field was picked to be the highest possible under the sample holder limitation of 100 V_{DC}. It was then cooled still under field to 15 K, kept at this temperature for 30 minutes, released of the field and short circuited for 10 minutes, to release trapped intergranular charges. Finally, by heating the sample at a fixed rate, the temperature dependence of the current was measured, from which the electric polarization

was calculated. The sample would then be heated to room temperature so the experiment could be repeated in a different condition.

The main result is displayed in figure 5.19. A peak centered at $T_{Ferr} = 30$ K was found. The inversion of the signal at T_{Ferr} while other thermally stimulated currents conserve their polarity even under field inversion (Around 100 K in figure 5.19) constitutes strong evidence of a ferroelectric transition at this temperature instead of other kinds of thermally stimulated current caused by experimental artifacts, like spatially accumulated charges [75]. From the current profiles of figure 5.19 the electric polarization was calculated and represented in filled circles. The value polarization is on the order of $LaMn_7O_{12}$'s polarization under the same pooling fields, so polarization in the order of 1 $\mu C/cm^2$ under higher pooling fields and for single crystals is expected. Furthermore, the experiment was also performed at the rate of 3 K/min, which can be compared to other conditions in figure 5.20, where the 3:5 proportion between the different rates is kept with great precision.

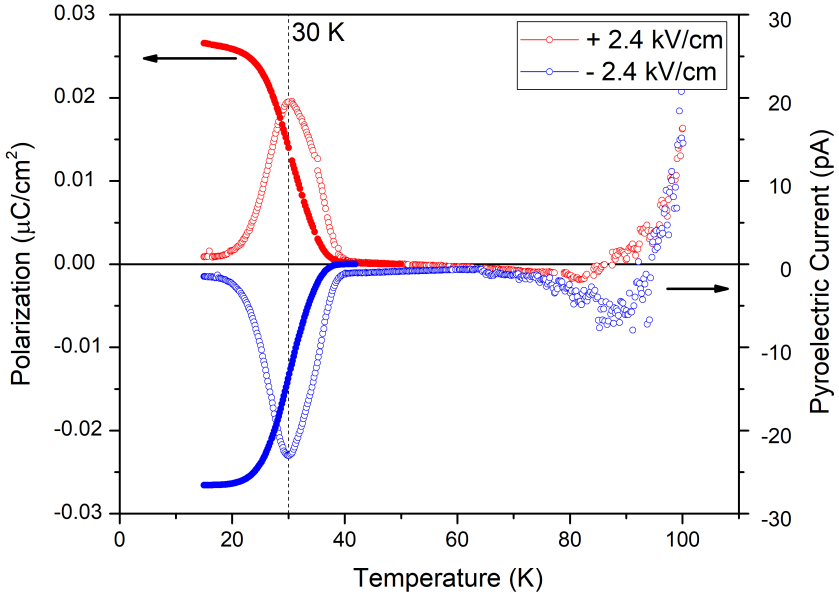

Figure 5.19 – Pyroelectric current profiles (open symbols, right axis) and remnant polarization (filled symbols, left axis) in function of temperature, measured at a 5 K/min rate. Dashed line shows the peak center at 30 K.

The peak at T_{Ferr} is quite wide, and this large transition sheds some light into the anomalies found in specific heat and magnetization. For instance, the difference in specific heat with and without magnetic field vanishes at the low temperature tail of the peak, where the polarization begins to drop. The anomaly in its derivatives is also located there. On the other hand, the anomaly in magnetization is located at the high temperature end of the peak, when most of the polarization is already gone. This strongly evidences that electric and magnetic orders are coupled under T_{Ferr}, and the coexistence of both ordered

phases in the same temperature range adds $NaMn_7O_{12}$ to the category of single phase multiferroic materials.

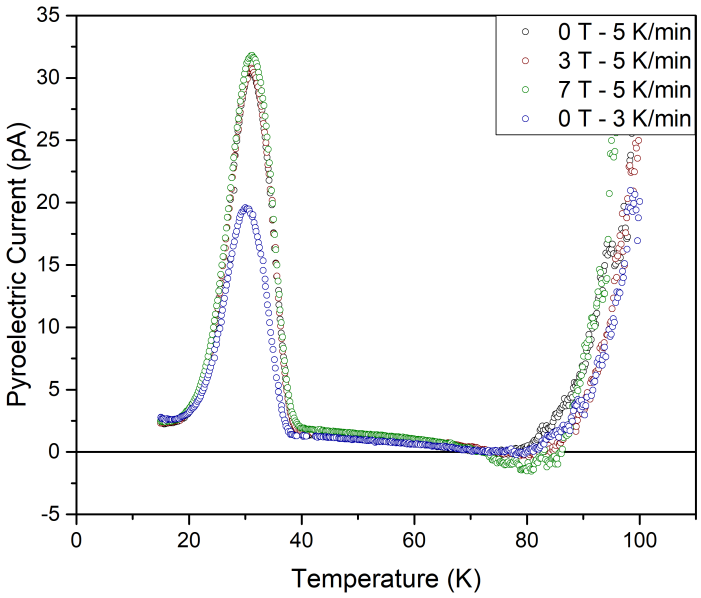

Figure 5.20 – Pyroelectric current peaks under different magnetic fields and heating rates. Note a precise 3:5 proportion between the measurements done with 3 and 5 K/min rates.

In order to detect coupling between the orders, figure 5.20 shows pyroelectric current measurements performed under different magnetic fields. Within the 7 T range of the MPMS 3 magnet, the magnetic field didn't have any effect over the ferroelectric peak, and consequently no effect on the polarization. Magnetoelectric susceptibility experiments were also performed, but still with negative results.

6 Discussion

6.1 Structural Anomalies in $\mathbf{NaMn_7O_{12}}$

Our data about structural characterization of the $NaMn_7O_{12}$ presents important differences with its bivalent counterpart $CaMn_7O_{12}$, as we observed by Diffuse Scattering and Inelastic X-ray Scattering. The interaction between the two structural anomalies found in $NaMn_7O_{12}$ shows how they compete and the fact that the soft phonon mode ultimately overcomes puts the Jahn-Teller mechanism in a very central position as the driving force of the commensurate distortion that takes place at T_{CO}.

An interesting aspect of the short-range correlations unveiled is their similarity to the ones found in $CaMn_7O_{12}$. DS data from [40] shows the same type of satellite peaks at temperatures significantly higher than the one when the incommensurate modulation effectively ensues (250 K), and higher yet than the one when the helical magnetic structure is established, with the same wavevector as the modulation (90 K). At this temperature, a ferroelectric order is also established, arising from the asymmetric exchange interaction (via the Dzyaloshinsky-Moriya interaction).

In $NaMn_7O_{12}$, on the other hand, that process is interrupted. While in $CaMn_7O_{12}$ the diffuse features appear already in the rhombohedral phase, in $NaMn_7O_{12}$ they appear in the cubic phase and by the transition to the monoclinic phase, the diffuse peaks disappear. The link to the dynamic origins of such disappearance come from the realization that the diffuse satellite peaks amplitudes are proportional to the amplitude of the quasi-elastic components of the elastic peak in the IXS experiments (see figure 5.9). Looking then to the width of said components (see figure 5.7 b), and noticing their broadening at $\mathbf{q}_{CO} = \left(\frac{1}{2}, \frac{1}{2}, 0\right)$, it can be seen that the lifetime of these short-range correlations is shortened by the softened phonon mode that leads to the structural modulation.

A closer look at the soft phonon, the influence of the Jahn-Teller mechanism in the structural anomaly becomes clear. Besides the symmetry analysis presented in section 5.3, the calculated distortion of the softened mode has a striking similarity to the structural modulation distortion, most importantly including two Jahn-Teller like elongation and compressions in two MnO_6 sharing the same crystallographic position. A possible driving mechanism for the structural modulation is through the freezing of this phonon as the JT distorted positions become energetically more favorable. And as it becomes more favorable the short-range correlations found in the DS experiments lose viability, which explains the broadening of the quasi-elastic component of the elastic peak, which indicate a shortening of the lifetime of the short-range correlations related to it.

This draws a scenario of competing distortions in the cubic structure of $NaMn_7O_{12}$. At higher temperatures, a three-unit cell sized distortion begins to ensue in the form of short-range correlations, like in the case of $CaMn_7O_{12}$, This distortion is made inviable tough, as Jahn-Teller phonon begins to soften, quickly becoming energetically more favorable and overcoming the incipient distortion. This highlights the importance of JT mechanism, as it is even able to suppress different kinds of distortion. The fact that the DS distortion begins to establish at higher temperatures while the IXS soft mode only appears in a short temperature range above T_{CO} also evidences how abruptly the JT soft mode is able to subdue competing distortions. The lack of anomalies in phonon energies and lifetimes at the diffuse scattering wavevector $\mathbf{q}_{DS}$ also supports the dominance of the JT mode over other distortions, but further experiments with more measurements in this region of the reciprocal space makes itself necessary. The competition between different competing structural distortions, and the dominant role played by the JT mechanism in $NaMn_7O_{12}$ might shed light into more complex structures with similar phenomena, like magnetite.

An important future perspective regards a more precise study of the short-range correlation found in the diffuse scattering experiment. One possibility for these phenomena are polarons, which would bring interesting insight into the electron-phonon coupling it would imply, and how it would relate to the multiferroicity that was newly found in $NaMn_7O_{12}$ at lower temperatures. A more interesting possibility is a distortion similar to $CaMn_7O_{12}$. This distortion is highly asymmetrical, being the cause of the helical magnetic order and multiferroicity via the Dzyaloshinsky-Moriya Interaction mechanism [40]. If a similar distortion in suppressed in $NaMn_7O_{12}$ and a different, simpler and less asymmetrical distortion is established, this makes other mechanisms for multiferroicity, like symmetric exchange, a much more likely candidate to explain the multiferroic behavior of $NaMn_7O_{12}$. EXAFS experiments might be able to probe into those questions and further the understanding of this short-range order.

6.2 New Multiferroic Phase in $\mathbf{NaMn_7O_{12}}$

The finding of a ferroelectric transition in the established antiferromagnetically ordered phase places $NaMn_7O_{12}$ in the class of multiferroic materials. Since this transition is simultaneous to magnetic transition which is related to a very peculiar behavior of magnetic hysteresis, there is a strong possibility of a causal link between these phenomena, and consequently robust coupling between the ferroic orders. The effects of magnetic field over specific heat are also only present in the ferroelectric phase (see figure 5.13 b). As soon as the electric polarization begins to drop the difference between specific heat with and without magnetic field completely vanishes and remains completely absent above T_{Ferr}. Besides from the difference specific heat happening only on the ferroelectric phase,

the Debye model fitting results also supports the picture of magnetoelastic coupling. The large increase in the lattice related β parameter agrees with the expected softening of phonons in the ferroelectric transition, since the higher availability of low energy phonons tends to increase specific heat at a given temperature. The presence of this effect under magnetic field evidences the coupling between the ferroic orders. Still, evidence of direct magnetoelectric coupling remains elusive.

The very small change in magnetization in the new magnetic phase suggest a different antiferromagnetic ordering in either the A' or B sites ensue at this temperature. Nevertheless, the neutron diffraction data doesn't show any signs of such order [77, 81], which suggest that this magnetic feature might have an origin different from the magnetic sublattices. This is backed by specific heat data, while the other magnetic and structural transitions are very sharply marked by discontinuities, the ferroelectric transition at 34 K is only noticed through its first and second derivatives (see figure 5.13). This behavior of specific heat has been detected in other improper ferroelectrics [80].

A model that can explain these magnetic anomalies in the absence of new magnetic ordering is based on the expected ordering of the domain borders in an magnetoelectric antiferromagnet [58]. Such ordering could explain the change in magnet properties below the ferroelectric transition even in the absence of new magnetic ordering. The domain ordered phase is in agreement with the large widening in hysteresis loops found below T_{Ferr}. Above this temperature, hysteresis loops are thinner and shift intensely in an exchange bias fashion, a behavior that has been previously attributed to uncompensated moments in the antiferromagnetic lattices [81] (see figure 5.18 for the evolution of hysteresis loops). It is important to remark that these effects are of intrinsic nature and are seen even in single crystals (see figure 5.17), so extrinsic and intergranular exchange-bias effects are not suitable as an explanation. Being present in a single $NaMn_7O_{12}$ crystal, these effects must arise from interaction between AFM domains.

Finally, pyroelectric current, specific heat and magnetic measurements evidence the multiferroic character of the phase transition at $T_{Ferr} = 34$ K in $NaMn_7O_{12}$. The presence of the ferroelectric transition and anomalies in specific heat at this temperature elucidate the magnetic features that were present despite of the lack of evidence of new magnetic order. The exchange bias-like shift of hysteresis loops and the higher coercive fields in the ferroelectric phase can be explained in terms of the magnetoelectricly induced antiferromagnetic domain borders, adding to the evidence of magnetoelectric coupling in $NaMn_7O_{12}$. The evidence of magnetoelastic coupling from the specific heat measurements and the lack of new neutron diffraction peaks at this temperature despite the anomalous magnetic features [77] point to the ordering of antiferromagnetic domain boundaries driven by improper ferroelectricity as the coupling mechanism between electric and magnetic degrees of freedom in $NaMn_7O_{12}$. However, to verify the direct coupling

and the magnetization flipping possibilities that such domain ordering would provide, experiments allowing for a higher range of electric and magnetic fields would be necessary [76].

6.3 Comparing the Multiferroicity in $\mathbf{NaMn_7O_{12}}$ and $\mathbf{LaMn_7O_{12}}$

There were several reasons to expect magnetically induced ferroelectricity in the quadruple perovskite manganites $NaMn_7O_{12}$ and $LaMn_7O_{12}$. Not only the same structure compound $CaMn_7O_{12}$ has shown very high electric polarization via the DMI mechanism [34, 35] but it has also large symmetric exchange striction driven ferroelectricity has been predicted in $RMnO_3$ perovskites, where R is a rare earth metal [28]. The similarity with simple perovskites structures but with usually simpler distortions make the study of the quadruple perovskite structures very interesting. Moreover, the higher symmetry of quadruple perovskite with regards to the simple ones lead to more symmetrical crystallographic oxygen positions, with makes them nearly completely defect free and reduces oxygen mobility to screen possible electric moments that might appear in the structure.

As expected, both $NaMn_7O_{12}$ and $LaMn_7O_{12}$ have been found to be multiferroic. But regardless of the similarities in their structure, the phenomenon of multiferroicity

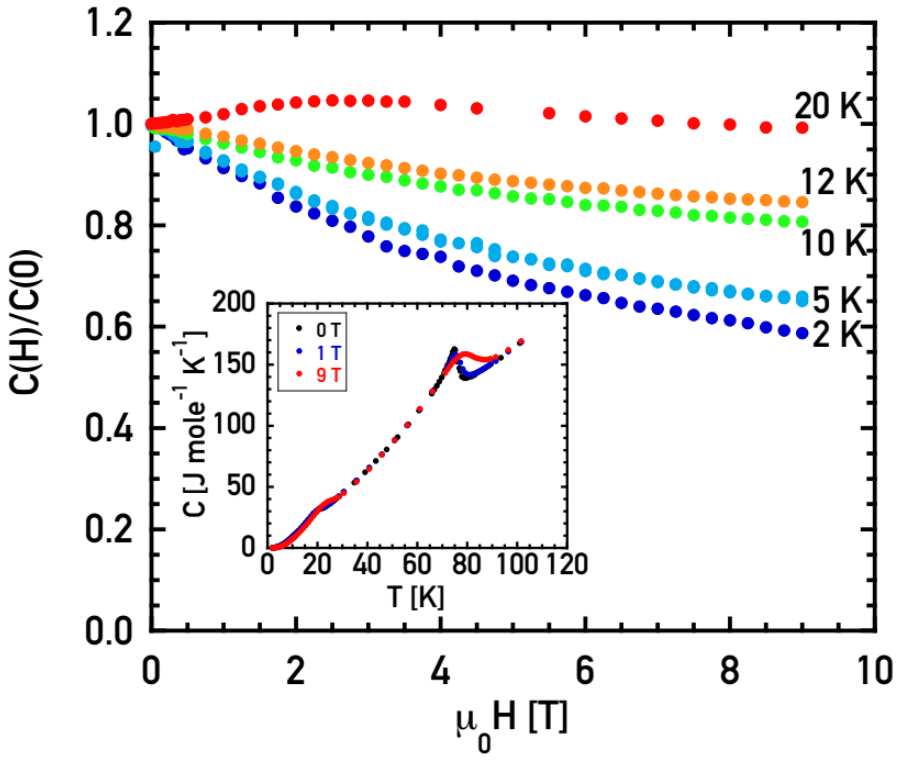

Figure 6.1 – Magnetic field dependence of $LaMn_7O_{12}$ in different temperatures. Inset shows temperature dependence of specific heat for different magnetic fields. Adapted from [42].

appears in very different ways in these related systems. While the ferroelectric transition in $LaMn_7O_{12}$ is coincident to one of the known magnetic phase transitions (specifically, $T_{N,B}$), with clear signatures in magnetization and specific heat (see figures 5.13, 5.14 and 6.1 for a comparison), the ferroelectricity in $NaMn_7O_{12}$ appears at a completely new phase, with a broad signature over the derivatives of the specific heat. Moreover, if the picture of the AFM domain border ordering is confirmed, beyond being caused by magnetic ordering, the ferroelectricity gives origin to distinct magnetic phenomena.

Comparing the magnetic field dependence of specific heat in $NaMn_7O_{12}$ and $LaMn_7O_{12}$, one can see a very similar dependence. Even the temperature in which $LaMn_7O_{12}$'s specific heat grows with magnetic field finds parallel in figure 5.13 c. This seems to suggest that the magnetoelastic coupling that causes the ferroelectricity is similar in both systems. However, there are important differences in their specific heat behavior during the phase transitions. As seen in the inset of figure 6.1, the phase transitions in $LaMn_7O_{12}$ are smeared by the magnetic field, a phenomenon that is not observed in $NaMn_7O_{12}$ (see figure 5.13 a). It would seem that the magnetoelastic coupling that leads to ferroelectricity in $LaMn_7O_{12}$ is absent in $NaMn_7O_{12}$ at temperatures much higher than T_{Ferr}. However, the effects observed in Raman spectroscopy point in a different direction. The shifts in Raman peaks during the magnetic transitions are of similar magnitude, this can be seen by comparing figure 6.2 and 5.11, which indicates that the magnetoelastic coupling is present at $NaMn_7O_{12}$ at temperature much higher than T_{Ferr}. The possibility that is left is that in $NaMn_7O_{12}$, despite the existence of magnetoelastic coupling at higher temperature, it is not of sufficient magnitude to cause ferroelectric order. This is surprising because, once the order is established, the polarization is of similar magnitude to $LaMn_7O_{12}$.

Another interesting question is, if the magnetic anomalies found in $NaMn_7O_{12}$ at T_{Ferr} are caused by magnetoelectrically coupled domain boundaries, why a similar phenomenon is not found in $LaMn_7O_{12}$. A closer look into the difference in their magnetization might provide some insight into the reasons. As seen in figures 4.3, 4.4, 5.15 and 5.16 the weak ferromagnetic component in $LaMn_7O_{12}$ is larger, and its hysteresis loops are much slimmer than $NaMn_7O_{12}$. In a such scenario, the much larger bulk weak ferromagnetic components might dominate over the domain magnetization. On the other hand, the larger hysteresis loops of $NaMn_7O_{12}$ and smaller weak FM component (see figure 5.15 and 5.16) would indicate a picture of domain dominance over bulk. Finally, if like in $CaMn_7O_{12}$ the diffuse scattering corresponding distortion is highly favorable to asymmetric exchange interaction, it would explain the weaker weak FM component of $NaMn_7O_{12}$ magnetization. However, further experiments on the DS future are necessary to reveal the nature of this distortion.

Considering the most colinear spin structure of $LaMn_7O_{12}$ and $NaMn_7O_{12}$ and

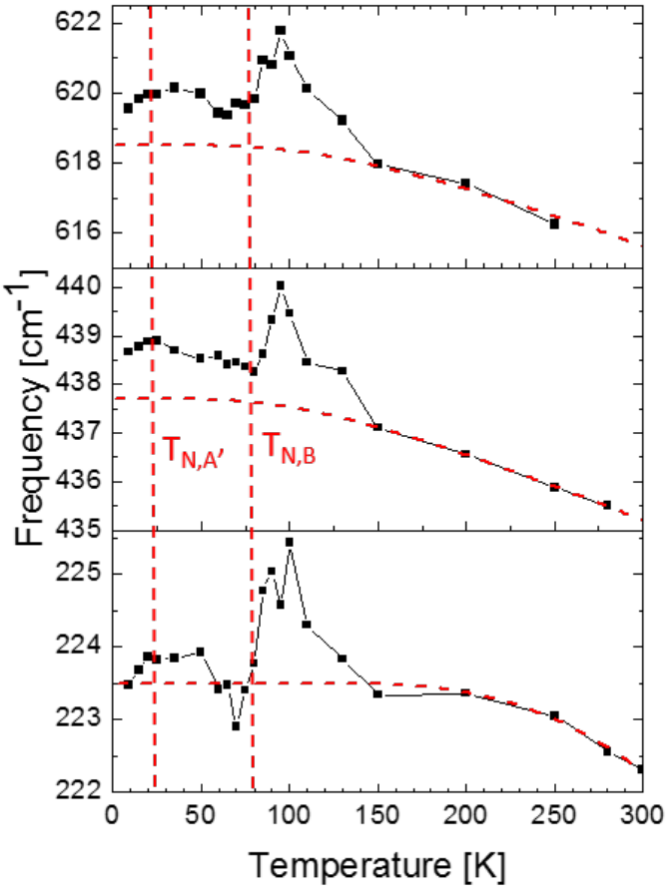

Figure 6.2 – Temperature evolution of the main Raman peaks for $LaMn_7O_{12}$. Magnetic phase transitions shown by red vertical dashed lines. Adapted from [82].

the high values of polarization achieved, suggest that the symmetric exchange is the mechanism of magnetic ordering induced ferroelectricity in these quadruple perovskite manganites. According to that model, the polarization should lie in the *ac* plane for both compounds, but experiments with single crystals are necessary to confirm that claim. Because of the asymmetric exchange induced weak ferromagnetism in these compounds, a small component of the polarization is also expected through this mechanism. But, as seen in the case of $CaMn_7O_{12}$ [34, 35], this component is sensitive to magnetic fields, given the easily switchable nature of this ferromagnetic component. Since the electric polarization in $LaMn_7O_{12}$ and $NaMn_7O_{12}$ was found to be insensitive to our range of magnetic fields, this also evidence the prevalence of the symmetric exchange mechanism, which is based on the hard to switch antiferromagnetic ordering.

Another interesting observation regards the apparent incompatibility between the centrosymmetric space group $I2/m$ and the obligatory non-centrosymmetric distortion that are associated with ferroelectricity. These distortions are of elusive detection in magnetic multiferroics, but case of the simple perovskite $TbMnO_3$ provides interesting insight into the difficulties involved in their detection. As described in [27], the atomic distortions are

in the scale of femtometers, which added to the possibility of nanometer sized ferroelectric domains show that these distortions are not detectable by used the X-ray techniques. This removes the apparent incongruity regarding the centrosymmetric point group and adds the interesting possibility of performing local structure sensitive techniques, like EXAFS, to also probe for this kind of distortion.

Therefore, even though direct coupling evidence remains unfound, there is substantial evidence to claim that the quadruple perovskite manganites $LaMn_7O_{12}$ and $NaMn_7O_{12}$ present magnetic ordering induced ferroelectricity by means of the symmetric exchange striction model, adding to the category of single phase multiferroic materials.

7 Conclusion and Future Perspectives

In this work, using different experimental techniques, we were able to unveil multiferroicity in the quadruple perovskite manganites $(LaMn_3)Mn_4O_{12}$ and $(NaMn_3^{3+})(Mn_2^{3+}Mn_2^{4+})O_{12}$. Furthermore, through synchrotron techniques, we determine the driving forces that cause the higher temperature structural instabilities in $NaMn_7O_{12}$.

Combining data of Diffuse X-ray scattering and Inelastic X-ray scattering, we were able to determine the crucial role played by the Jahn-Teller mechanism in the structural distortion that takes place in $NaMn_7O_{12}$ at T_{CO}. By means of a soft phonon mode that excite Jahn-Teller distortion, the higher temperature short range distortions are suppressed, disappearing in a very short temperature range, giving place to the commensurate modulation found in the monoclinic phase [78]. If the similarities with the bivalent quadruple perovskite manganite $CaMn_7O_{12}$ can be extrapolated, this plays an important role in suppressing the asymmetric exchange striction component of magnetic ordering induced ferroelectricity that is found at lower temperatures. But in order to clarify that claim, local structure sensitive techniques, like EXAFS, must be applied in order to determine the nature of the short-range correlations.

Several lattice related experiments evidenced the possibility of magnetoelastic coupling in these quadruple perovskite manganites. Anomalies in Raman spectra of similar magnitude were found for certain peaks both in $NaMn_7O_{12}$ and $LaMn_7O_{12}$ during the magnetic ordering temperatures of both A' and B sites. Moreover, interesting effects of the magnetic field over Raman intensities were found in $NaMn_7O_{12}$, adding to the case of magnetoelastic coupling. Specific heat measurements, however, have unveiled important differences in the behavior of the two systems. While in $LaMn_7O_{12}$ important differences in specific heat under magnetic fields are found up to $T_{N,B}$, $NaMn_7O_{12}$ only show such effects in temperatures much lower than $T_{N,A'}$, and also showing signs of a phase transition in the magnetoelastic coupled phase. In both cases, the effects of magnetic fields over specific heat are exclusively found in a temperature range where electric ordering is also present.

Pyroelectric current measurements were the primary evidence for ferroelectric ordering in $NaMn_7O_{12}$ and $LaMn_7O_{12}$, which transition into an ordered state at the same temperature in which magnetoelastic coupling ensues. The magnitude of the electric polarization in $LaMn_7O_{12}$, which orders electrically at $T_{N,B}$, is very high, setting even greater expectations to its values in single crystals. As for $NaMn_7O_{12}$, which orders at $T_{Ferr} = 30$ K, the electric polarization seems to be as large as $LaMn_7O_{12}$'s, and the transition is accompanied by a widening of hysteresis loops. This property, in the absence

of neutron diffraction evidence on new magnetic ordering, has been attributed to domain wall ordering in the AFM lattice, an effect that is driven by magnetoelectric coupling.

The magnetic structure provides valuable information to unveil the mechanism through which the multiferroicity is established. Both $NaMn_7O_{12}$ and $LaMn_7O_{12}$ presenting only colinear magnetic structure, with a small asymmetric exchange induced canting, there is ground to assume that the polarization has both a symmetric (proportional to $|\mathbf{s}_i \cdot \mathbf{s}_j|$) and asymmetric (proportional to $|\mathbf{s}_i \times \mathbf{s}_j|$) exchange. However, the higher predicted magnitudes [28] and the lack of effect of magnetic field over polarization point to a dominance of the symmetry exchange model, since the asymmetric weak ferromagnetic component of the magnetization is very susceptible to the field, as shown by the example of $CaMn_7O_{12}$ [34, 35].

This conclusion predicts the electric polarization to lie in the *ac* plane, which remains to be confirmed in future work and would require larger crystals. Larger crystals would also allow direction specific magnetic characterization, which would cast light into the direction dependence of specific magnetic features and the domain structure of the antiferromagnetic lattice. On the structural property side, local structure sensitive measurements, like EXAFS, could clarify the nature of the diffuse features observed above T_{CO} in $NaMn_7O_{12}$ and detect the minute asymmetric distortions expected in the ferroelectric phase.

We conclude that both the quadruple perovskite manganites $(LaMn_3)Mn_4O_{12}$ and $(NaMn_3^{3+})(Mn_2^{3+}Mn_2^{4+})O_{12}$ present magnetic order induced ferroelectricity, driven by symmetric exchange striction.

Bibliography

1 SPALDIN, N. A.; FIEBIG, M. The renaissance of magnetoelectric multiferroics. *Science*, v. 309, p. 391, 2005. Citado 4 vezes nas páginas 14, 24, 25, and 26.

2 EERENSTEIN, W.; MATHUR, N. D.; SCOTT, J. F. Multiferroic and magnetoelectric materials. *Nature*, v. 442, n. 17, p. 759, 2006. Citado 6 vezes nas páginas 14, 25, 26, 32, 33, and 34.

3 FIEBIG, M. Revival of the magnetoelectric effect. *Journal of Physics D: Applied Physics*, v. 38, p. R123–R152, 2005. Citado 3 vezes nas páginas 25, 26, and 33.

4 CHEONG, S.-W.; MOSTOVOY, M. Multiferroics: a magnetic twist for ferroelectricity. *Nature Materiaols*, v. 6, p. 13, 2007. Citado 2 vezes nas páginas 25 and 32.

5 PYATAKOV, A. P.; ZVEZDIN, A. K. Magnetoelectric and multiferroic media. *Physics - Uspekhi*, v. 55, n. 6, p. 557–581, 2012. Citado 2 vezes nas páginas 25 and 26.

6 CHUN, S. H. et al. Electric field control of nonvolatile four-state magnetization at room temperature. *Physical Review Letters*, v. 108, p. 177201, 2012. Citado 2 vezes nas páginas 25 and 26.

7 KIM, Y.; PHAM, C.; CHANG, J. P. Potentials and challenges of integration for complex metal oxides in cmos devices and beyond. *Journal of Physics D: Applied Physics*, v. 48, p. 063001, 2015. Citado na página 25.

8 WANG, K.; LIU, J.-M.; REN, Z. Multiferroicity: the coupling between magnetic and polarization orders. *Advances in Physics*, v. 58, n. 4, p. 321, 2009. Citado na página 25.

9 BINEK, C.; DOUDIN, B. Magnetoelectronics with magnetoelectrics. *Journal of Physics: Condensed Matter*, v. 17, p. L39, 2005. Citado na página 25.

10 ASTROV, D. N. et al. Spontaneous magnetoelectric effect. *Soviet Physics Journal of Experimental and Theoretical Physics*, v. 28, n. 6, p. 1123, 1969. Citado na página 26.

11 FOLEN, V. J.; RADO, G. T.; STALDER, E. W. Anisotropy of the magnetoelectric effect in Cr_2O_3. *Physical Review Letters*, v. 6, p. 607, 1961. Citado na página 26.

12 NAN, C.-W. et al. Multiferroic magnetoelectric composites: Historical perspective, status, and future directions. *Journal of Applied Physics*, v. 103, p. 031101, 2008. Citado na página 26.

13 MA, J. et al. Recent progress in multiferroic magnetoelectric composites: from bulk to thin films. *Advances Materials*, v. 23, p. 1062, 2011. Citado na página 26.

14 ZABOTTO, F. L. et al. Angular dependence of the magnetoelectric effect on PMN-PT/CFO particulate composites. *Integrated Ferroelectrics*, v. 131, n. 1, p. 127, 2011. Citado na página 26.

15 ZABOTTO, F. L. et al. Effect of ferrite concentration on dielectric and magnetoelectric properties in $(1-x)Pb(Mg_{1/3}Nb_{2/3})_{0.68}Ti_{0.32}O_3 + (x)CoFe_2O_4$ particulate composites. *Ferroelectrics*, v. 428, n. 1, p. 122, 2012. Citado na página 26.

16 GUALDI, A. J. et al. Stress magnetization model for magnetostriction in multiferroic composite. *Journal of Applied Physics*, v. 114, p. 053913, 2013. Citado na página 26.

17 VIANA, D. S. F. et al. Ferroic properties of $(0.675Pb(Mg_{1/3}Nb_{2/3})_{0.68}Ti_{0.32}O_3 - 0.325CoFe_2O_4$ prepared by spark plasma sintering. *Integrated Ferroelectrics*, v. 174, n. 1, p. 138, 2016. Citado na página 26.

18 GUALDI, A. J. et al. Understanding the dynamic magnetization process for the magnetoelectric effect in multiferroic composites. *Journal of Applied Physics*, v. 119, p. 124110, 2016. Citado na página 26.

19 ZABOTTO, F. L. et al. Grain coarsening and its effects on the properties of magnetoelectric $(0.675Pb(Mg_{1/3}Nb_{2/3})_{0.68}Ti_{0.32}O_3 - 0.325CoFe_2O_4$ particulate composites. *Journal of Alloys and Compounds*, v. 676, p. 80, 2016. Citado na página 26.

20 ZABOTTO, F. L. et al. Effect of different ferroelectric phases on magnetoelectric properties of co-ferrite particulate composites. *Ferroelectrics*, v. 497, n. 1, p. 92, 2016. Citado na página 26.

21 GUALDI, A. J. et al. Dynamic magnetization on the low temperature magnetoelectric effect in multiferroic composites. *Journal of Physics: Condensed Matter*, v. 30, p. 325803, 2018. Citado na página 26.

22 SILVA, J. et al. $BiFeO_3$: A review on synthesis, doping and crystal structure. *Integrated Ferroelectrics*, v. 126, p. 47, 2011. Citado 2 vezes nas páginas 26 and 32.

23 TOKURA, Y.; SEKI, S.; NAGAOSA, N. Multiferroics of spin origin. *Reports on Progress in Physics*, v. 77, p. 076501, 2014. Citado 7 vezes nas páginas 14, 15, 26, 35, 36, 37, and 38.

24 NAGANO, A.; ISHIHARA, S. Spin–charge–orbital structures and frustration in multiferroic RFe_2O_4. *Journal of Physics: Condensed Matter*, v. 19, p. 145263, 2007. Citado na página 26.

25 CAIGNAERT, V. et al. Gigantic magnetic-field-induced polarization and magnetoelectric coupling in a ferrimagnetic oxide $CaBaCo_4o_7$. *Physical Review B*, v. 88, p. 174403, 2013. Citado na página 26.

26 TOKURA, Y. *Colossal magnetoresistive oxides*. New York: Gordon and Breach Science Publishers, 2000. Citado na página 26.

27 WALKER, H. C. et al. Femtoscale magnetically induced lattice distortions in multiferroic $TbMnO_3$. *Science*, v. 333, n. 6047, p. 1273, 2011. Citado 2 vezes nas páginas 26 and 94.

28 SERGIENKO, I. A.; ŞEN, C.; DAGOTTO, E. Ferroelectricity in the magnetic E -phase of orthorhombic perovskites. *Physical Review Letters*, v. 97, p. 227204, 2006. Citado 3 vezes nas páginas 26, 92, and 97.

29 LEE, N. et al. Mechanism of exchange striction of ferroelectricity in multiferroic orthorhombic $HoMnO_3$ single crystals. *Physical Review B*, v. 84, p. 020101(R), 2011. Citado 2 vezes nas páginas 26 and 36.

30 MOCHIZUKI, M.; FURUKAWA, N.; NAGAOSA, N. Theory of spin-phonon coupling in multiferroic manganese perovskites $RMnO_3$. *Physical Review B*, v. 84, p. 144409, 2011. Citado na página 26.

31 MAREZIO, M. et al. High pressure synthesis and crystal structure of a new series of perovskite-like compounds CMn_7O_{12} (C =Na, Ca, Cd, Sr, La, Nd). *Journal of Solid State Chemistry*, v. 11, p. 88–93, 1973. Citado 3 vezes nas páginas 26, 27, and 42.

32 GILIOLI, E. et al. P–T phase diagram and single crystal structural refinement of $NaMn_7O_{12}$. *Solid State Sciences*, v. 7, p. 746–752, 2005. Citado 3 vezes nas páginas 26, 27, and 39.

33 GILIOLI, E. et al. High-pressure growth of $NaMn_7O_{12}$ crystals. *Journal of Solid State Chemistry*, v. 179, p. 3839–3848, 2006. Citado 5 vezes nas páginas 15, 26, 39, 41, and 42.

34 JOHNSON, R. D. et al. Giant improper ferroelectricity in the ferroaxial magnet $CaMn_7O_{12}$. *Physical Review Letters*, v. 108, p. 067201, 2012. Citado 8 vezes nas páginas 26, 27, 34, 36, 63, 92, 94, and 97.

35 ZHANG, G. et al. Multiferroic properties of $CaMn_7O_{12}$. *Physical Review B*, v. 84, p. 174413, 2011. Citado 8 vezes nas páginas 26, 27, 34, 36, 63, 92, 94, and 97.

36 DOLGOS, M. et al. Chemical control of octahedral tilting and off-axis a cation displacement allows ferroelectric switching in a bismuth-based perovskite. *Chemical Science*, n. 3, p. 1426, 2012. Citado na página 27.

37 PROSANDEEV, S. et al. Novel nanoscale twinned phases in perovskite oxides. *Advanced Functional Materials*, n. 23, p. 234, 2013. Citado na página 27.

38 HOWARD, C. J.; STOKES, H. T. Structures and phase transitions in perovskites – a group-theoretical approach. *Acta Crystallographica Section A Foundations of Crystallography*, n. 61, p. 93, 2005. Citado na página 27.

39 GAUZZI, A. et al. Magnetoelectric coupling driven by inverse magnetostriction in multiferroic $BiMn_3Mn_4O_{12}$. *Journal of Applied Physics*, v. 113, p. 043920, 2013. Citado na página 27.

40 SOULIOU, S. M. et al. Soft-phonon-driven orbital order in $CaMn_7O_{12}$. *Physical Review B*, v. 94, p. 184309, 2016. Citado 7 vezes nas páginas 27, 54, 67, 68, 70, 89, and 90.

41 GASTALDO, V. P. et al. Evidence of jahn-teller-driven wigner crystal. *unpublished*, v. 00, p. 000, 2019. Citado 3 vezes nas páginas 28, 73, and 75.

42 GAUZZI, A. et al. Ferroelectricity in the 1 $\mu c/cm^{-2}$ range induced by canted antiferromagnetism in $(LaMn_3)Mn_4O_{12}$. *arXiv:1811.07182*, v. 00, n. 00, p. 00, 2019. Citado 3 vezes nas páginas 20, 28, and 92.

43 COEY, J. M. D. *Magnetism and Magnetic Materials*. 1^{st} edition. Cambridge, United Kingdom: Cambridge University Press, 2010. Citado 3 vezes nas páginas 14, 29, and 31.

44 SKOMSKI, R. *Simple Models of Magnetism*. 1^{st} edition. New York, NY, USA: Oxford University Press, 2008. Citado 2 vezes nas páginas 14 and 30.

45 GOODENOUGH, J. B. *Magnetism and the Chemical Bond*. 1^{st} edition. New York, NY, USA: John Wiley & Sons, Inc, 1963. Citado na página 30.

46 GOODENOUGH, J. B. Theory of the role of covalence in the perovskite-type manganites $[La, M(II)]MnO_3$. *Physical Review*, v. 100, n. 2, p. 564, 1955. Citado na página 30.

47 JAHN, H. A.; TELLER, E. Stability of polyatomic molecules in degenerate electron states. i - orbital degenercy. *Proceedings of the Royal Society of London. Series A, Mathematical and Physical Sciences*, v. 161, n. 905, p. 220, 1937. Citado na página 30.

48 LEVANYUK, A. P.; SANNIKOV, D. G. Improper ferroelectrics. *Uspekhi Fizicheskikh Nauk*, v. 112, p. 561, 1974. Citado na página 32.

49 VERWEY, E. J. Electronic conduction of magnetite (Fe_3O_4) and its transition point at low temperatures. *Nature*, v. 144, p. 327–328, 1939. Citado 2 vezes nas páginas 32 and 66.

50 JIA, C. et al. Microscopic theory of spin-polarization coupling in multiferroic transition metal oxides. *Physical Review B*, v. 76, p. 144424, 2007. Citado na página 34.

51 SERGIENKO, I. A.; DAGOTTO, E. Role of the dzyaloshinskii-moriya interaction in multiferroic perovskites. *Physical Review B*, v. 73, p. 094434, 2006. Citado na página 34.

52 MOCHIZUKI, M.; FURUKAWA, N.; NAGAOSA, N. Spin model of magnetostrictions in multiferroic mn perovskites. *Physical Review Letters*, v. 105, p. 037205, 2010. Citado na página 34.

53 NAGAOSA, N. Theory of multiferroic behavior in cycloidal helimagnets. *Journal of Physics: Condensed Matter*, v. 20, p. 434207, 2008. Citado na página 34.

54 KATSURA, H.; NAGAOSA, N.; BALATSKY, A. V. Spin current and magnetoelectric effect in noncollinear magnets. *Physical Review Letters*, v. 95, p. 057205, 2005. Citado na página 34.

55 MOSTOVOY, M. Ferroelectricity in spiral magnets. *Physical Review Letters*, v. 96, p. 067601, 2006. Citado na página 34.

56 JIA, C. et al. Bond electronic polarization induced by spin. *Physical Review B*, v. 74, p. 224444, 2006. Citado na página 37.

57 JIA, C. et al. Microscopic theory of spin-polarization coupling in multiferroic transition metal oxides. *Physical Review B*, v. 76, p. 144424, 2007. Citado na página 37.

58 BELASHCHENKO, K. D. Equilibrium magnetization at the boundary of a magnetoelectric antiferromagnet. *Physical Review Letters*, v. 105, p. 147204, 2010. Citado 4 vezes nas páginas 15, 37, 38, and 91.

59 PRODI, A. et al. Magnetic structure of the high-density single-valent eg Jahn-Teller system $LaMn_7O_{12}$. *Physical Review B*, v. 79, p. 085105, 2009. Citado 6 vezes nas páginas 16, 39, 42, 55, 56, and 57.

60 WALKER, D.; CARPENTER, M. A.; HITCH, C. M. Some simplifications to multianvil devices for high pressure experiments. *American Mineralogist*, v. 75, p. 1020–1028, 1990. Citado 3 vezes nas páginas 15, 39, and 40.

61 QUANTUM DESIGN INC. *Magnetic Property Measurement System SQUID VSM User's Manual*. 6325 Lusk Boulevard, San Diego, CA 92121, USA, 2010. Citado 2 vezes nas páginas 15 and 43.

62 DUONG, G. V. et al. The lock-in technique for studying magnetoelectric effect. *Journal of Magnetism and Magnetic Materials*, v. 316, n. 2 SPEC. ISS., p. 390–393, 2007. Citado 2 vezes nas páginas 44 and 46.

63 JIMENEZ, K. R. C. P. *Efeitos da polarização elétrica sobre as propriedades magnéticas, térmicas e magnetoelétricas em compósitos multiferróicos de* $(0.675Pb(Mg_{1/3}Nb_{2/3})_{0.68}Ti_{0.32}O_3 - 0.325CoFe_2O_4$. Thesis (PhD) — Universidade Federal de São Carlos, Rodovia Washington Luis Km 235, São Carlos, SP, Brazil, december 2018. Citado 2 vezes nas páginas 15 and 45.

64 JACKSON, J. D. *Classical Electrodynamics*. 3^{rd} edition. Hoboken, NJ, USA: John WIley & Sons, Inc., 1999. Citado na página 46.

65 QUANTUM DESIGN INC. *Physical Property Measurement System Heat Capacity Option User's Manual*. 11578 Sorrento Valley Rd. San Diego, CA 92121-1311 USA, 2004. Citado 3 vezes nas páginas 15, 47, and 48.

66 VANDENABEELE, P. *Practical Raman Spectroscopy - An introduction*. 1^{st} edition. West Sussex, United Kingdom: John Wiley & Sons, Ltd, 2013. Citado 3 vezes nas páginas 15, 48, and 50.

67 SCHULKE, W. *Electron Dynamics by Inelastic X-ray Scattering*. 1^{st} edition. Oxford, United Kingdom: Oxford University Press, 2007. Citado 5 vezes nas páginas 15, 50, 51, 52, and 53.

68 MASCHEK, M. et al. Polaronic metal phases in $La_{0.7}Sr_{0.3}MnO_3$ uncovered by inelastic neutron & x-ray scattering. *Physical Review B*, v. 93, p. 045112, 2016. Citado 2 vezes nas páginas 51 and 76.

69 BARON, A. Q. R. Phonons in crystals using inelastic x-ray scattering. *Journal of The Spectroscopical Society of Japan*, v. 58, n. 5, p. 205–214, 2009. Citado na página 51.

70 KEEN, D. A.; GOODWIN, A. L. The crystallography of correlated disorder. *Nature*, v. 521, p. 303, 2015. Citado 3 vezes nas páginas 15, 53, and 54.

71 WALL, M. E.; WOLFF, A. M.; FRASER, J. S. Bringing diffuse x-ray scattering into focus. *Current Opinion in Structural Biology*, v. 50, p. 109–116, 2015. Citado na página 54.

72 BOSAK, A. et al. Short-range correlations in magnetite above the verwey temperature. *Physical Review X*, v. 4, p. 011040, 2014. Citado na página 54.

73 BROENNIMANN, C. et al. The PILATUS 1M detector. *Journal of Synchrotron Radiation*, v. 13, p. 120, 2006. Citado 2 vezes nas páginas 54 and 68.

74 OKAMOTO, H. et al. High-temperature synchrotron x-ray diffraction study of $LaMn_7O_{12}$. *Solid State Sciences*, v. 11, n. 7, p. 1211, 2009. Citado na página 56.

75 TERADA, N.; GLAZKOVA, Y. S.; BELIK, A. A. Differentiation between ferroelectricity and thermally stimulated current in pyrocurrent measurements of multiferroic MMn_7O_{12} ($M = Ca, Sr, Cd, Pb$). *Physical Review B*, v. 93, p. 155127, 2016. Citado 2 vezes nas páginas 62 and 87.

76 KIMA, J. W. et al. Observation of a multiferroic critical end point. *Proceedings of the National Academy of Sciences of the United States of America*, v. 106, n. 37, p. 15573–15576, 2009. Citado 3 vezes nas páginas 64, 86, and 92.

77 PRODI, A. et al. Charge, orbital and spin ordering phenomena in the mixed valence manganite $\left(NaMn_3^{3+}\right)\left(Mn_2^{3+}Mn_2^{4+}\right)O_{12}$. *Nature Materials*, v. 3, p. 48–52, 2004. Citado 6 vezes nas páginas 17, 65, 66, 67, 79, and 91.

78 PRODI, A. et al. Commensurate structural modulation in the charge- and orbitally ordered phase of the quadruple perovskite $(NaMn_3)\,Mn_4O_{12}$. *Physical Review B*, v. 90, p. 180101(R), 2014. Citado 8 vezes nas páginas 17, 21, 65, 66, 68, 71, 76, and 96.

79 SENN, M. S.; WRIGHT, J. P.; ATTFIELD, J. P. Charge order and three-site distortions in the verwey structure of magnetite. *Nature*, v. 481, p. 173–176, 2012. Citado na página 66.

80 SALJE, E. K. H. et al. Order-parameter coupling in the improper ferroelectric lawsonite. *Journal of Physics: Condensed Matter*, v. 24, p. 255901, 2012. Citado 2 vezes nas páginas 82 and 91.

81 BOLZONI, F. et al. Magnetic response of the CE structure in the doping-free system $NaMn_7O_{12}$. *Physical Review B*, v. 71, p. 052404, 2005. Citado 3 vezes nas páginas 83, 84, and 91.

82 VERSEILS, M. *Interplay between magnetic ordering and ferroelectricity in multiferroics with quadruple perovskite structure.* Thesis (PhD) — Université Pierre et Marie Curie - Paris VI, 4 place Jussieu, 75252, Paris cedex 05, France, may 2017. Citado 2 vezes nas páginas 20 and 94.